

Micromagnetic Simulations of Maghemite Nanospheres in FCC Arrays

by

© *BASSEL ALKADOUR*

A thesis submitted to the
School of Graduate Studies
in partial fulfilment of the
requirements for the degree of
Master of *Computational Science*

Department of *Computational Science*
Memorial University of Newfoundland

May 2015

St. John's

Newfoundland

Abstract

Encouraged by recent developments in synthesizing magnetic nanospheres and nanosphere super-lattices, we study maghemite nanospheres using stochastic LLG implemented by Maglua programming environment. We consider core-shell model where the core has bulk like exchange and the surface has weak exchange and radial anisotropy. First, we study noninteracting nanospheres with diameters ranging from 5 nm to 7.5 nm. For comparison, we vary the surface anisotropy and the surface thickness. We observe ferrimagnetic order where the core has a bulk-like spin texture and ordering temperature whereas the surface spins show a hedgehog-like texture with a domain wall at the magnetic equator. The nanospheres prefer the magnetic moment to be in the direction that maximizes the surface vacancies at the equator, which results in a magnetic torque. Also, results of multi-scale simulations of 7.5 nm maghemite nanosphere FCC arrays with different surface thicknesses are presented. Comparing these arrays with the corresponding dipole arrays (with no anisotropy) reveals an orientational disorder below $T = 20$ K due to magnetic torque generated by the surface vacancies.

Acknowledgements

First and foremost I would like to express my sincerest gratitude to my supervisor, Prof. John P. Whitehead, for his guidance, support, insightful comments, hard questions, and encouragement.

I place on record, my sincere gratitude to Jason I. Mercer for his significant contribution in developing the codes that have been used in this work.

I am also grateful to Prof. Byron W. Southern and thank Prof. Johan V. Lierop for all the fruitful discussions and valuable inputs.

I also would like to thank Prof. Martin L. Plumer and Dr. Ahmad M. Almudallal for their critical reading.

I take this opportunity to express my gratitude to my parents, Ahmad Rafea Alkadour and Faten Alkadour, and my siblings for supporting me throughout all my studies.

Also, I wish to thank my friends Rabea Almatarneh, Eyad Sakkar, Justin Royce, Asfand Tareen, Purna Roy, and Vahid Hemmati for their support.

Thanks also to the Department of Physics and Physical Oceanography and Memorial University of Newfoundland for giving me all the chances and experiences that I need to establish my future.

Contents

Acknowledgements	iii
List of Tables	vii
List of Figures	viii
1 Introduction	1
1.1 Nanospheres	1
1.2 Synthesizing and coating nanospheres	2
1.3 Assemblies of MNPs	3
1.4 Properties and structure of maghemite	4
1.5 Magnetic properties of maghemite nanospheres	6
1.6 Previous models and simulation results for maghemite nanospheres	11
1.6.1 Results from previous simulations	11
1.7 Other models	19
1.8 Outline of the thesis	19
2 Noninteracting Maghemite Nanospheres	21
2.1 Simulation using the stochastic Landau-Lifshitz-Gilbert equation	21

2.1.1	Results from simulations	23
2.2	Blocking temperature	31
2.3	The microscopic spin ordering	35
2.4	The effect of the surface vacancies	44
2.5	The effect of the surface thickness	50
2.6	Summary	58
3	Nanoparticles Superstructures and Inter-Nanoparticle Interactions	60
3.1	The ground state of dipolar lattices in two and three dimensions	61
3.2	Magnetic dipole interactions in FCC arrays	63
3.3	Summary	68
4	Nanosphere FCC Array	71
4.1	Model and parameters of the nanosphere FCC lattices	72
4.2	The equivalent dipole lattice	75
4.3	Results and Analysis	78
4.4	Summary	86
5	Conclusion	93
5.1	Maghemite noninteracting nanospheres	93
5.2	FCC dipole lattice	94
5.3	Maghemite nanospheres on FCC lattice with dipole interactions	95
5.4	Future work	97
	Bibliography	99

A Comparing Stochastic LLG with Monte Carlo	108
B Comparing noninteracting maghemite nanosphere simulation with experimental results	111
C Euler integration error in nanospheres lattice	113

List of Tables

1.1	Sublattices displacements used for heat bath MC simulations of maghemite nanospheres.	13
1.2	L (the number of unit cells) and the corresponding diameter in nm units that were used in MC simulations from Ref [37].	13
1.3	Maghemite nanospheres exchange parameters used for MC simulation.	14
2.1	The maghemite nanospheres parameters used in LLG simulations. . .	24
2.2	Characteristic parameters of the ensembles K5, K10, Dc63, and Dc675.	25
4.1	Characteristic parameters of FDc63, FDc675 and the corresponding dipole lattices, d63 and d675.	75

List of Figures

1.1	Ferritin's structure.	3
1.2	Spinel superstructure.	4
1.3	Saturation magnetization as a function of temperature of 7 nm diameter dispersed maghemite nanospheres (the data are adapted from experimental results in Ref. [1]).	7
1.4	The magnetization of a dilute dispersion of maghemite nanospheres as a function of temperature. The sample was cooled in no field then heated and cooled in a finite field [20].	10
1.5	The total magnetization of maghemite single nanospheres of different sizes as a function of temperature. The results are obtained using MC simulation from Ref. [37] where the units of temperature, field, and anisotropy are (12.5 K) and the magnetization unit is $5 \mu_B/\text{ion}$. The unit scaling is explained in Appendix. A.	16

1.6	The core magnetization of maghemite single nanospheres of different sizes as a function of temperature. The results are obtained using MC simulation from Ref. [37] where the units of temperature, field, and anisotropy are (12.5 K) and the magnetization unit is $5 \mu_B/\text{ion}$. The unit scaling is explained in Appendix. A.	17
1.7	The surface magnetization of maghemite single nanospheres of different sizes as a function of temperature. The results are obtained using MC simulation from Ref. [37] where the units of temperature, field, and anisotropy are (12.5 K) and the magnetization unit is $5 \mu_B/\text{ion}$. The unit scaling is explained in Appendix. A.	18
2.1	The average magnitude of the core magnetization (M_c), magnitude of the surface magnetization (M_{srf}) and the magnitude of the magnetization of the nanosphere (M_n) as functions of temperature. The data represents the K10 ensemble cooled in $H_z = 5 \text{ K}$ (1.49 T). K10 consists of 1000 maghemite nanospheres of $D = 5 \text{ nm}$, diameter, $D_c = 3.67 \text{ nm}$ core diameter and $K_s = 10 \text{ K}$ ($2.58 \times 10^{-23} \text{ J}$).	27
2.2	The average magnitude of the core magnetization (M_c), magnitude of the surface magnetization (M_{srf}) and the magnitude of the magnetization of the nanosphere (M_n) as functions of temperature. The data represents the K10 ensemble cooled in $H_z = 5 \text{ K}$ (1.49 T). K5 consists of 1000 maghemite nanospheres of $D = 5 \text{ nm}$ diameter, $D_c = 3.67 \text{ nm}$ core diameter and $K_s = 5 \text{ K}$ ($1.29 \times 10^{-23} \text{ J}$).	28

2.3	M_{srf} for different anisotropies as a function of temperature. The results from cooling the K5 and K10 ensembles, with $H = 5$ K.	29
2.4	M_z and M_n as a function of temperature for cooling the ensemble K10 under a magnetic field $H_z = 5$ K.	30
2.5	Data showing the magnetization of the zero field cooled ensemble K10 (Table 2.2) during the heating and then the cooling processes under an applied field of $H_z = 0.4$ K (0.12 T) where the heating and cooling rate is $0.1\text{K}/t_u$ (1.76×10^{11} K/sec).	32
2.6	The magnetization of the zero field cooled ensemble K5 (Table 2.2) during the heating and then the cooling processes under an applied field of $H_z = 0.4$ K (0.12 T) where the heating and cooling rate is $0.1\text{K}/t_u$ (1.76×10^{11} K/sec).	33
2.7	The magnetization of the zero field cooled ensemble K10 (Table 2.2) during the heating and then the cooling processes under an applied field of $H_z = 0.4$ K (0.12 T). The data compares a heating and cooling rate of $0.1\text{K}/t_u$ (1.76×10^{11} K/sec) with a rate of $0.05\text{K}/t_u$	34
2.8	Spin configuration of a single nanosphere at $T = 0$ K, $K_s = 5$ K, and $H_z = 5$ K.	36
2.9	Simplified spin configuration of a single nanosphere at $T = 0$ K.	37
2.10	The radial component of each spin of a single nanosphere with 5 K at $T=0$ K.	39
2.11	The radial component of each spin in a single nanosphere at different temperatures. The nanosphere has $D = 5$ nm, $D_c = 3.67$ nm and $K_s = 5$ K cooled in zero external field.	40

2.12	The radial component of each spin in a single nanosphere at different temperatures. The nanosphere has $D = 5$ nm, $D_c = 3.67$ nm and $K_s = 10$ K cooled in zero external field.	42
2.13	The polar distribution of the reversed spins as a function of $\cos(\varphi)$ at different temperatures. The results are from the K5 and the K10 ensembles cooled in zero field.	43
2.14	The polar distribution of surface vacancies of the ensemble K5 as a function of $\cos(\varphi)$ at different temperatures. The ensemble has been cooled with rate of 0.1 K/ t_u under zero external field.	45
2.15	The polar distribution of surface vacancies of the ensemble K10 as a function of $\cos(\varphi)$ at different temperatures. The ensemble has been cooled with rate of 0.1 K/ t_u under zero external field.	46
2.16	The polar distribution of surface vacancies for the ensembles K10 and K5 as a function of $\cos(\varphi)$ at different temperatures. The ensembles have been cooled with rate of 0.1 K/ t_u under zero external field.	49
2.17	The cumulative density of surface vacancies (CDV) of the ensembles K5 as a function of P_s (the percentage of the surface spins allocated around the magnetic equator) at different temperatures.	51
2.18	The cumulative density of surface vacancies (CDV) of the ensembles K10 as a function of P_s (the percentage of the surface spins allocated around the magnetic equator) at different temperatures.	52
2.19	The polar distribution of surface vacancies for the ensemble Dc63 as a function of $\cos(\varphi)$ at different temperatures. The ensemble has been cooled with rate of 1 K/ t_u under zero external field.	54

2.20	The polar distribution of surface vacancies for the ensemble Dc675 as a function of $\cos(\varphi)$ at different temperatures. The ensemble has been cooled with rate of 1 K/t_u under zero external field.	55
2.21	The cumulative density of surface vacancies (CDV) of the ensembles Dc63 as a function of P_s (the percentage of the surface spins allocated around the magnetic equator) at different temperatures.	56
2.22	The cumulative density of surface vacancies (CDV) of the ensembles Dc675 as a function of P_s (the percentage of the surface spins allocated around the magnetic equator) at different temperatures.	57
3.1	The magnetization of different sizes of the FCC lattice of magnetic dipoles as a function of temperature.	64
3.2	The susceptibility of different sizes of the FCC lattice of magnetic dipoles as a function of temperature (the susceptibility is divided by the number shown in the legend and the solid lines are drawn for the convenience of the eye).	65
3.3	The heat capacity of different sizes of the FCC lattice of magnetic dipoles as a function of temperature.	66
3.4	The dipole energy of different sizes of the FCC lattice of magnetic dipoles as a function of temperature.	67
3.5	Binder cumulant for different sizes of the FCC lattice of magnetic dipoles as a function of temperature (lines are just for guidance).	69

4.1	The relation between the reduced temperature and the temperature of two FCC dipole lattices d63 and d675 which correspond to the nanospheres with core diameter $D_c = 6.3$ nm and 6.75 nm, respectively (Table 4.1).	77
4.2	M_{nl} of an $8 \times 8 \times 8$ FCC nanosphere array as a function of temperature, where the nanospheres have a 7.5 nm diameter, 6.75 nm core diameter, 7.5 nm center to center spacing and $K_s = 10$ K (FDc675 Table 4.1). . .	79
4.3	M_{nl} of an $8 \times 8 \times 8$ FCC nanosphere array as a function of temperature, where the nanospheres have a 7.5 nm diameter, 6.3 nm core diameter, 7.5 nm center to center spacing and $K_s = 10$ K (FDc63 Table 4.1). . .	80
4.4	The lattice magnetization, M_{nl} , and the magnitude of the nanosphere magnetic moment, M_n , as a function of temperature. M_{nl} and M_n belong to the array FDc675 (Table 4.1). The array is an $8 \times 8 \times 8$ FCC lattice with 7.5 nm diameter nanospheres, 6.75 nm core diameter, $K_s = 10$ K and 7.5 nm center to center distance between the nearest neighbors. Also, M_{dl} , the magnetization of the corresponding dipole lattice (d675 Table 4.1) is presented as a function of temperature. . .	82
4.5	As in Fig. 4.4 for the FDc63 lattice.	83
4.6	The density of the vacancies of the lattice, FDc675, and the corresponding ensemble of non-interacting nanospheres, Dc675, as a function of $\cos(\varphi)$ at different temperatures.	85
4.7	O_{nl} and O_{dl} of an $8 \times 8 \times 8$ FCC array as a function of temperature, where the nanospheres have a 7.5 nm diameter, 6.75 nm core diameter and $K_s = 10$ K.	87

4.8	O_{nl} and O_{dl} of an $8 \times 8 \times 8$ FCC array as a function of temperature, where the nanospheres have a 7.5 nm diameter and 6.3 nm core diameter.	88
4.9	O_{nl} of $8 \times 8 \times 8$ FCC arrays as a function of temperature, where the nanospheres have a 7.5 nm diameter with $K_s = 10$ K in both cases. One of the lattices has nanospheres of core diameter 6.3 nm, while the other has nanospheres of core diameter 6.75 nm.	89
4.10	The density of the vacancies of the lattice, FDc63, and the corresponding ensemble of non-interacting nanospheres, Dc63, as a function of $\cos(\varphi)$ at different temperatures.	90
A.1	The total magnetization of maghemite single nanosphere with 5 nm diameter as a function of temperature. The data compares MC simulations from Ref. [37] with stochastic LLG simulation results. The units of temperature, field, and anisotropy are (12.5 K) and the magnetization unit is $5 \mu_B/\text{ion}$.	110
B.1	The saturation magnetization of 7 nm diameter dispersed maghemite nanospheres as a function of temperature. The data represents the experimental results in Ref. [1] (red) and the stochastic LLG simulations with $K_s = 20$ K and 0.735 nm surface thickness.	112
C.1	The magnetization of the FDc675 FCC nanosphere lattice and the corresponding dipole lattice. The data represents results using Euler and RK4 integration of the LLG equation with time step $2 \times 10^{-4} t_u$.	114

Chapter 1

Introduction

1.1 Nanospheres.

Magnetic nanospheres are spherical particles with diameters in the range between 1 nm and 100 nm. They are usually ferromagnetic or ferrimagnetic chemical compounds of the iron triad (Fe, Ni, and Co) such as, magnetite (Fe_3O_4), maghemite ($\gamma - \text{Fe}_2\text{O}_3$) [1], NiFe_2O_4 [2], and CoFe_2O_4 [3]. They also consist of antiferromagnetic materials such as, goethite ($\alpha - \text{FeOOH}$) [2]. The symmetry of the bulk crystal breaks at the surface which result in additional anisotropy on the surface in addition to possible chemical changes [4]. Since nanospheres have big surface to volume ratio, they exhibit magnetic properties significantly different from the bulk materials. Magnetic nanoparticles can differ from bulk materials in other ways. For example, bulk materials can form multiple magnetic domains due to the exchange and dipole interactions, while nanospheres can only form a single domain when nanospheres are very small. The diameter at which nanospheres can form only one domain is known

as the critical diameter [2].

1.2 Synthesizing and coating nanospheres

Many applications require nanospheres with a narrow distribution of diameters [5]. While many methods are used to fabricate nanoparticles, only a few can produce nanospheres with a narrow size distribution. These methods include: condensation methods [2, 5], thermolysis of metal-containing compounds [2], synthesis in reverse micelles [2], and sol-gel methods [1].

In many cases, metallic nanoparticles are unstable when exposed to air and might spontaneously ignite at room temperature [2]. However, encapsulation of magnetic nanoparticles can stabilize them by preventing oxidation and aggregation. Besides that, encapsulation in organic polymers provides compatibility with organic tissues which is important for many biomedical applications [6]. Coated magnetic nanoparticles, ferritin for example, exist naturally in many biological complexes. Ferritin shown in Fig. 1.1, is a water soluble protein filled mostly by ferrihydrite ($5\text{Fe}_2\text{O}_3 \cdot 9\text{H}_2\text{O}$) [7], which can be extracted from horse's spleen on a commercial level. It consists of 24 polypeptides forming a shell of 6 nm thickness and a hollow core of 8 nm diameter [7]. The ferritin without the core of iron compounds is called apoferritin. It is possible to fill the ferritin with magnetite/maghemite nanospheres after extracting the native iron in the core forming the so-called magnetoferritin. Having the magnetic nanospheres encapsulated in this coat does not only provide a protection, but also can be used to obtain a variety of self assembled superstructures of nanospheres [8].

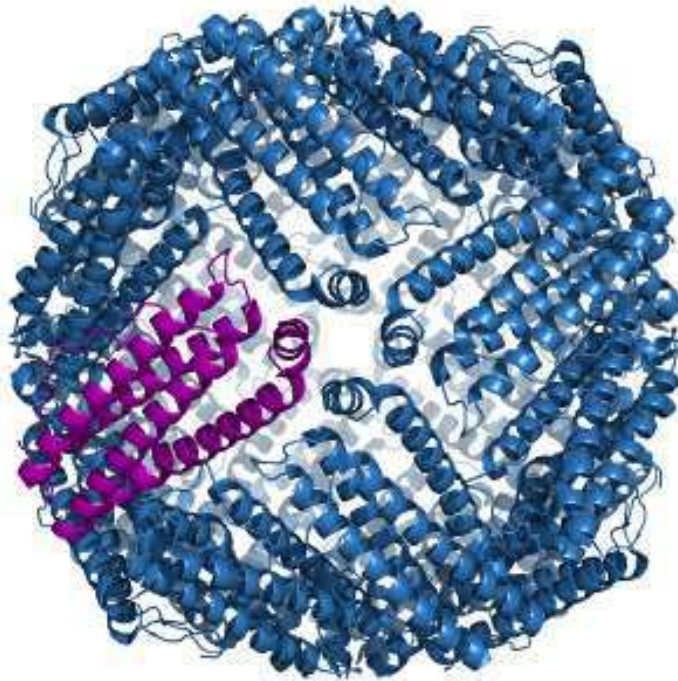


Figure 1.1: Ferritin's structure.

1.3 Assemblies of MNPs

Besides the unique properties of magnetic nanoparticles (MNPs), assemblies of MNPs show a collective behavior that opens the door to further applications, such as, high density hard disks [9], magnetic refrigeration [10], spintronics [11], medicine and biology [12, 13], and hyperthermia [14].

Many methods for synthesizing assemblies of nanoparticles have been developed such as the LangmuirBlodgett method [15] and more widely the variety of self assembly techniques, such as, self-assembly at interfaces [16], self-assembly using templating [16], assisted self assembly [16], patterned self assembly [9, 17, 18, 19] and self assembly in a solution [17, 20]. One advantage of self assembly in solution relies on the possibility of using an organic coat such as ferritin as the source of the forces

that form the assembly. In particular, apoferritin can be crystallized in FCC, cubic, tetragonal or orthorhombic structure. Consequently, corresponding lattices of magnetic nanospheres can be formed by synthesizing the nanospheres inside the ferritin cage then making the magnetoferritin complex form the desired structure [20, 8].

1.4 Properties and structure of maghemite

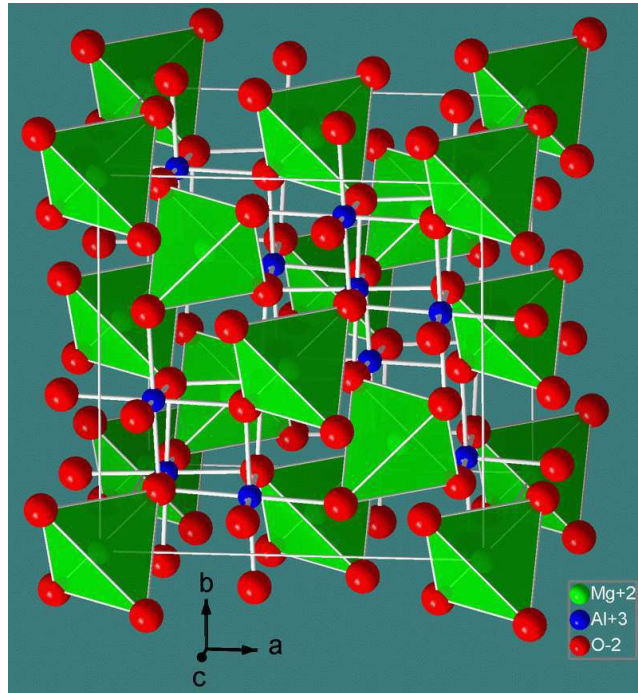


Figure 1.2: Spinel superstructure.

Most of the work described in this thesis focuses on the properties of nanospheres formed from, the spinel ferrite, maghemite. Many magnetic oxides such as ZnFe_2O_4 [21], MgAl_2O_4 [22], Fe_3O_4 [23], and MnFe_2O_4 [24] have crystalline superstructures similar to the spinel MgAl_2O_4 [25] as shown in Fig. 1.2, the compound that this

superstructure is named after. Spinels have the general formula $A^{2+}B_2^{3+}O_4^{2-}$, where A^{2+} and B^{3+} can be the same or can be two different types of minerals, whereas O^{2-} can be oxygen or any other (-2) anion. Normally the spinel unit cell has 32 oxygen anions arranged in a cubic close packed lattice which contains 64 holes in a tetrahedral lattice (TH), with 1/8 of them are occupied by A^{2+} cations, and 32 holes in an octahedral lattice (OH), with 1/2 of them are occupied by B^{3+} cations, leading to 8 ($A^{2+}B_2^{3+}O_4^{2-}$) in each unit cell [25].

Inverse spinel structures as in magnetite ($Fe^{3+}(Fe_2^{3+})(O^{2-})_4$) have a different cation distribution, where 1/2 of the B^{3+} cations occupy the TH sites, whereas all A^{2+} and the other 1/2 of B^{3+} occupy the OH sites [25]. The antiferromagnetic superexchange between OH and TH cations through the oxygen anions results in the ferrimagnetic behavior of magnetite [25]. Since the number of OH spins does not equal the number of TH spins, magnetite is considered as a ferrimagnetic material. Magnetite has curie temperature $T_c = 850$ K and saturation magnetization $M_s = 90$ Am²/Kg [26].

Maghemite ($\gamma - Fe_2O_3$) is another inverse spinel iron oxide compound which contains defects in the lattice structure. Maghemite's structure can be derived from magnetite by removing 1/6 of the iron atoms at the OH sites and distributing some of the oxygen anions over these vacancies to neutralize the charges. Removing some of the iron atoms results in making all the iron atoms in maghemite triple cations Fe^{3+} [27, 28]. Since maghemite is fully oxidized, it is more stable than magnetite. In addition to the ease of oxidizing magnetite to form maghemite, the high stability of maghemite and the low toxicity [29] encourage using maghemite nanospheres in many applications such as drug delivery and magnetic resonance imaging [30].

Bulk maghemite has an estimated saturation magnetization of $M_{s0} (bulk) = 400$ emu/cm³

[31], curie temperature of $T_c \simeq 950$ K [28], and small anisotropy of -5 kJ/m³ [32]. Similar to magnetite, maghemite is ferrimagnetic due to the superexchange between the iron spins through the oxygen atoms[25].

Many methods have been developed to produce maghemite nanospheres of narrow size distribution with diameters smaller than the critical diameter [1, 2]. Maghemite nanospheres of 7nm diameter have a special interest because many medical applications require this size due to the possibility of encapsulating these nanospheres in ferritin.

1.5 Magnetic properties of maghemite nanospheres

Neutron scattering experiment on CoFe₂O₄ nanoparticles [33] shows that the magnetization of nanoparticles comprises a core with a bulk like magnetization surrounded by a shell of disordered spins with a thickness larger than 1 nm. This is consistent with the observed dramatic increase of the saturation magnetization of maghemite nanospheres at low temperature while maintaining a bulk like magnetization curve at high temperature as shown in Fig 1.3 from Ref [1].

Based on the core-shell model and using the experimental measurements of the saturation magnetization, as in Fig 1.3, it is possible to extrapolate many of the magnetic parameters of these 7 nm diameter nanospheres. Since the core spins have magnetic properties similar to bulk material, they order at high temperature ($T_c \approx 1000$ K comparable to that of bulk maghemite). As a result, the saturation magnetization of the core is almost constant at temperatures much lower than T_c .

Fig. 1.3 shows a significant increase in the saturation magnetization below $T \approx$

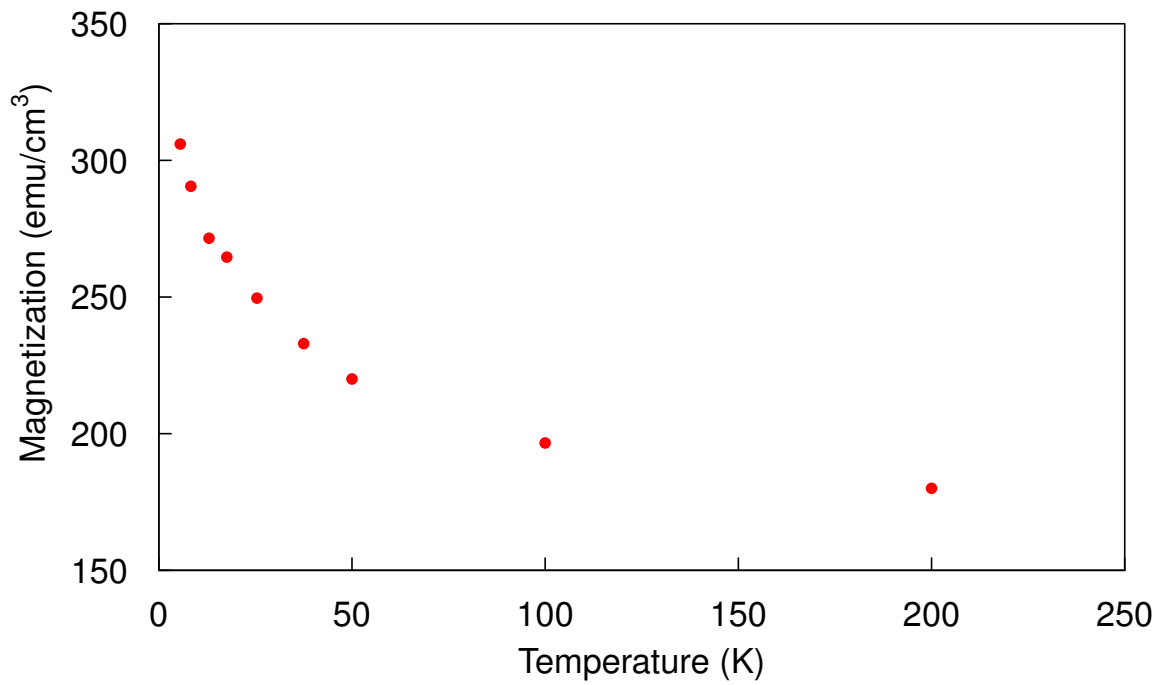


Figure 1.3: Saturation magnetization as a function of temperature of 7 nm diameter dispersed maghemite nanospheres (the data are adapted from experimental results in Ref. [1]).

35K, which indicates that the surface starts to order at $T_s \approx 35$ K. Above T_s , the saturation magnetization is almost constant which means only the bulk-like core is contributing in the saturation magnetization at temperature above T_s . Comparing the measured saturation magnetization of the nanospheres at $T > 35$ K with that of the bulk maghemite, we obtain the ratio,

$$M_{s0 \text{ (core)}}/M_{s0 \text{ (bulk)}} \approx 210/400 \approx 0.5. \quad (1.1)$$

This implies that approximately 50% of the iron atoms are located in the core and the rest are located on the surface. From this ratio, the surface thickness is expected to be (0.72 nm) as explained in the following calculations,

$$\begin{aligned} V_{\text{core}}/V_{\text{total}} &= (R_c/R_s)^3 = 0.5, \\ R_c &= R_s \times \sqrt[3]{0.5}, \\ R_c &= 3.5 \times \sqrt[3]{0.5} \approx 2.78 \text{ nm}, \\ R_s - R_c &= 3.5 - 2.78 \approx 0.72 \text{ nm}, \end{aligned} \quad (1.2)$$

where V_{core} is the core volume, V_{total} is the volume of the nanosphere, R_c is the core radius, and R_s is the nanosphere's radius.

By ignoring the effect of both the core-surface interactions and the surface anisotropy on the ordering temperature of the surface, it becomes easy to estimate the ratio of the exchange interactions between the surface spins (J_{ss}) and the corresponding exchange interactions in the core (J_{cc}),

$$J_{ss}/J_{cc} = T_s/T_c \approx 35/1000 = 0.035. \quad (1.3)$$

In Fig 1.3, it can also be observed that near $T = 0$ K the saturation magnetization of the nanospheres is nearly 280 emu/cm^3 , which is considerably less than the saturation magnetization observed in the bulk maghemite $M_{sb} \approx 400 \text{ emu/cm}^3$. This can be attributed to the large surface anisotropy which causes the disordering of the surface spins.

The surface anisotropy also plays an important role at temperatures below the blocking temperature (T_b) in term of the magnetic dynamics of the nanospheres. Below T_b , the rate at which the surface spins can flip their direction due to thermal fluctuations is constrained by the energy barrier arising from the surface anisotropy. As a consequence, the magnetic moment of the whole nanosphere can not freely change direction as it does at temperatures higher than T_b . The blocking effect is seen in Fig 1.4 in which a dilute dispersion of 7 nm diameter maghemite nanospheres is cooled in a zero field to a temperature close to 0 K. At $T = 0$ K the surface spins freeze and lock in the magnetization of each of the nanospheres in random directions. As a result, the whole system of the non-interacting nanospheres has zero net magnetization. When a weak field is applied at $T = 0$ K, the spins are blocked due to the surface anisotropy and the magnetization of the system remains effectively zero. If the temperature is increased, the effect of the blocking is reduced and the net magnetization of the zero field cooled (ZFC) nanospheres increases due to the tendency of each nanosphere's magnetic moment to align parallel to the applied field. However, at some temperature the disordering of the magnetic orientation of the nanospheres due to the thermal fluctuations begins to reduce the net magnetization of the system, resulting in a peak in the net magnetization. By cooling the sample

in the same field after that, the magnetization increases monotonically. The point where the heating and cooling curves diverge is usually taken to define the blocking temperature (~ 25 K in this case).

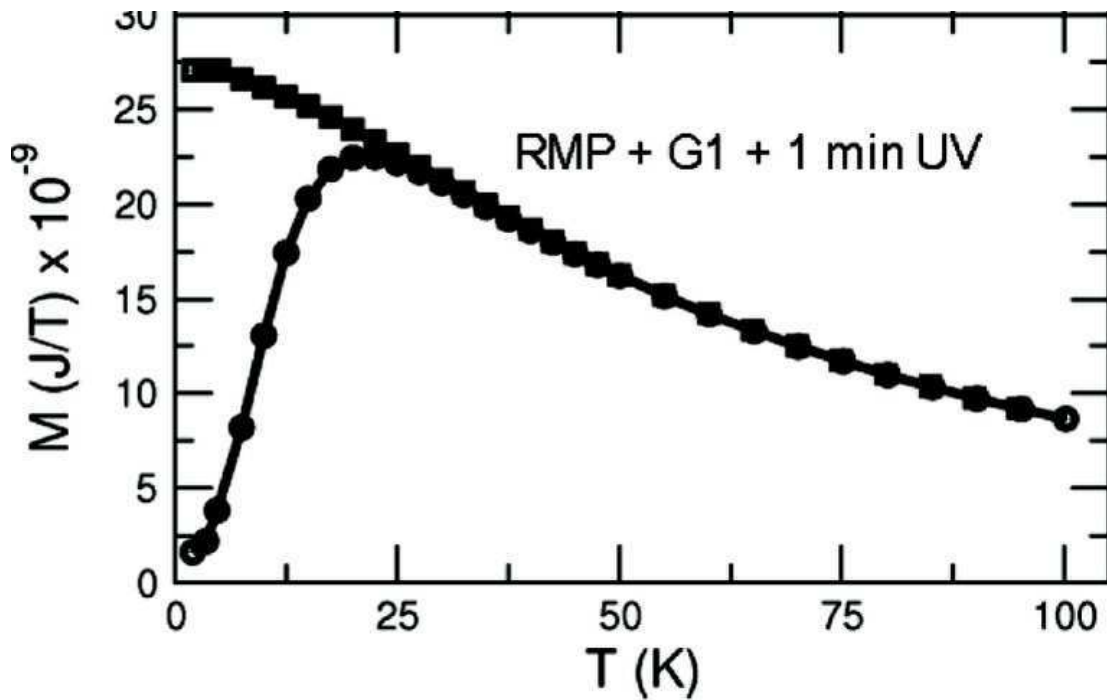


Figure 1.4: The magnetization of a dilute dispersion of maghemite nanospheres as a function of temperature. The sample was cooled in no field then heated and cooled in a finite field [20].

1.6 Previous models and simulation results for maghemite nanospheres

The first model of magnetic nanoparticles based on surface spins disorder was proposed by Kodama [34]. This model assumes a bulk-like core, broken exchange at the surface ($J=0$ for 80% of the exchange bonds), and classical spins with no anisotropy or dipole interactions. Applying the model to NiFe_2O_4 shows surface spin-canting resulting in a reduction in the magnetic moment of all nanoparticles. Additionally, multiple stable surface spins configurations appear as a result of the broken bonds. Further more, applying the same model to NiFe_2O_4 and $\gamma - \text{Fe}_2\text{O}_3$ but with bulk-like anisotropy in the core and anisotropy with radial easy axis in the surface shows irreversible transition demonstrated by open hysteresis loops [35].

1.6.1 Results from previous simulations

A previous MC study of non-interacting maghemite nanospheres [36] was done with the following energy expression,

$$E = - \sum_{\langle i,j \rangle} J_{ij} \vec{S}_i \cdot \vec{S}_j - K_s \sum_{i \in \text{surface}} (\vec{S}_i \cdot \hat{n}_i)^2 - K_V \sum_i (S_{x,i}^2 S_{y,i}^2 + S_{y,i}^2 S_{z,i}^2 + S_{z,i}^2 S_{x,i}^2). \quad (1.4)$$

The first term is due to the exchange interactions where J_{ij} is the magnetic exchange interaction between neighbors located at sites i and j . The value of J_{ij} depends on the type of atoms at sites i and j (A or B) where the exchange energies in units of k_B are: $J_{AA} = -1.3 \text{ K}$, $J_{AB} = -33.9 \text{ K}$ and $J_{BB} = 7.3 \text{ K}$. The surface anisotropy K_s was studied with different values and it is radial where \hat{n}_i is the radial unit vector at

spin i . $K_V = 8.13 \times 10^{-3}$ K is the cubic anisotropy that exists in the bulk maghemite. Each filled Fe^{+3} site was assigned $(5/2) \mu_b$, where μ_b is bohr magneton.

The study focused on 3.3 nm diameter nanospheres where the core diameter is half of the nanospheres diameter. The results show a hedgehog spin texture at the surface where two domains can be recognized when $K_s/K_V < 10^4$. This texture explains the reduction of the nanospheres magnetization compared to the bulk material. On the contrary to what is obtained experimentally [1], the nanospheres magnetization in that simulation shows no increase at low temperature. This can be attributed to the fact that the study assumed the same exchange parameters at the surface and the core, as we will see.

Of particular relevance to the present work are simulations of non-interacting maghemite nanospheres using heat bath Monte-Carlo simulations done by Adebayo *et al.* [37]. The simulations were carried out on the maghemite spinel-like structure discussed previously, where sites (A) correspond to the tetrahedral sites and sites (B) correspond to the octahedral sites. Each of the (A) and (B) sites is occupied by a spin of $1 \mu_b$ in magnitude and the vacancies are randomly distributed among (B) sites. To build the superlattice, a cube (base) of the FCC lattice is built with sites $4(i + k, i + j, j + k)$, where (i, j, k) are integers in the range $-L$ to L , where L is the nanosphere diameter measured in unit cells. Two (A) sites and four (B) sites surround each of the FCC sites with a distance corresponding to the vectors in Table 1.1.

Nanosphere diameters are arranged to be L unit cells by eliminating any spins located at distances larger than $4L$ from the center. In all cases studied by Adebayo *et al.*, the surface of each nanosphere has a thickness of two unit cells (1.66 nm). For convenience the diameter of the nanospheres presented here is expressed in terms of

Ion Type	A1	A2	B1	B2	B3	B4
Location	(0,0,0)	(2,2,2)	(1,1,-3)	(3,1,-1)	(-1,3,1)	(1,3,-1)

Table 1.1: Sublattices displacements used for heat bath MC simulations of maghemite nanospheres.

the number of unit cells (L), where each unit cell of maghemite is a cube with a side length of 0.83 nm. Table 1.2 shows the diameter of the simulated nanospheres in nm and the corresponding number of unit cells. The energy of a nanosphere, which

L (unit cells)	Diameter (nm)
4	3.3
5	4.2
6	5.0
7	5.8
8	6.6
9	7.5

Table 1.2: L (the number of unit cells) and the corresponding diameter in nm units that were used in MC simulations from Ref [37].

Adebayo *et al.* based their model on may be written as

$$E = - \sum_{i < j} J_{ij} \vec{S}_i \cdot \vec{S}_j - \sum_{i \in \text{surface}} K_s (\vec{S}_i \cdot \hat{n}_i)^2 - \sum_{i \in \text{core}} K_c S_{iz}^2 - \vec{H} \sum_i \vec{S}_i. \quad (1.5)$$

The first two terms are as in Eq. 1.4. The third term is the core anisotropy interaction

with K_c is the core anisotropy constant, where the easy axis is the Z-direction. The last term is the zeeman field term.

Table 1.3 shows the exchange values between different sites. Each of the site notations i and j is replaced by a combination of the following notations: “c” for sites in the core, “s” for sites in the surface, “a” for the (A) sites, and “b” for the (B) sites. For example, the first line in the table shows that the exchange constant between two neighboring spins located in the core with one of them on a site (A) and the other on a site (B) is $J_{ca-cb} = -56.2$ K (All energies are quoted in Kelvin). The last line shows that the exchange between two spins, both of them at the surface, is 10% of the exchange between two spins of corresponding types (A or B) at the core. As a result, the ordering temperature of the surface (T_s) is expected to be about 10% of the core ordering temperature (T_c). The core-surface $J_{s_b^a-c_b^a}$ exchange is assumed to be half of the exchange between the corresponding types at the core $J_{c_b^a-c_b^a}$.

exchange parameter	value (K)	position	interacting sites
J_{ca-cb}	-56.2	core-core	A-B
J_{ca-ca}	-42.0	core-core	A-A
J_{cb-cb}	-17.2	core-core	B-B
$J_{s_b^a-c_b^a}$	$J_{c_b^a-c_b^a} \times 0.5$	surface-core	A or B – A or B
$J_{s_b^a-s_b^a}$	$J_{c_b^a-c_b^a} \times 0.1$	surface-core	A or B – A or B

Table 1.3: Maghemite nanospheres exchange parameters used for MC simulation.

Fig. 1.5 shows the total magnetization of a single sphere as obtained by Adebayo

et al. for different sizes. The magnetic moment verses temperature curve shows qualitative agreement with the experimental results of saturation magnetization presented in Fig. 1.3 (assuming that the magnetic moment of the nanosphere is aligned along the direction of the saturation field). As explained in Appendix. A, one temperature unit is equivalent to 12.5 K while one magnetization unit is equivalent to $(5 \mu_b/\text{ion})$. The two distinct ordering temperatures are due to the two different sets of exchange parameters, the core set on one side, and the surface set on the other side. The high values of exchange at the core results in a high ordering temperature of the core ($T_c \approx 70 \times 12.5 \simeq 875 \text{ K}$) as shown in Fig 1.6. The weak exchange interactions at the surface produce the low ordering temperature ($63 \text{ K} < T_s < 125 \text{ K}$) as shown in Fig. 1.7.

The non-zero magnetization above T_c for the core and above T_s for the surface is due to the size effect. The saturation magnetization per spin is significantly less than the magnetic moment of each spin even for bulk maghemite due to the ferrimagnetic order. Assuming a perfect ferrimagnetic spins alignment, (A) spins would be anti-parallel to (B) spins. Since 1/6 of B sites are vacancies, maghemite has two spins at (A) sites for each of the four ($\times 5/6$) spins on (B) sites, the maximum net magnetization per spin is 1/4 of the magnetic moment of a spin. For nanosphere with fully parallel spins, the average magnetic moment per spin is:

$$M_{\text{tot}} = \frac{-2 + 4 \times \frac{5}{6}}{2 + 4 \times \frac{5}{6}} \times (5\mu_b) = 0.25 \times (5\mu_b). \quad (1.6)$$

Fig. 1.7 shows the surface magnetization of a single sphere at different sizes for $K_s = 5 \times (12.5 \text{ K})$. The ordering temperature of the surface is $63 \text{ K} < T_s < 125 \text{ K}$.

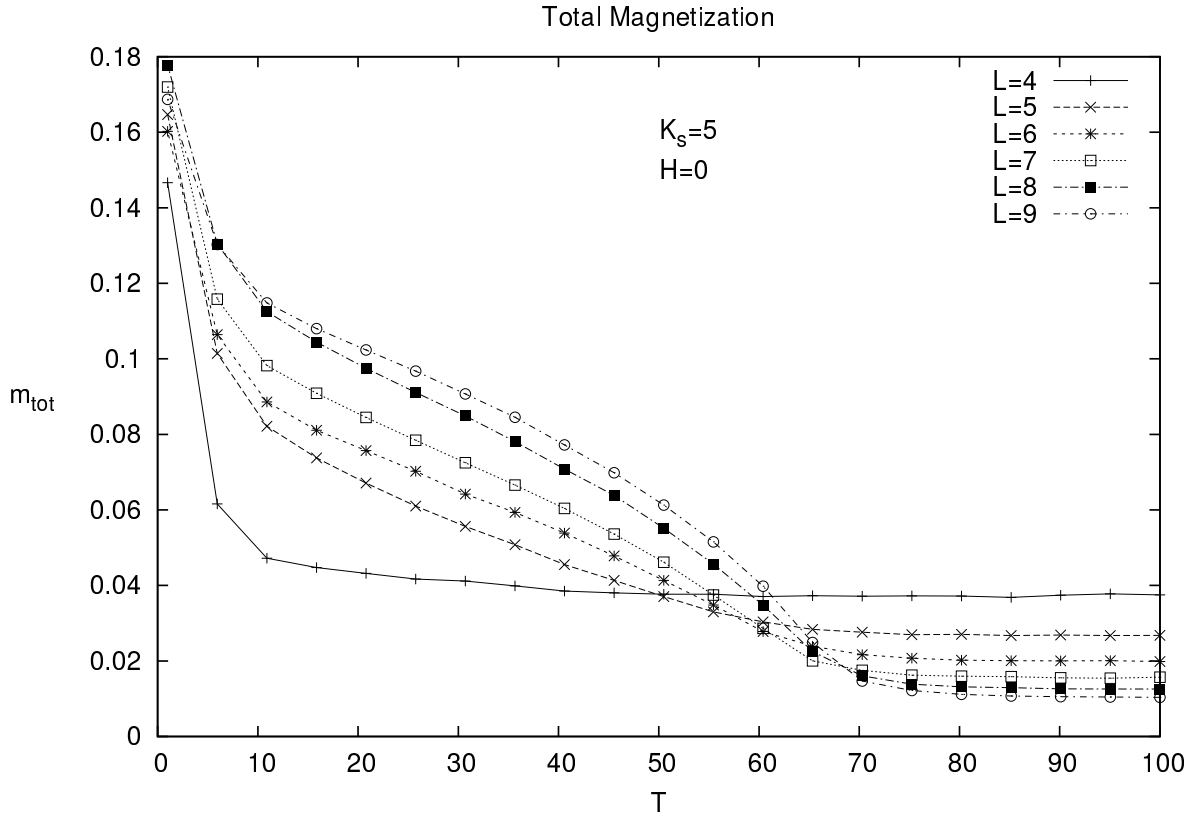


Figure 1.5: The total magnetization of maghemite single nanospheres of different sizes as a function of temperature. The results are obtained using MC simulation from Ref. [37] where the units of temperature, field, and anisotropy are (12.5 K) and the magnetization unit is $5 \mu_B/\text{ion}$. The unit scaling is explained in Appendix. A.

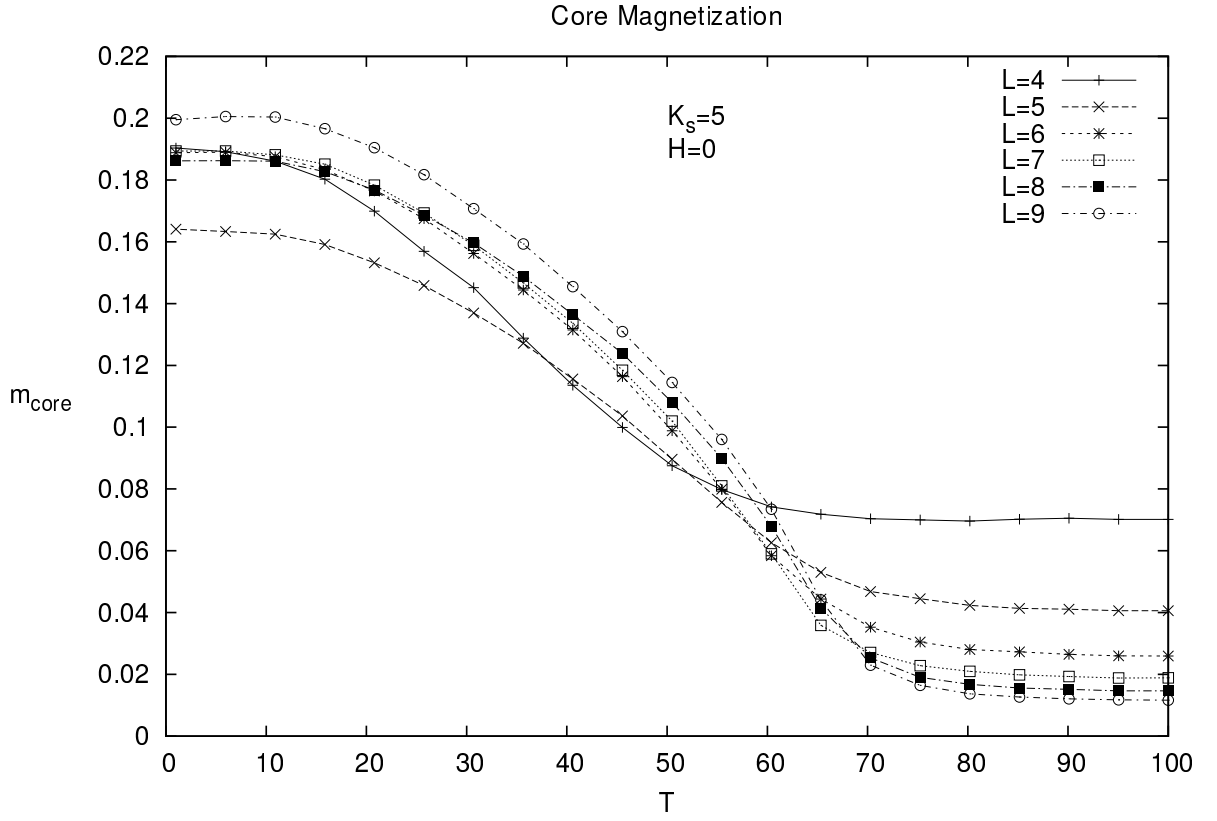


Figure 1.6: The core magnetization of maghemite single nanospheres of different sizes as a function of temperature. The results are obtained using MC simulation from Ref. [37] where the units of temperature, field, and anisotropy are (12.5 K) and the magnetization unit is $5 \mu_B/\text{ion}$. The unit scaling is explained in Appendix. A.

Also, we note that the ratio $T_s/T_c = 0.11 \pm 0.04$ is in good agreement with the ratio $J_{ss}/J_{cc} = 0.1$. It is important to note that the surface ordering temperature is driven by factors other than the exchange interactions between the surface spins, such as finite size effect and the surface-core interaction. As a result, the equation ($T_s/T_c = J_{ss}/J_{cc}$) provides only a qualitative estimate of J_{ss}/J_{cc} .

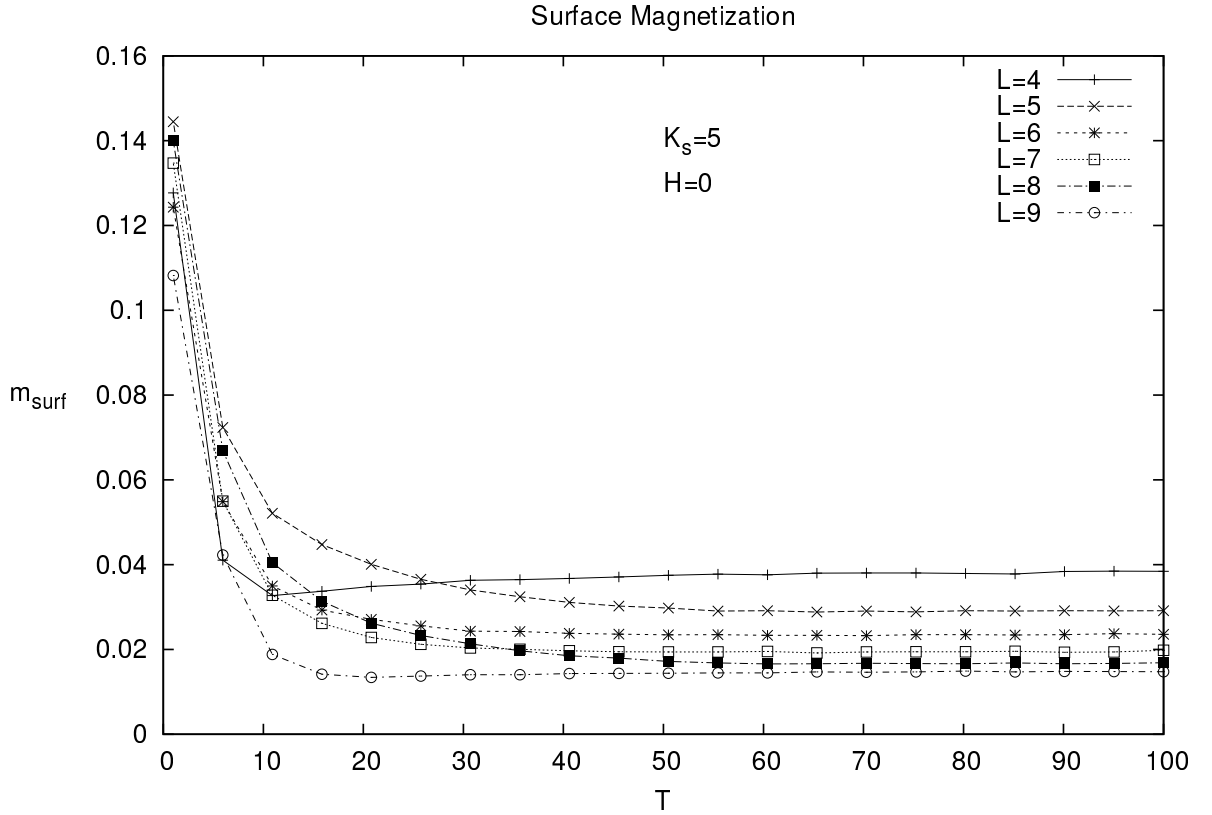


Figure 1.7: The surface magnetization of maghemite single nanospheres of different sizes as a function of temperature. The results are obtained using MC simulation from Ref. [37] where the units of temperature, field, and anisotropy are (12.5 K) and the magnetization unit is $5 \mu_B/\text{ion}$. The unit scaling is explained in Appendix. A.

1.7 Other models

Many studies of magnetic nanospheres have shared the main core-shell principle in their model with some variations. For example, simulations of magnetite nanospheres in Refs. [38, 39] assume that the exchange and the bulk cubic anisotropy are the same for both the surface and the core. The studies define the surface spins as the spins that miss some of their nearest neighbors, whereas the surface anisotropy direction is calculated from each surface spin based on the position of the nearest neighbors as,

$$e_k = \sum_j (P_k - P_j) / |\sum_j (P_k - P_j)|. \quad (1.7)$$

Ref [40] proposed core anisotropy in the Z-direction and radial surface anisotropy. Another model using Neel anisotropy was proposed showing that magnetic nanospheres can be modeled using uniaxial and cubic anisotropy.

Recently, studying systems of interacting nanospheres becomes a matter of interest. The size and the complexity of these systems resulted in a challenge in performing the simulations. Therefore, most of the recent computational studies of magnetic nanoparticles use more simplified models by, for example, assuming each nanosphere as a single dipole with an effective anisotropy [41, 42, 43]

1.8 Outline of the thesis

In the following chapters, we present simulation results using the stochastic Landau-Lifshitz-Gilbert technique. The codes were implemented by Maglua programming environment [44, 45]. It is a scripting language developed by Jason Mercer based on

Lua as an interface scripting language to his LLG code [44, 45]. All the subroutines to perform numerical calculations such as calculating the effective field and performing the LLG time steps are written in C/C++ to take advantage of the computational efficiency of these lower level languages.

Ch. 2 presents the results of stochastic LLG simulations of noninteracting maghemite nanospheres based on the core shell model of Refs. [34, 37] discussed in Section 1.6. The study focuses on the microscopic spin ordering to show how the surface vacancies distribution plays an important role in the magnetic properties of maghemite nanospheres.

Ch. 3 shows the magnetic behavior of dipole FCC arrays using stochastic LLG. The dipole field was calculated assuming periodic boundary conditions using Ewald summation techniques [46].

In Ch. 4, we present multiscale simulation of maghemite nanosphere FCC arrays. The model considers the dipole interactions between the nanospheres and the complex internal spin structure of these nanospheres. The results are compared with the dipole FCC arrays to show the significance of the effect of the internal structure of maghemite nanospheres on the array collective behavior.

In Ch. 5 we give our conclusions regarding the full project with comparison to previous simulations and experiments.

Chapter 2

Noninteracting Maghemite Nanospheres

2.1 Simulation using the stochastic Landau-Lifshitz- Gilbert equation

While MC techniques are very efficient at finding the equilibrium state, they are not able to properly explain the dynamical evolution of the magnetic systems. On the other hand, the stochastic LLG equation has been widely used in simulating dynamic properties of magnetic systems. Such a model is important for studying non-equilibrated systems such as spin-glasses and magnetic hysteresis loops [47].

The stochastic LLG equation is based on Landau-Lifshitz equation that treats the spin like a classical dipole with a damping factor, which results in an additional magnetic torque. The equation of motion for the spin magnetic moment is given by

$$\frac{d\vec{S}}{dt} = -\gamma\vec{S} \times \vec{H}_{\text{eff}} + \lambda\vec{S} \times (\vec{S} \times \vec{H}_{\text{eff}}), \quad (2.1)$$

where γ is the electron gyro-magnetic ratio, and $\lambda = -\alpha\gamma/|S|$ with α the damping factor. The effective field (\vec{H}_{eff}) can be calculated from the energy equation,

$$\vec{H}_{\text{eff}}^i = -\frac{\partial E}{\partial \vec{S}^i} + \vec{H}_{\text{th}}^i, \quad (2.2)$$

where H_{th} is a stochastic magnetic field due to thermal fluctuations given by

$$H_{\text{th}} = \sqrt{\frac{2\alpha K_B T}{\gamma\mu_0 V |\sigma| \delta t}} W. \quad (2.3)$$

Here, V is the volume, δt is the time step and W is a random number with a gaussian distribution that satisfies,

$$\begin{aligned} w \langle W_t W_{t'} \rangle &= \delta(t - t') \\ \langle W \rangle &= 0 ; t \neq t', \end{aligned} \quad (2.4)$$

For convenience we define the time unit $t_u = (B_0\gamma)^{-1}$, where B_0 is some characteristic field value. Choosing $B_0 = 1$ T gives $t_u = 1/\gamma = 5.68 \times 10^{-12}$ sec. The damping factor used in the simulation is $\alpha = 0.5$ and the time step used to integrate the LLG equation is $\Delta t = 2.0 \times 10^{-4} t_u$.

The model and the parameters

The model used for LLG simulations is similar to the one used for MC simulations in the Introduction by Adebayo *et al.* Ref. [37] but for simplicity, the core anisotropy is neglected since it has a very small value compared with the surface anisotropy. Hence the energy used for this model is,

$$E = - \sum_{i \neq j} J_{ij} \vec{S}_i \cdot \vec{S}_j - \sum_{i \in \text{surface}} K_s (\vec{S}_i \cdot \vec{n}_i)^2 - \vec{H} \sum_i \vec{S}_i. \quad (2.5)$$

Table 2.1 shows the exchange parameters that have been used for the stochastic LLG simulations. The parameters are derived from the exchange parameters of $\text{Ni}^{+2}\text{Fe}_2^{+3}\text{O}_4$ by matching (B) and (A) sites in the maghemite with the Fe^{+3} at the octahedral sites and the Fe^{+3} at the tetrahedral sites in $\text{Ni}^{+2}\text{Fe}_2^{+3}\text{O}_4$ [35]. Since the magnetic moment of each spin is normalized to unity, the exchange parameters used in Refs [35] have been multiplied by $5 \times 5 = 25$ (since each ion corresponds to $5\mu_B$). This results in a rescaling of the temperature unit to Kelvin. The nanospheres in the simulation have a 5 nm diameter with a surface thickness of 0.83 nm. The ratio of surface spin exchange to the corresponding core spin exchange is chosen to get a close value to the ratio of the surface ordering temperature to the core ordering temperature obtained from the experimental results in Fig. 1.3.

$$J_{ss}/J_{cc} = T_s/T_c = 0.025. \quad (2.6)$$

2.1.1 Results from simulations

In this section we present the results from a series of simulation studies on ensembles of non-interacting nanospheres. Defining $\vec{S}_i(n)$ as the i^{th} atomic spin on the n^{th} nanosphere, the following quantities are defined. The average magnitude of the

exchange parameter	exchange value ($\times 25$ K)	position	interacting sites
J_{ca-cb}	-28.1	core-core	A-B
J_{ca-ca}	-21.0	core-core	A-A
J_{cb-cb}	-8.6	core-core	B-B
$J_{s_b^a-c_b^a}$	$J_{c_b^a-c_b^a} \times 0.025$	surface-core	A or B – A or B
$J_{s_b^a-s_b^a}$	$J_{c_b^a-c_b^a} \times 0.025$	surface-core	A or B – A or B

Table 2.1: The maghemite nanospheres parameters used in LLG simulations.

magnetic moment of the nanospheres (M_n):

$$M_n = \frac{4}{N} \sum_{n=1}^N \left| \sum_{i=1}^{q_n} \vec{S}_{i(n)}/q_n \right|, \quad (2.7)$$

where N is the number of nanospheres in the ensemble, q_n is the number of spins in the n^{th} nanosphere and $\vec{S}_i(n)$ is the i^{th} spin on the n^{th} nanosphere in the ensemble. Due to the ferrimagnetic structure, a normalizing factor 4 is introduced from Eq. 1.6. This means that in the fully saturated state $M_n = 1$. The average magnetic moment of nanospheres ensemble (M_e) is given by

$$\vec{M}_e = \frac{4}{N} \sum_{n=1}^N \sum_{i=1}^{q_n} \vec{S}_i(n)/q_n. \quad (2.8)$$

The average magnitude of the magnetic moment of the cores (M_c) is given by

$$M_c = \frac{4}{N} \sum_{n=1}^N \left| \sum_{i \in \text{core}}^{q_{cn}} \vec{S}_i(n)/q_{cn} \right|, \quad (2.9)$$

where $\vec{S}_i(n)$ denotes the i^{th} spin in the core of the n^{th} nanosphere in the ensemble and q_{cn} denotes the number of spins in the core of the n^{th} nanosphere. Finally, the

average magnitude of the magnetic moment of the surfaces (M_{srf}) is given by

$$M_{\text{srf}} = \frac{4}{N} \sum_{n=1}^N \left| \sum_{i \in \text{surface}}^{q_{sn}} \vec{S}_i(n)/q_{sn} \right|, \quad (2.10)$$

where q_{sn} denotes the number of spins in the surface of the n^{th} nanosphere.

For comparison purposes, two ensembles consisting of 1000 non-interacting spheres were studied. The two ensembles had different values of K_s , but identical in all other aspects (the size, the series of random numbers used to generate the vacancies and the stochastic field, etc...). One ensemble was given a value of $K_s = 5 \text{ K} = 1.29 \times 10^{-24} \text{ J}$, the other $K_s = 10 \text{ K} = 2.58 \times 10^{-24} \text{ J}$. We will refer to these ensembles as K5 and K10, respectively. Table 2.2 lists the properties of the ensembles studied in this chapter.

Ensemble	K5	K10	Dc63	Dc675
The surface anisotropy, K_s (K)	5	10	10	10
The diameter of the nanospheres, D (nm)	5	5	7.5	7.5
The core diameter, D_c (nm)	3.67	3.67	6.3	6.75
The number of spheres (N)	1000	1000	512	512
Core volume/nanosphere volume	0.4	0.4	0.59	0.73

Table 2.2: Characteristic parameters of the ensembles K5, K10, Dc63, and Dc675.

The ensembles were initialized with the same random spin configuration. They were then equilibrated at an initial temperature of 1000 K in a field $H = 5 \text{ K} = 1.49 \text{ T}$ and then cooled at a rate of $1 \text{ K}/t_u = 1.76 \times 10^{11} \text{ K/sec}$.

Figs .2.1 and 2.2 show the core magnetization of the individual nanospheres, as defined by Eq. 2.9, as a function of temperature. We can see that the core spins begin to order at a temperature close to that of bulk maghemite, and this temperature is independent of the K_s . The data also show that the core spins are fully ordered at $T = 0$ K. On the other hand, the surface spins do not order until a much lower temperature as shown in Fig. 2.3 due to the lower value of the surface exchange interactions. We also note that the surface spins in the two ensembles do not fully saturate at $T = 0$ K. As we will show, this occurs as a consequence of the frustration that arises due to the competition between the surface anisotropy and the exchange interactions.

The results for M_n , M_c and M_{srf} as defined in Eqs. 2.7, 2.9 and 2.10 show that the surface spins contribute significantly to the total magnetization at low temperature as expected by comparing the size of the core with the size of the nanosphere. These results are consistent with the earlier MC simulations discussed in the Introduction [37].

To compare the low temperature surface magnetization for $K_s = 5$ K with $K_s = 10$ K, the surface magnetization for both the K5 and K10 ensembles is presented in Fig 2.3. The data show that in both cases the surface spins begin to order at $T_s \simeq 30$ K. Both the transition temperature and the surface magnetization show little dependence on the value of the surface anisotropy down to approximately $T \simeq 20$ K and it is only at $T \simeq 15$ K, that the data start to diverge. The difference between the surface magnetization for the two data sets increases as the temperature decreases.

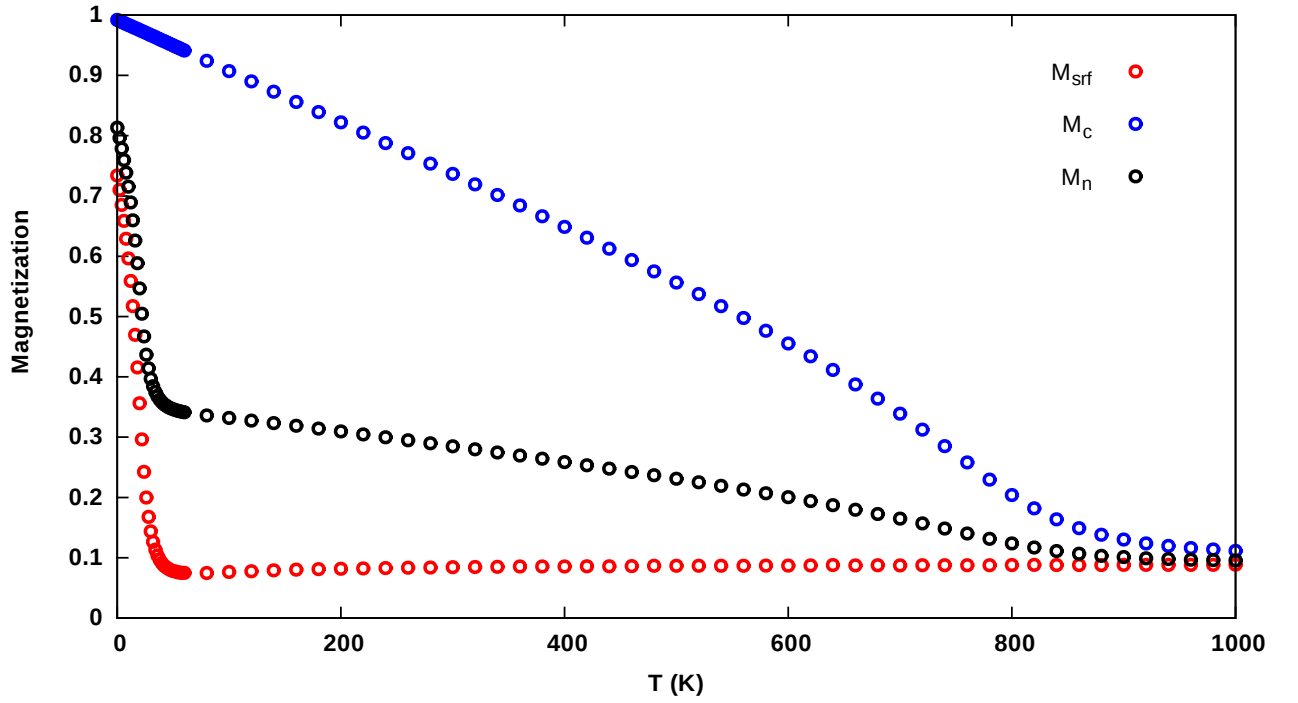


Figure 2.1: The average magnitude of the core magnetization (M_c), magnitude of the surface magnetization (M_{srf}) and the magnitude of the magnetization of the nanosphere (M_n) as functions of temperature. The data represents the K10 ensemble cooled in $H_z = 5$ K (1.49 T). K10 consists of 1000 maghemite nanospheres of $D = 5$ nm, diameter, $D_c = 3.67$ nm core diameter and $K_s = 10$ K (2.58×10^{-23} J).

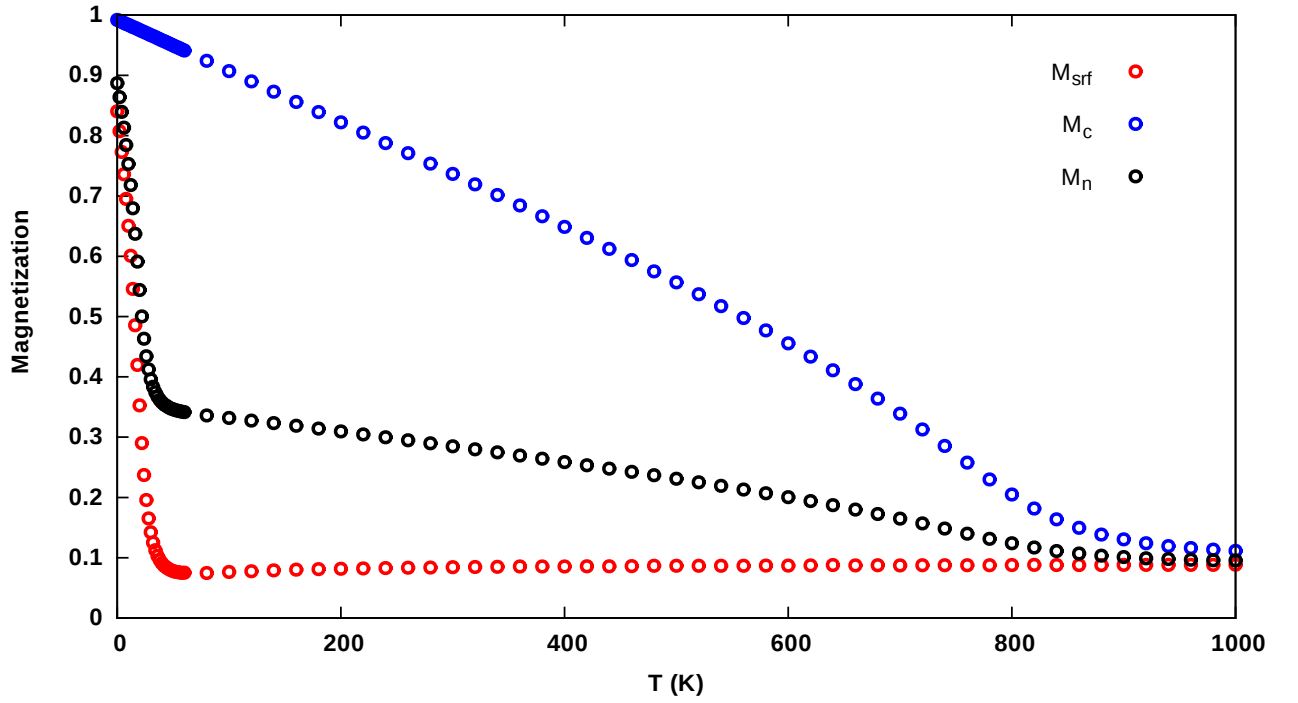


Figure 2.2: The average magnitude of the core magnetization (M_c), magnitude of the surface magnetization (M_{srf}) and the magnitude of the magnetization of the nanosphere (M_n) as functions of temperature. The data represents the K10 ensemble cooled in $H_z = 5$ K (1.49 T). K5 consists of 1000 maghemite nanospheres of $D = 5$ nm diameter, $D_c = 3.67$ nm core diameter and $K_s = 5$ K (1.29×10^{-23} J).

We observe that, while both data sets do not show full ordering of the surface spins at $T = 0$ K, the surface magnetization for $K_s = 10$ K ($M_{\text{srf}} \simeq 0.79$) is lower than the corresponding value for $K_s = 5$ K ($M_{\text{srf}} \simeq 0.89$). This is due to the fact that the higher value of K_s increases the frustration of the surface spins.

Finally we note that while the value of $T_s/T_c \simeq 0.03$ is close to the ratio of $J_{s-s}/J_{c-c} = 0.025$, it is not identical. We attribute this to the effect of the core-surface exchange interaction and finite size effects.

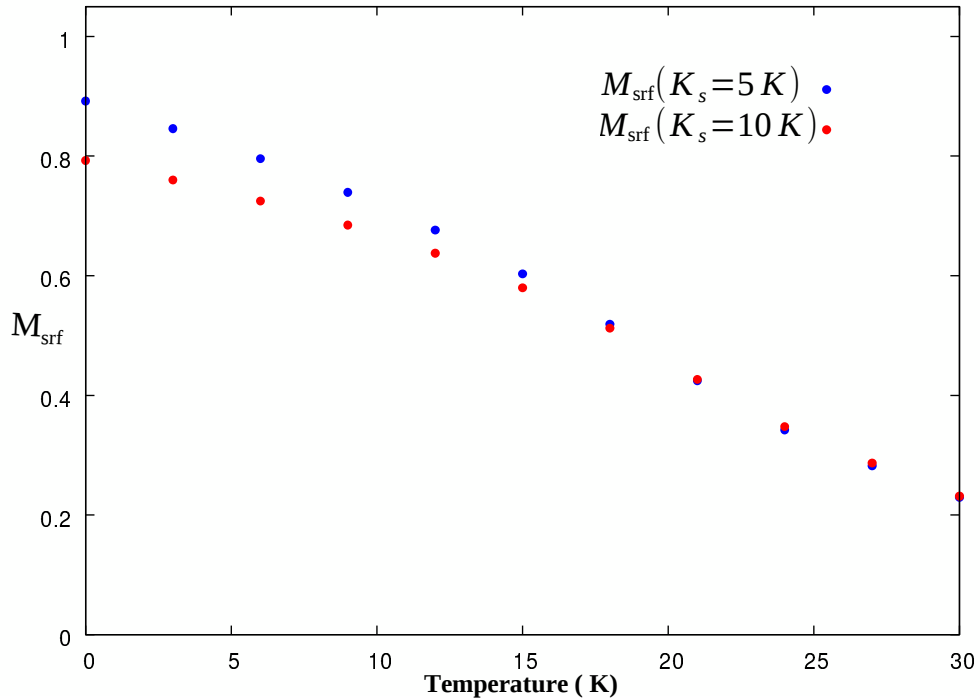


Figure 2.3: M_{srf} for different anisotropies as a function of temperature. The results from cooling the K5 and K10 ensembles, with $H = 5$ K.

Fig. 2.4 shows the temperature dependence of M_z (the z-component of \vec{M}_c as defined in Eq. 2.8) of the K10 ensemble as it is cooled in a field of ($H_z = 5$ K (1.49 T)).

Also shown is a plot of the average magnitude of the nanospheres (M_n). We note that the data are mostly identical. This indicates that a field of $H_z = 5$ K is sufficient to completely align the magnetic moment of each of the nanospheres in the direction of the field for $T < 100$ K. Similar comparison for the K5 ensemble shows that this also applies to the $K_s = 5$ K case.

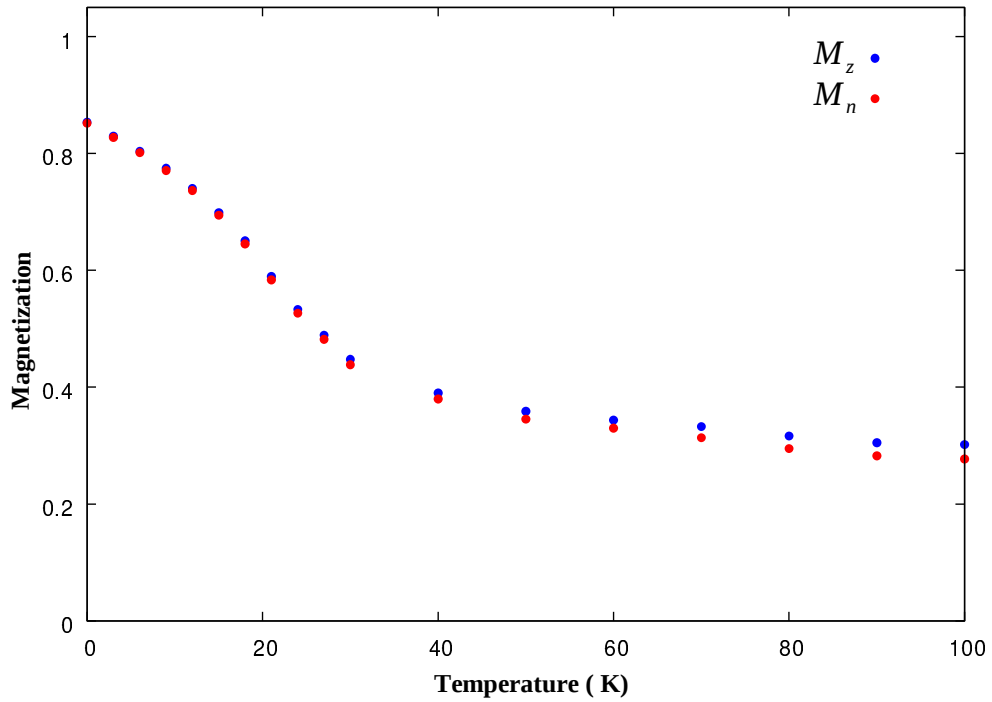


Figure 2.4: M_z and M_n as a function of temperature for cooling the ensemble K10 under a magnetic field $H_z = 5$ K.

2.2 Blocking temperature

By cooling the ensemble in zero field, the net magnetization of the ensemble will effectively be zero. We will refer to this state as a zero field cooled (ZFC) ensemble. By heating and then cooling in a field, as described in the experiments discussed in the Introduction, we can identify the blocking temperature as the point of divergence between the two curves.

Fig. 2.5 shows the heating and cooling magnetization (M_z) of a ZFC ensemble consisting of 1000 non-interacting nanospheres under $H_z = 0.4$ K (0.12 T) as a function of temperature. Each nanosphere has a 5 nm diameter, 3.67 nm core diameter and surface anisotropy of $K_s = 10$ K (the ensemble, K10). The ensemble cooled in zero field to $T = 0$ K then heated and cooled in an external field magnetic field of $H_z = 0.4$ K in the z-direction where the cooling and heating rate is 0.1 K/ t_u . The cooling and heating curves are mostly identical above $T \geq 20$ K. From this we estimate a blocking temperature of $T_B \simeq 20$ K.

Fig. 2.6 shows the heating and cooling magnetization of the ZFC ensemble K5. The heating and cooling rate is 0.1 K/ t_u and the applied field is $H_z = 0.4$ K. The blocking temperature in the K5 ensemble is about 12 K. This reduction in the blocking temperature with reducing the surface anisotropy is consistent with Arrhenius-Neel law [48].

Fig. 2.7 compares the data in Fig. 2.5 with the data of the same ensemble using different cooling and heating rates. A smaller rate gives a longer time for the ensemble to relax and hence to get closer to the equilibrium state. As a result, a smaller heating and cooling rate gives a lower blocking temperature.

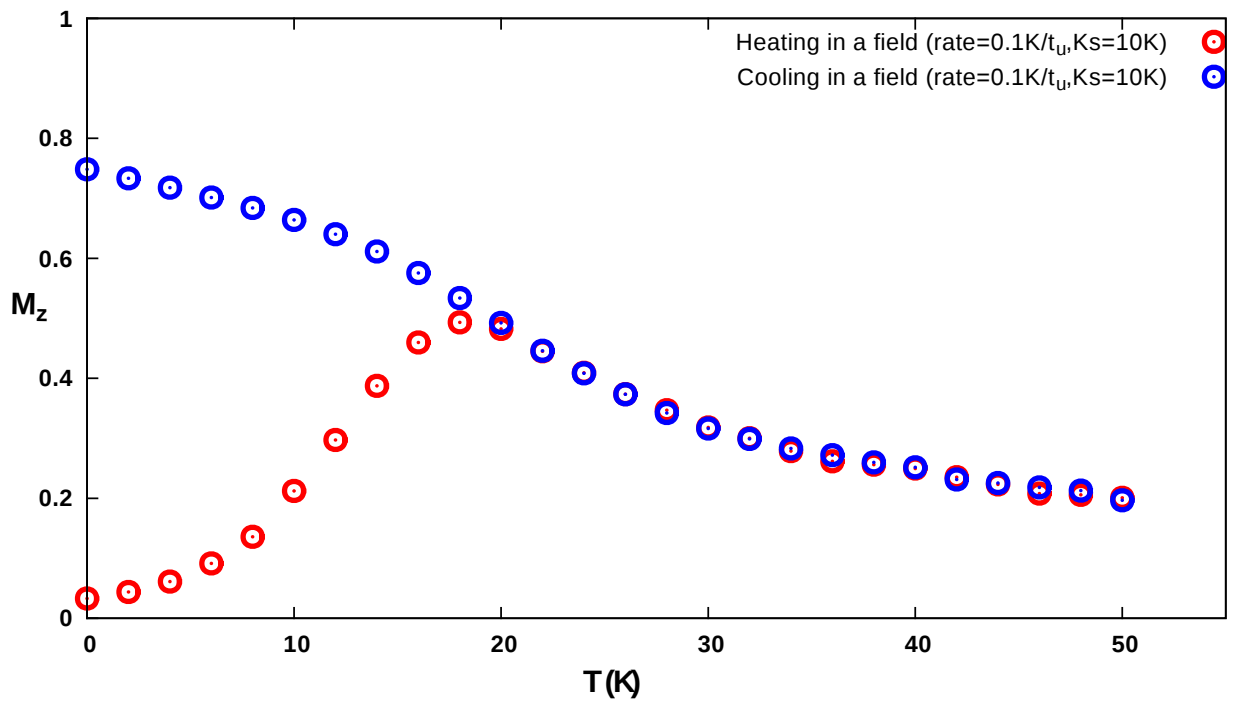


Figure 2.5: Data showing the magnetization of the zero field cooled ensemble K10 (Table 2.2) during the heating and then the cooling processes under an applied field of $H_z = 0.4$ K (0.12 T) where the heating and cooling rate is $0.1K/t_u$ (1.76×10^{11} K/sec).

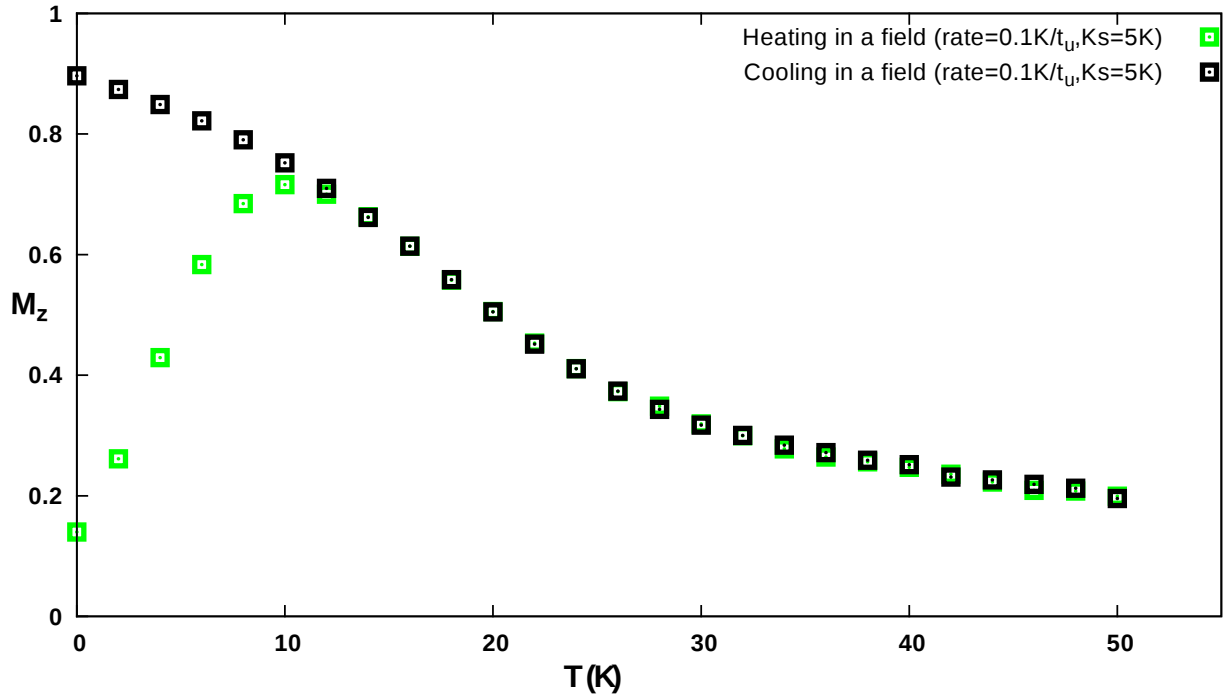


Figure 2.6: The magnetization of the zero field cooled ensemble K5 (Table 2.2) during the heating and then the cooling processes under an applied field of $H_z = 0.4\text{K}$ (0.12 T) where the heating and cooling rate is $0.1\text{ K}/t_u$ ($1.76 \times 10^{11}\text{ K/sec}$).

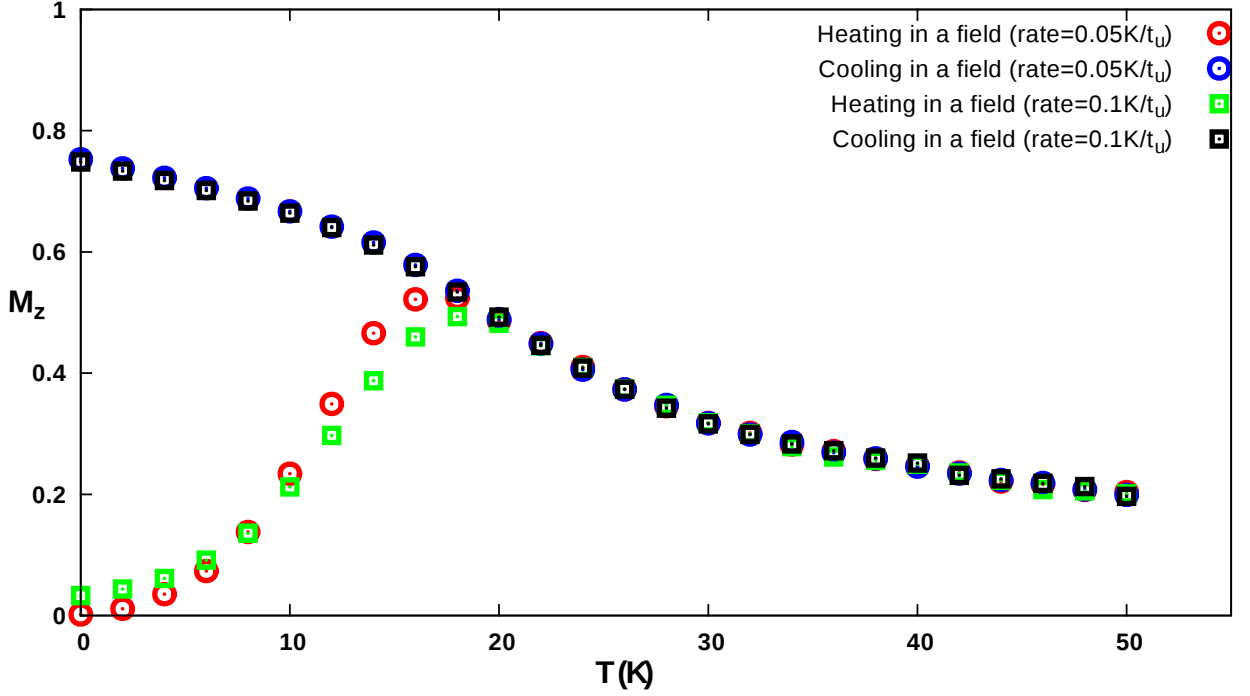


Figure 2.7: The magnetization of the zero field cooled ensemble K10 (Table 2.2) during the heating and then the cooling processes under an applied field of $H_z = 0.4$ K (0.12 T). The data compares a heating and cooling rate of 0.1 K/ t_u (1.76×10^{11} K/sec) with a rate of 0.05 K/ t_u .

The total cooling and heating rates of the LLG simulations performed here are of the order of ($0.1K/t_u \simeq 1.8 \times 10^{11}K/sec$) which is very small and the applied field $H_z = 0.4$ K (1200 Oe) is very large. Unfortunately, the blocking temperature is related to the heating and cooling rates as shown in Fig. 2.7 and to the applied field [20]. Comparing with the experiments in [20] (the heating and cooling rates are of the order of 1 K/min and the applied field is of the order of 1 Oe [49]), the parameters we

used in the simulation are far from being ideal. Hence a different method is required to determine the blocking temperature in order to compare it with the experimental results.

2.3 The microscopic spin ordering

In the preceding section we focus on the average magnetic properties of nanospheres. However, the simulation studies also reveal more information about the internal spin configuration within the nanospheres. A typical spin configuration for one of the nanospheres with $K_s = 5 \text{ K}$, with a field $H_z = 5 \text{ K}$ at $T = 5 \text{ K}$ is shown in Fig. 2.8. Fig. 2.9 shows a simplified version of the spins configuration. For simplicity, only B-sites are included in Fig. 2.9, since A-sites are aligned in the opposite direction.

While the results show that the magnetization in the core spins saturate at $T = 0 \text{ K}$, this is not the case for surface spins. This is a consequence of the frustration that arises from the competition between the radial surface anisotropy and the exchange interactions. The minimal energy due to the anisotropy is reached when the surface spins are aligned radially while the minimal energy due to the exchange corresponds to the spins aligned parallel to the magnetic axis of the nanosphere. Hence this frustration and disorder is maximum at the equator (we will refer to the magnetic equator by the equator).

Fig. 2.10 provides a more detailed illustration of the spin configuration for a $K_s = 5 \text{ K}$ nanosphere at $T = 0 \text{ K}$ by plotting the radial component of the direction of each spin (with A-sites spins rotated 180°) as a function of $\cos(\varphi)$, where, φ is the angle

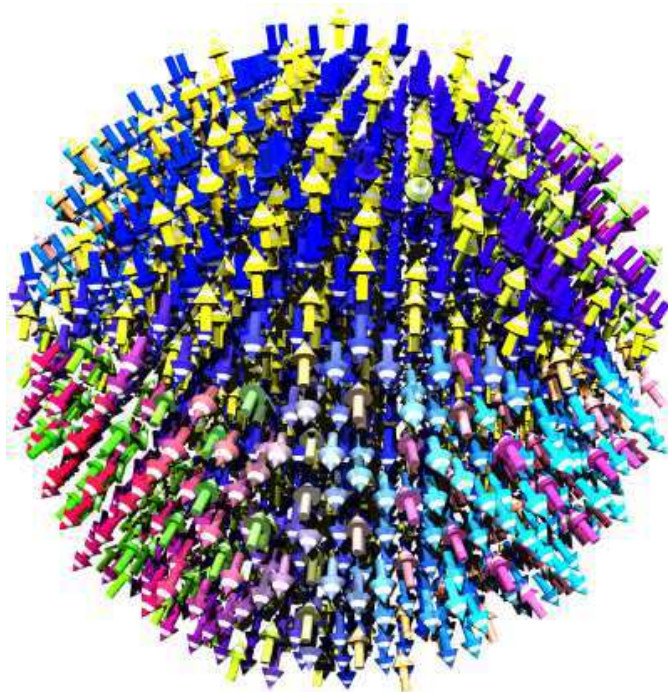


Figure 2.8: Spin configuration of a single nanosphere at $T = 0$ K, $K_s = 5$ K, and $H_z = 5$ K.

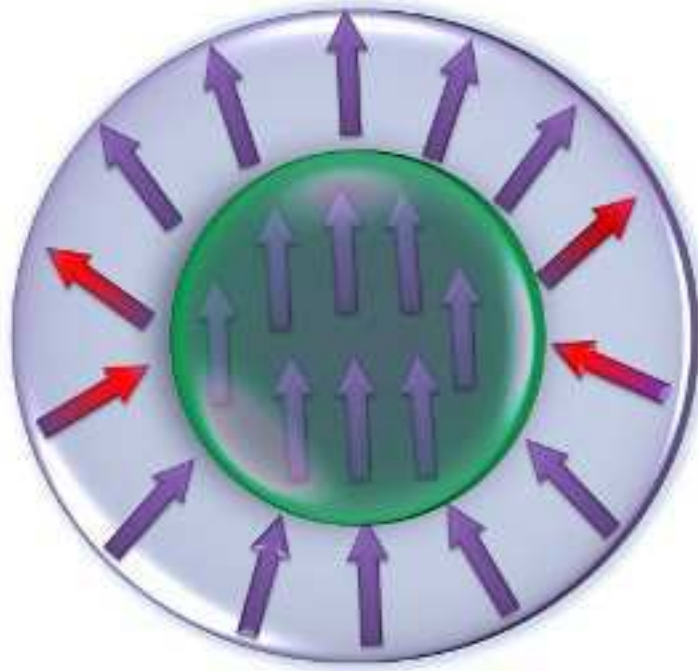


Figure 2.9: Simplified spin configuration of a single nanosphere at $T = 0$ K.

between the vector connecting the center of the nanosphere with the spin location and the magnetic moment of the nanosphere. Each point in the figure represents a spin. When a spin is directed toward the north pole, the radial component of the spin is equal to $\cos(\varphi)$; this means that the straight line $Y = X$ indicates that the spins are aligned along the net magnetic moment of the nanosphere. From this, we see that the core spins are aligned ferrimagnetically as in bulk maghemite.

The points to the right of the vertical axis ($\cos \varphi > 0$) correspond to the spins in the northern hemisphere while the points to the left of the vertical axis ($\cos \varphi < 0$) correspond to the spins in the southern hemisphere. From this, we see that most of the surface spins in the vicinity of the (magnetic) north pole are pointing more or less radially outward and those at the (magnetic) south pole are pointing more

or less radially inward. The extent of this configuration at the equator results in an anti-parallel ordering where there is a strong shift in the surface spins direction from inward at the southern side to outward at the northern side. This switch forms a domain wall at the magnetic equator of each nanosphere (at the surface). These domain walls arise as a consequence of the competition between the surface anisotropy that prefers to align the spins radially outward or inwards, and the exchange field of the core that prefers to align the spins parallel to the magnetic axis. Due to this competition, the domain walls have higher energy than the rest of the nanosphere.

On the other hand, close to the equator we see that there are some surface spins in the northern hemisphere pointing radially inward and spins in the southern hemisphere pointing radially outwards. These reversed spins are in a metastable state where the anisotropic energy is minimized due to the radial orientation of spins, but the exchange energy is not minimized as these spins are anti-parallel to the neighboring spins. This metastable state is more likely to be filled in the domain wall and therefore it is reasonable to associate the width of the reversed spins area with the width of the domain wall. The reversed spins in Fig. 2.10 are represented by the points in the upper left and the lower right quarters of the figure.

Fig. 2.11 shows the radial components of the spins of a nanosphere with a diameter of $D = 5$ nm, a core diameter $D_c = 3.67$ nm and surface anisotropy $K_s = 5$ K. Each sub-figure is for a different temperature. The nanosphere has been cooled in zero field with a cooling rate of 0.1 K/ t_u . By comparing the configurations at different temperatures, we can see that the higher the temperature is, the wider the reversed spins region is. Hence, the domain wall gets wider with increasing the temperature.

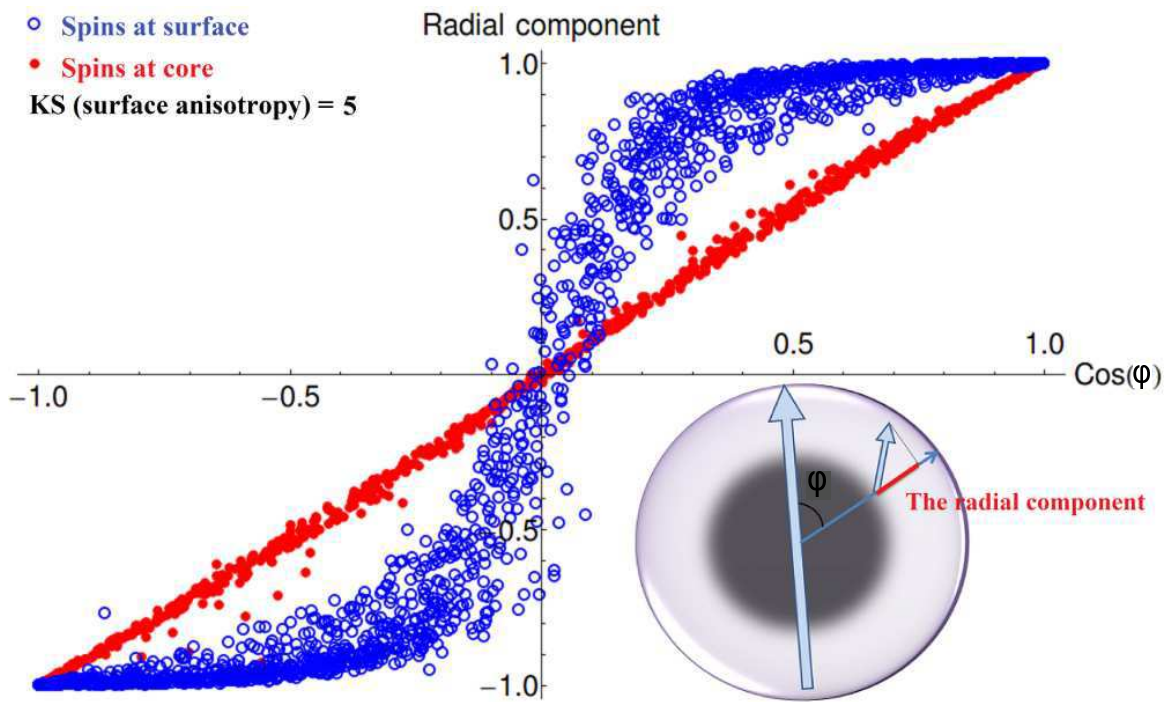


Figure 2.10: The radial component of each spin of a single nanosphere with 5 K at $T=0$ K.

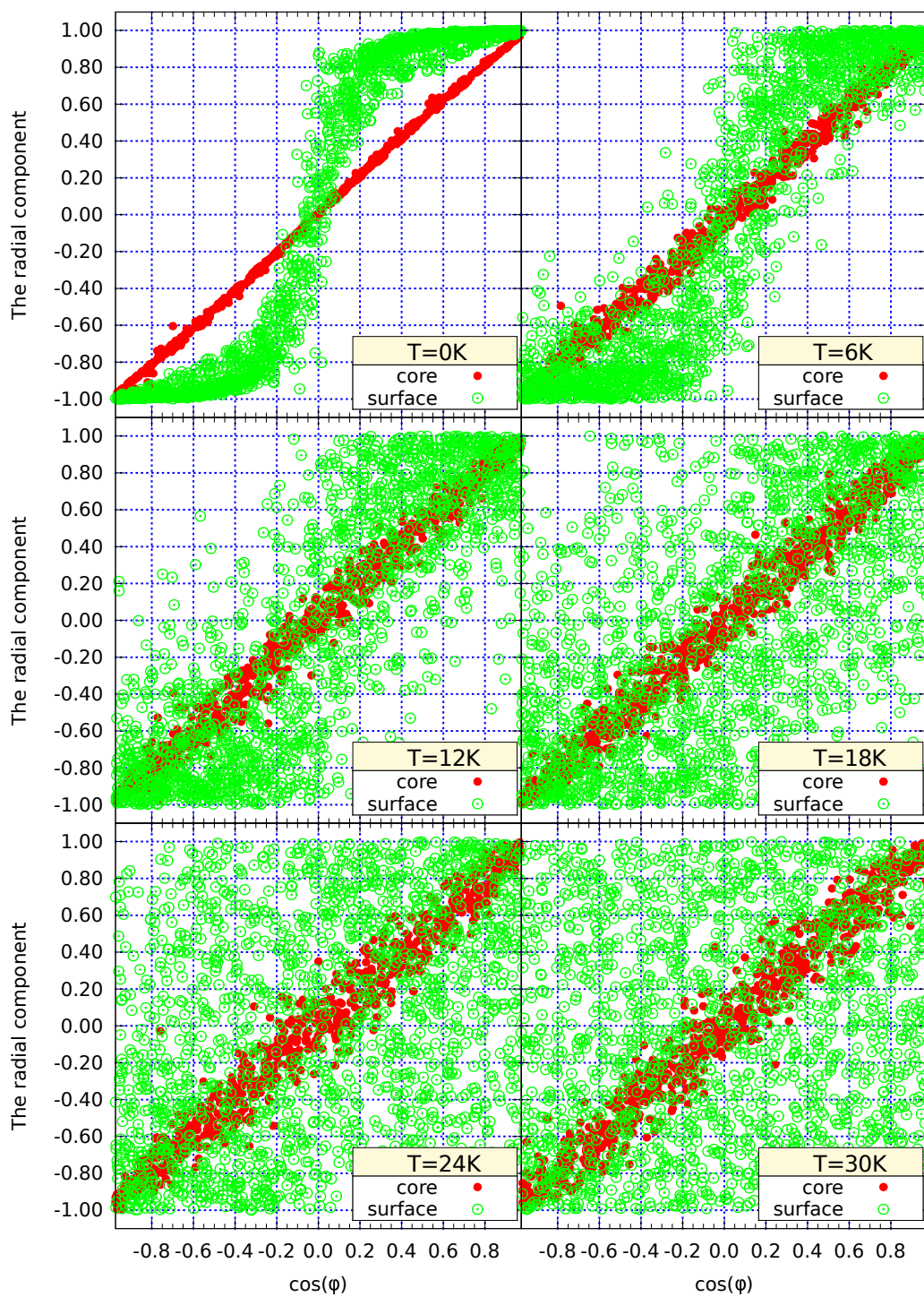


Figure 2.11: The radial component of each spin in a single nanosphere at different temperatures. The nanosphere has $D = 5$ nm, $D_c = 3.67$ nm and $K_s = 5$ K cooled in zero external field.

Fig. 2.12 shows the radial components of a nanosphere with diameter $D = 5$ nm, core diameter $D_c = 3.67$ nm and surface anisotropy $K_s = 10$ K. Each sub-figure is for a different temperature. The nanosphere has been cooled in zero field with a cooling rate of $0.1 \text{ K}/t_u$. As compared with Fig. 2.11, Fig. 2.12 shows that increasing the surface anisotropy increases the surface spins radial components.

Fig. 2.13 shows the density of the reversed spins as a function of $\cos(\varphi)$ for both ensembles (K5 and K10) at different temperatures. Since each nanosphere has a unique direction of the magnetic moment, converting to spherical coordinates for each nanosphere was performed before averaging the reversed spins densities over the ensemble. Both of the ensembles K5 and K10 were cooled in zero field with a cooling rate of $0.1 \text{ K}/t_u$. The data shows that, regardless of the temperature, at least 45% of the spins at the equator ($-0.01 < \cos(\varphi) < 0.01$) are reversed. At $T = 0$ the data show that the density of the reversed spins is narrowly peaked at the equator for both K5 and K10 ensembles indicating a narrow domain wall. As the temperature increases the region of reversed spins around the equator becomes larger, until at $T \approx 24$ K for the K5 ensemble and $T \approx 30$ K for the K10 ensemble, where the spins in the equator vicinity are completely disordered (with 50% of the spins are reversed) while a high proportion ($\approx 35\%$ of the spins are reversed) at the north and the south poles. Thus, at low temperature, the reversed spins area is confined to a narrow region around the (magnetic) equator. As the temperature is increased the reversed spins area extends over a larger portion of the surface of the nanosphere due to the thermal fluctuations of the spins. Similarly, the width of the domain wall increases with increasing the temperature and decreases with increasing the surface anisotropy.

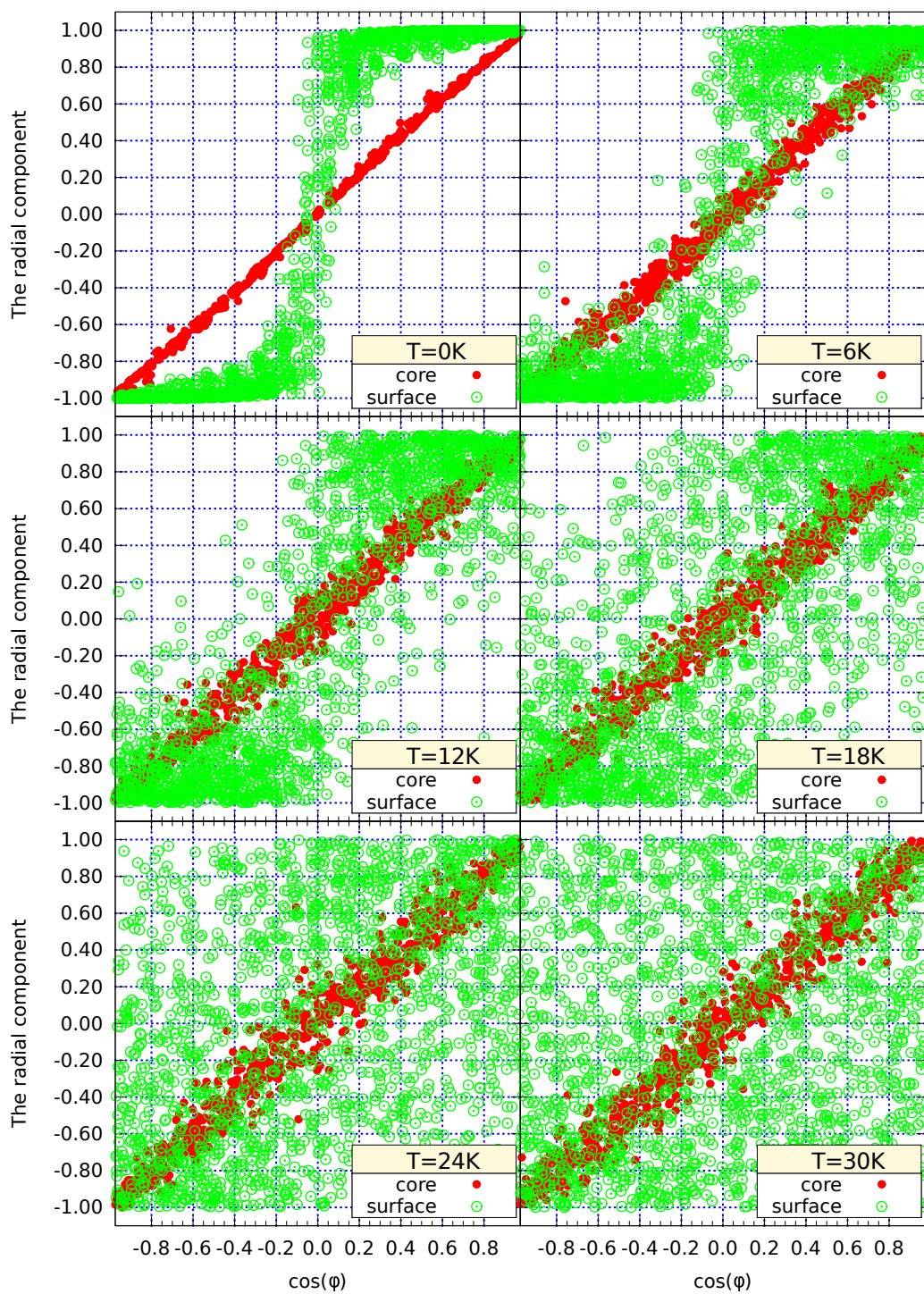


Figure 2.12: The radial component of each spin in a single nanosphere at different temperatures. The nanosphere has $D = 5$ nm, $D_c = 3.67$ nm and $K_s = 10$ K cooled in zero external field.

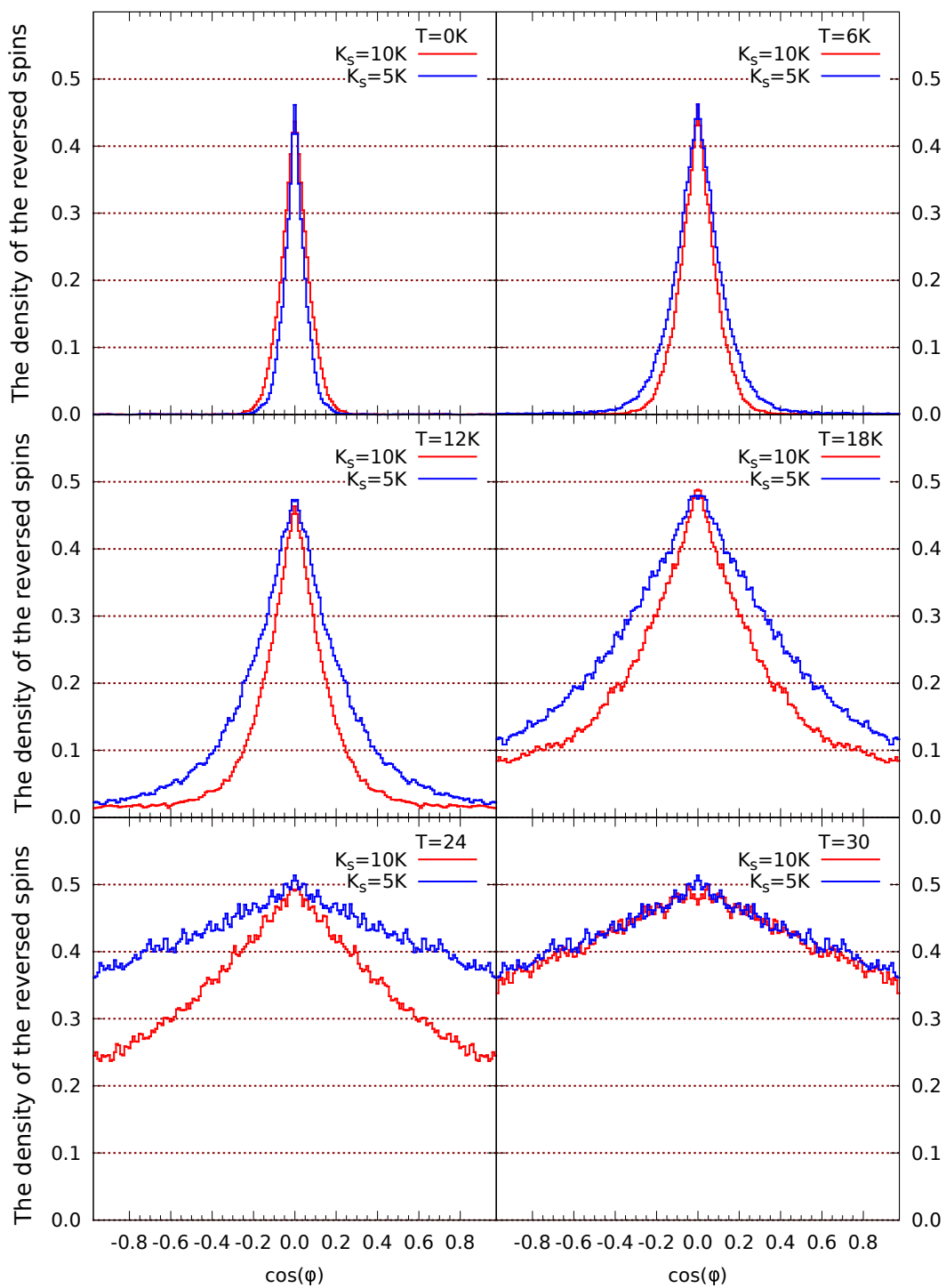


Figure 2.13: The polar distribution of the reversed spins as a function of $\cos(\varphi)$ at different temperatures. The results are from the K5 and the K10 ensembles cooled in zero field.

2.4 The effect of the surface vacancies

The vacancies on the B-sites are distributed randomly across each nanosphere and hence each nanosphere has a unique distribution of the vacancies where some areas on the surface have higher density of vacancies than other areas. Because of the frustration, the surface spins at the equator have a higher energy than the others, and hence the energy of the nanosphere is minimum when the highest density of vacancies are located at the equator.

Fig. 2.14 shows the density of the surface vacancies of the ensemble K5 as a function of $\cos(\varphi)$ at different temperatures, where φ is the angle between the magnetic axis connecting the north and south poles of the nanosphere and the line connecting the site of the surface vacancy and the center of the nanosphere. The ensemble has been zero-field cooled at a rate of $0.1 \text{ K}/t_u$. After calculating the density of the surface vacancies as a function of $\cos(\varphi)$ (according to the magnetic moment of each nanosphere), the densities are then averaged over the whole ensemble. Fig. 2.14 indeed shows that the vacancy distribution of the vacancies is concentrated at the equator at low temperatures.

Because of the high frustration energy at the equator, each nanosphere minimizes the energy by maximizing the number of vacancies at the equator. Since the vacancy distribution of each nanosphere is fixed, each nanosphere lowers the frustration energy at the equator by rotating the magnetization axis of a nanosphere. An individual nanosphere can therefore reduce its energy by aligning its magnetic moment so that the equator is located in the region where the concentration of the surface vacancies is the highest. The inhomogeneous distribution of vacancies therefore gives rise to an

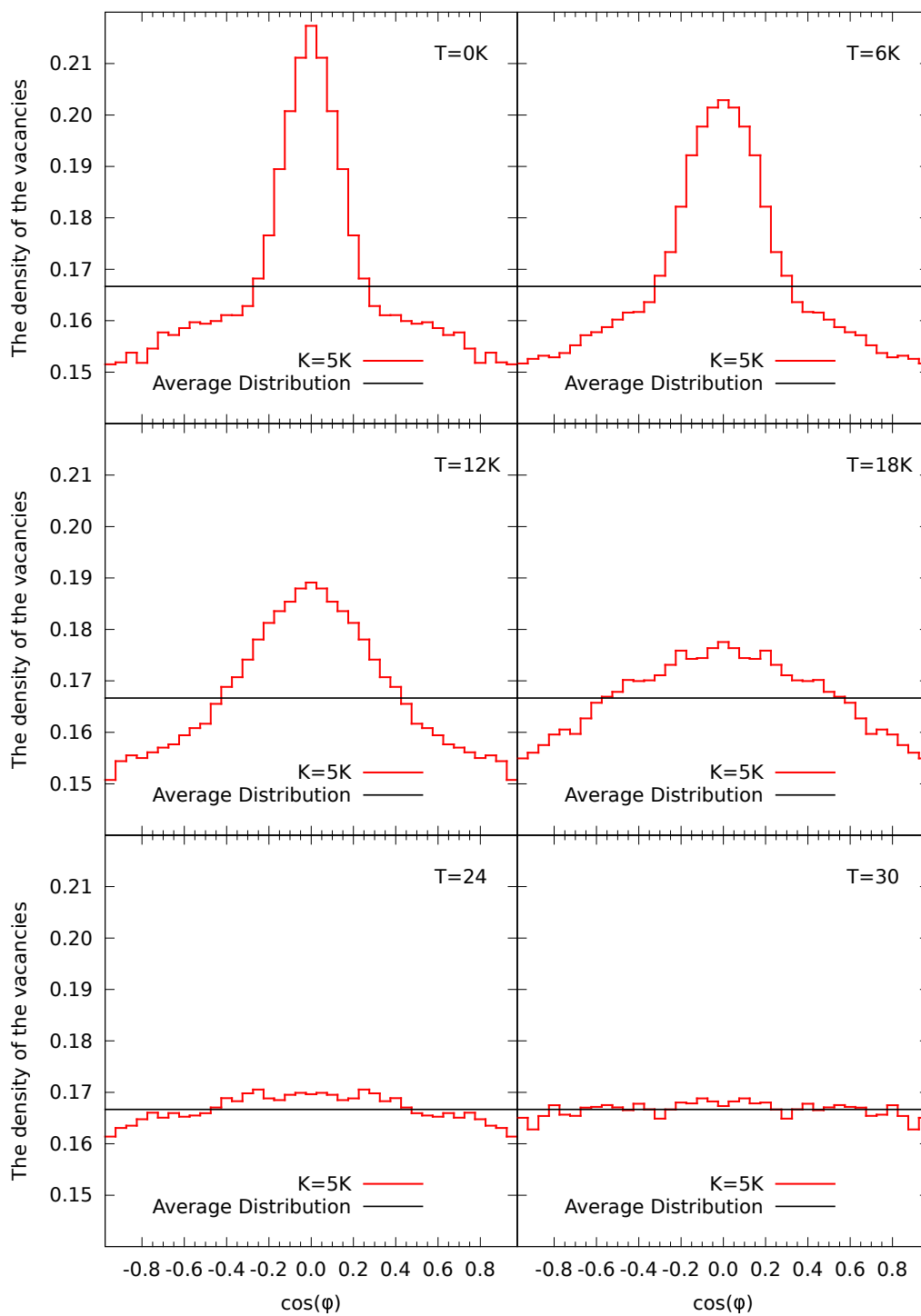


Figure 2.14: The polar distribution of surface vacancies of the ensemble K5 as a function of $\cos(\varphi)$ at different temperatures. The ensemble has been cooled with rate of $0.1 K/t_u$ under zero external field.

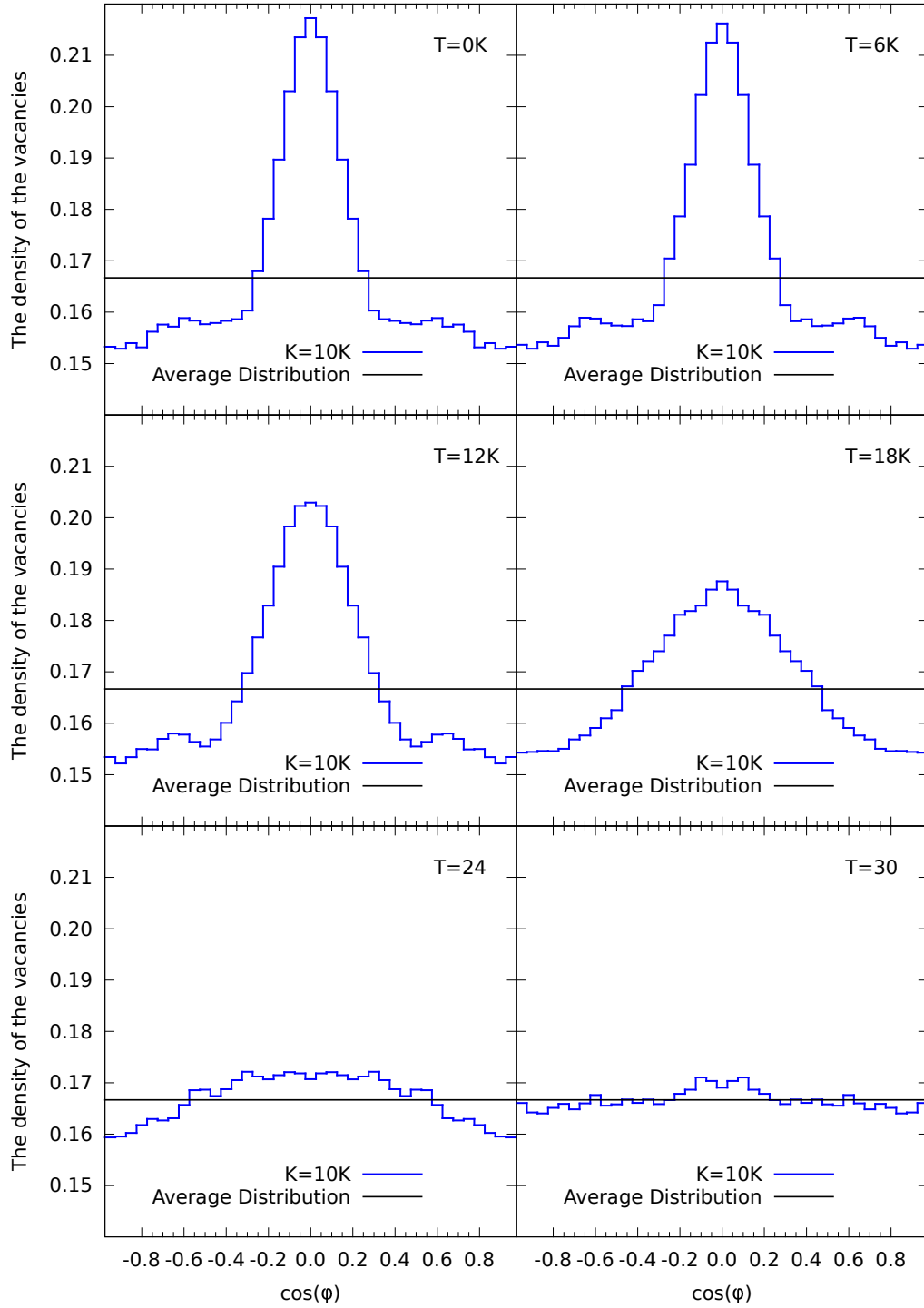


Figure 2.15: The polar distribution of surface vacancies of the ensemble K10 as a function of $\cos(\varphi)$ at different temperatures. The ensemble has been cooled with rate of $0.1 \text{ K}/t_u$ under zero external field.

effective torque acting on the magnetic moment of the nanosphere.

Another way of representing the effect of the vacancies is to recognize that any change in the orientation of the magnetic moment of the nanosphere must be associated with a displacement of the domain wall at the magnetic equator of the nanosphere. The effect of the inhomogeneity in the distribution of the surface vacancies is therefore to pin the domain wall, hindering the motion of the magnetization axis. At high temperatures, thermal fluctuations unpin the domain wall and the nanosphere behaves like a superparamagnet. However, as the temperature is lowered, the domain wall pinning begins to limit the amount of phase space that the nanosphere can access. This results in the domain wall at the equator being trapped in a region high in the density of the surface vacancies. Obviously, there is a relationship between the temperature at which the unpinning occurs and the blocking temperature discussed previously, although the precise nature of this relationship is elusive.

Fig. 2.16 compares the data from Fig. 2.15 and Fig. 2.14 for K10 and K5, respectively. For $T = 0$ K, the direction of the magnetic moment of each nanosphere is dominated only by the surface vacancy distribution. As a result, the vacancies distributions are almost identical at $T = 0$ K. With increasing the temperature, the K10 ensemble shows higher density at the equator and narrower peak than the K5 ensemble. This means that the pinning effect increases with increasing the surface anisotropy. This is because of the fact that thermal fluctuations have to overcome an energy difference between the energy of the state of maximum number of vacancies at the domain wall and the energy corresponding to some other random direction of the magnetic moment. This energy difference and hence the pinning effect increases

with increasing the surface anisotropy. The pinning disappears for the low anisotropy case at $T = 30$ K while remaining for the high anisotropy ensemble.

The cumulative density of vacancies (CDV) is defined as the percentage of surface vacancies in the range between φ and $\pi - \varphi$. To calculate CDV, the surface of each nanosphere was divided into 200 slices each of them has the same number of surface spins similar to what has been done to calculate the angular vacancies distribution where the first two slices contains 1% of the surface spins ($P_s = 0.01$) where these spins are located around the magnetic equator line. The number of vacancies at the surface slice that has the lowest vacancy density was subtracted from the number of vacancies at each slice before calculating CDV to obtain graphs that emphasize the variation of the vacancies distribution.

Fig. 2.17 shows the cumulative density of vacancies of the ensembles K5 as a function of P_s (the ratio of the surface spins allocated around the magnetic equator to the total number of the surface spins) at different temperatures. Also three lines are shown in the graph. One line represents the area corresponding to the peak of density of the vacancies (defined from Fig 2.14). Another line represents the CDV at that area. The third line (black) shows the CDV in case of no correlation between the direction of the magnetic moment and the vacancies distribution. This means the black line represents the CDV for a homogeneous polar distribution of the surface vacancies of the ensemble. Similar data for the K10 ensemble is presented in Fig. 2.18. As we can see from Figs. 2.17 and 2.18, the CDV is practically above or equals the homogeneous value at any temperature up to 30 K and for any size of surface area around the equator. At $T = 30$ K, the CDV approaches the homogeneity line of the angular distribution of the surface vacancies of the ensemble and shows a very weak

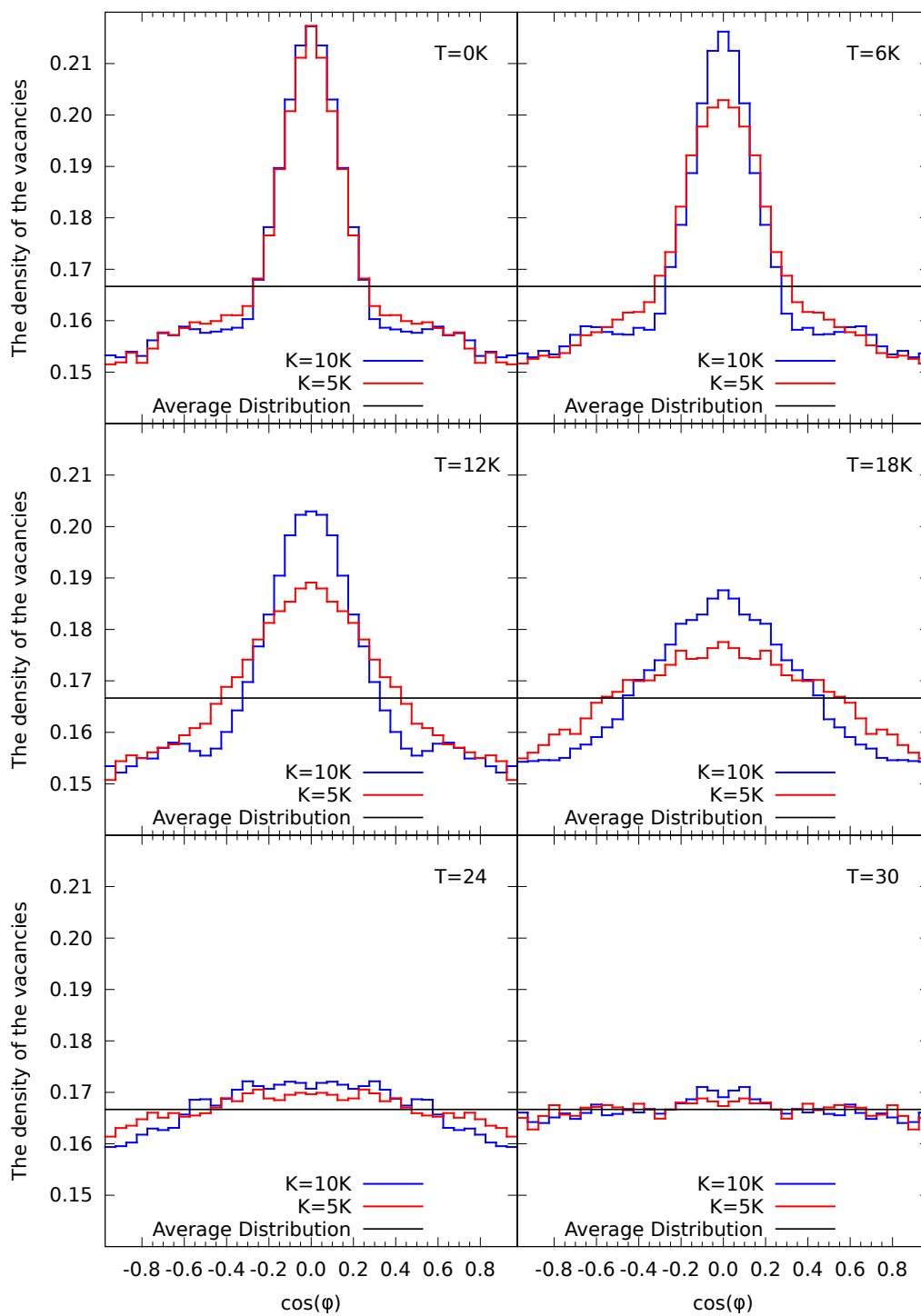


Figure 2.16: The polar distribution of surface vacancies for the ensembles K10 and K5 as a function of $\cos(\varphi)$ at different temperatures. The ensembles have been cooled with rate of $0.1 \text{ K}/t_u$ under zero external field.

tendency of the magnetic moment to favor any direction. This means that each of the maghemite nanospheres from the K5 and the K10 ensembles can be approximated as a simple magnetic dipole above $T = 30$ K .

By looking at the line corresponding to the area of the vacancies peak at $T = 0$ K, we can see that the CDV is the same at that area for any temperature up to almost 12 K for the K10 ensemble and up to 8 K for the K5 ensemble. This means that vacancies distribution controls the magnetic moment direction strongly and the thermal fluctuation takes almost no effect on the direction of the magnetic moment in these ranges of temperature. Rapid decreasing in CDV takes place by increasing the temperature from 12 K to 24 K for K10 and from 8 K to 20 K for K5. The CDV approaches the line of the average vacancies distribution and the direction of the magnetic moment is controlled by thermal fluctuations rather than the vacancies distribution. This means that the nanospheres can be considered practically superparamagnets at temperatures higher than 30 K.

2.5 The effect of the surface thickness

In the previous section we discussed the effects of increasing the surface anisotropy and its relation to of the pinning effect of the magnetic moment of the nanospheres. Increasing the surface thickness also increases the ratio of the anisotropy energy to the total energy and hence we would expect the pinning effect to be more pronounced in nanospheres with a thick surface than nanospheres with a thin surface. In this

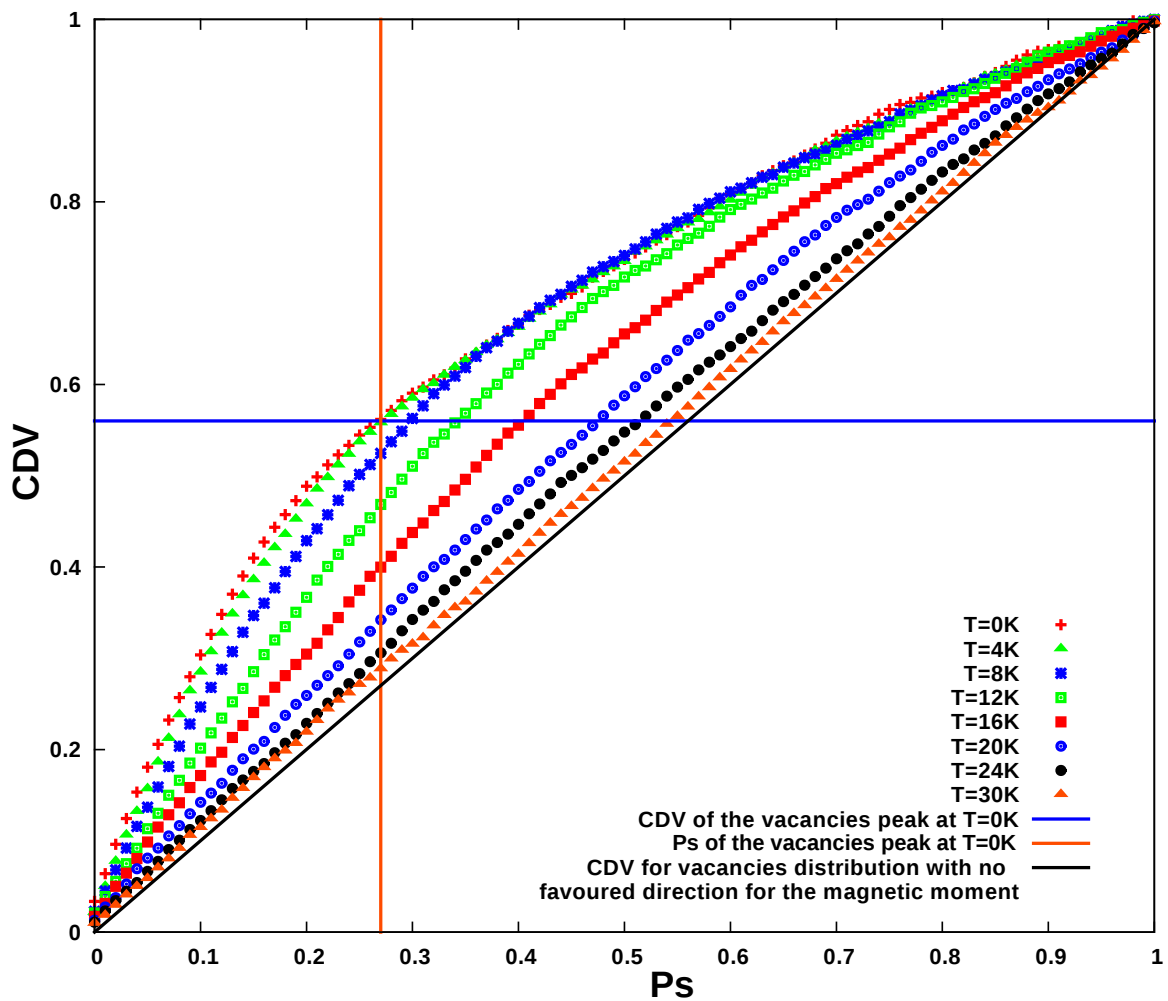


Figure 2.17: The cumulative density of surface vacancies (CDV) of the ensembles K5 as a function of P_s (the percentage of the surface spins allocated around the magnetic equator) at different temperatures.

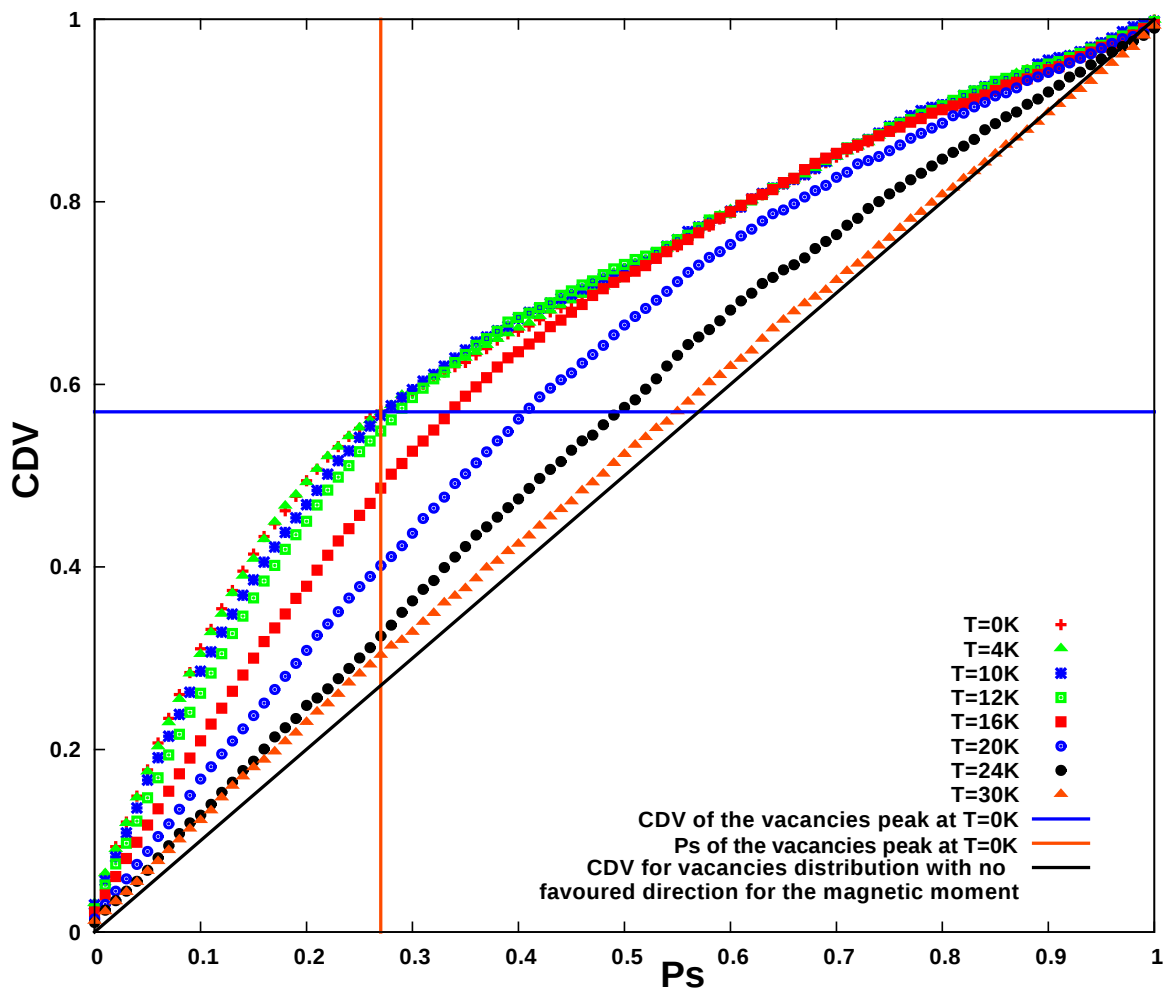


Figure 2.18: The cumulative density of surface vacancies (CDV) of the ensembles K10 as a function of P_s (the percentage of the surface spins allocated around the magnetic equator) at different temperatures.

section we study the effects of surface thickness.

Figs. 2.19 and 2.20 show the polar distribution of the surface vacancies of the ensembles Dc63 and Dc675 respectively as a function of $\cos(\varphi)$. The two ensembles were cooled under zero external field with cooling rate of $1 \text{ K}/t_u$. The ensemble Dc63 consists of 1000 non-interacting nanospheres each one is of $D = 7.5 \text{ nm}$, $D_c = 6.3 \text{ nm}$ and $K_s = 10 \text{ K}$. The ensemble Dc675 is identical to the ensemble Dc63 except that the core diameter is $D_c = 6.3 \text{ nm}$ for Dc63 while it is $D_c = 6.75 \text{ nm}$ for Dc675.

Comparing Figs. 2.19 and 2.20 shows that the peak in the surface vacancy distribution at the equator is wider in the ensemble with the thin surface (Dc675) than in the ensemble with the thick surface (Dc63). This reflects the fact that the nanospheres with the thinner surface (and hence lower pinning energy) are able to sample a wider region of phase space than the nanosphere's with the thicker surface. This is also reflected in the observation that a recognizable peak in the surface vacancy distribution persists to $T \approx 30 \text{ K}$ for the Dc63 ensemble (thick surface) but is no longer present by $T \approx 24 \text{ K}$ for the Dc675 ensemble.

Figs. 2.22 and 2.21 show the cumulative density distribution of surface vacancies for the ensembles Dc675 and Dc63 respectively as a function of P_s at different temperatures. The surface thickness effect is clear at $T = 15 \text{ K}$. While the CDV is fairly different at $T = 15 \text{ K}$ from $T = 0 \text{ K}$ in the ensemble Dc63. This difference disappears for an area corresponding to an angle range bigger than $\cos(\varphi) = P_s = 0.33$.

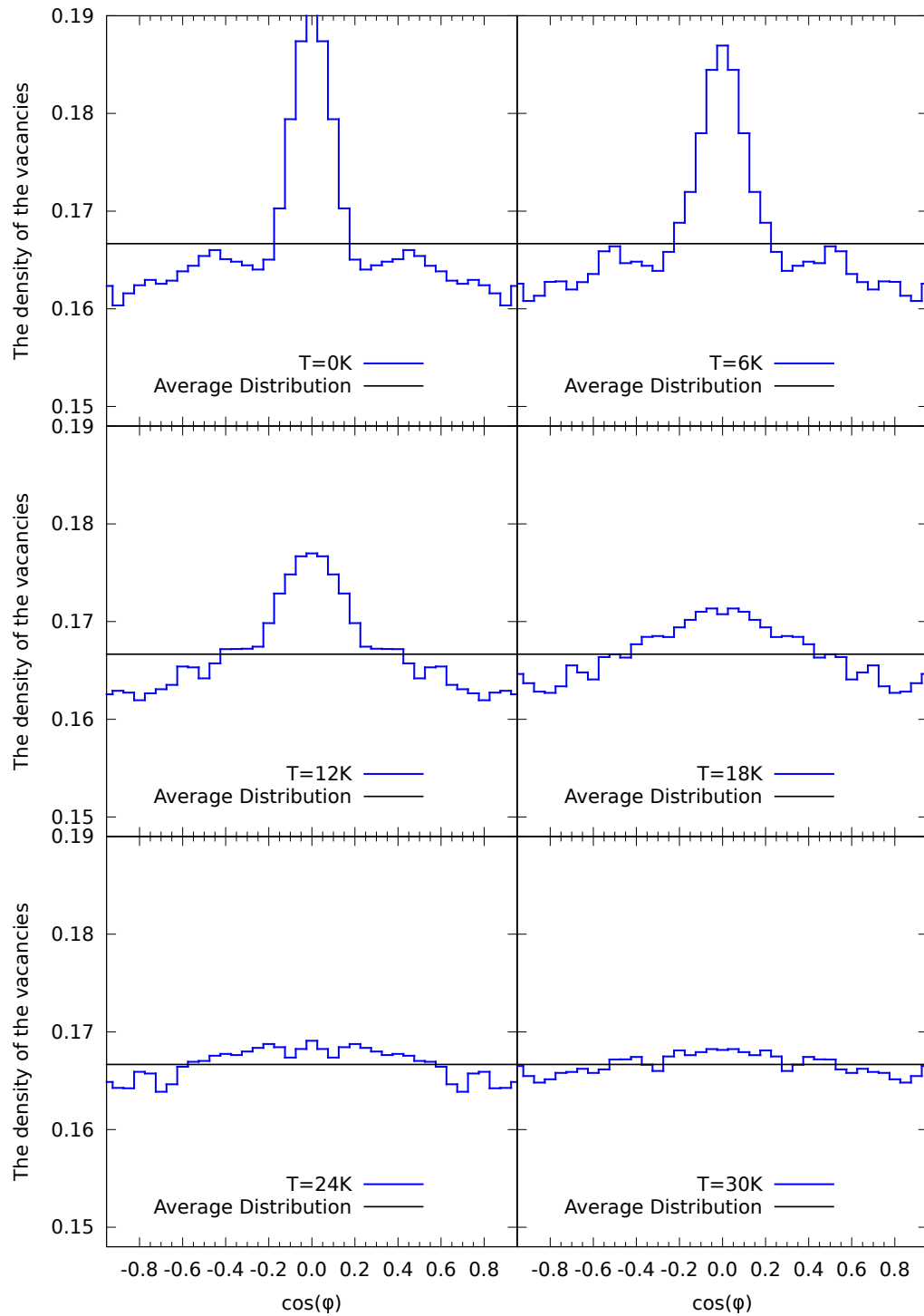


Figure 2.19: The polar distribution of surface vacancies for the ensemble Dc63 as a function of $\cos(\varphi)$ at different temperatures. The ensemble has been cooled with rate of $1 \text{ K}/t_u$ under zero external field.

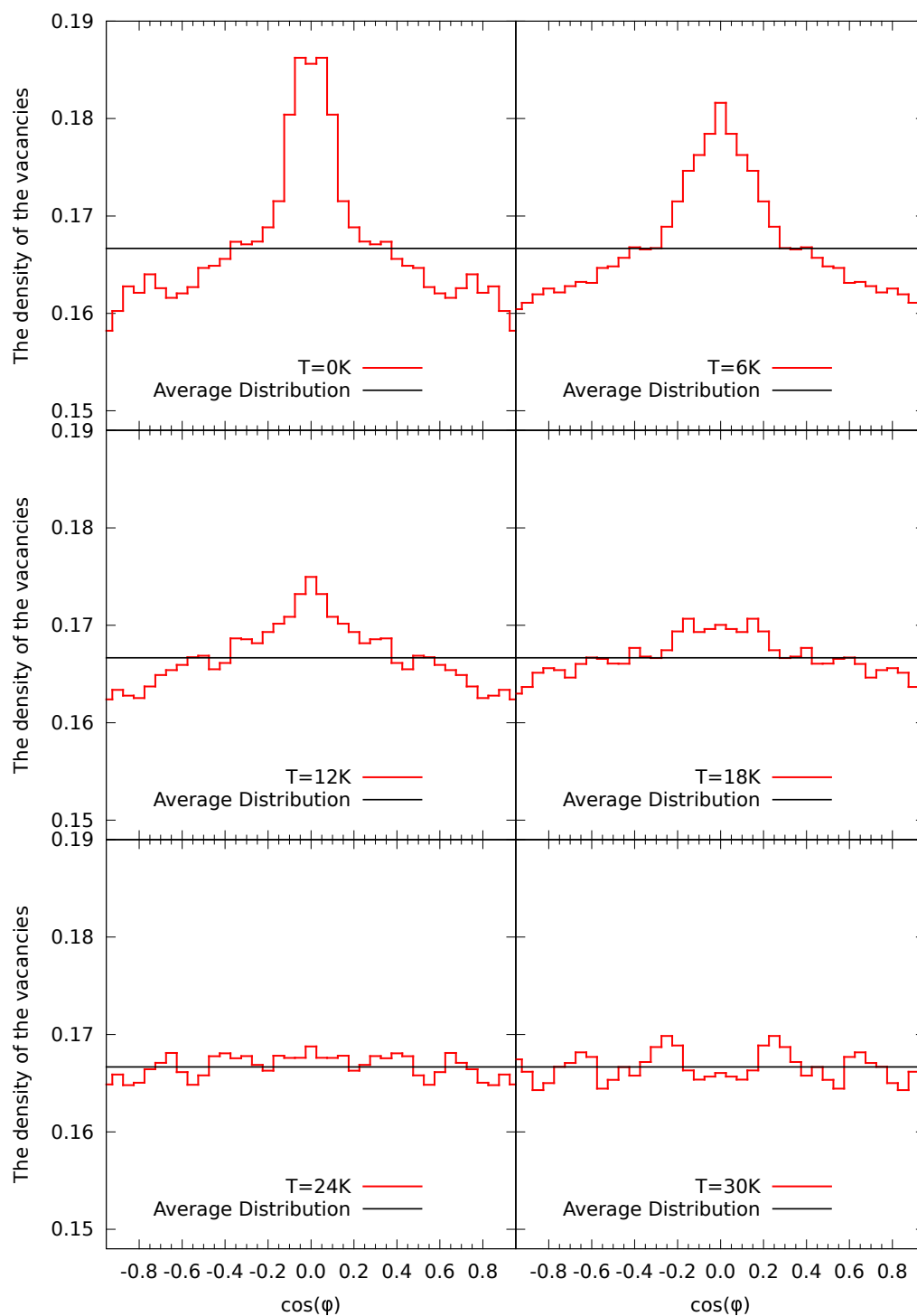


Figure 2.20: The polar distribution of surface vacancies for the ensemble Dc675 as a function of $\cos(\varphi)$ at different temperatures. The ensemble has been cooled with rate of $1 \text{ K}/t_u$ under zero external field.

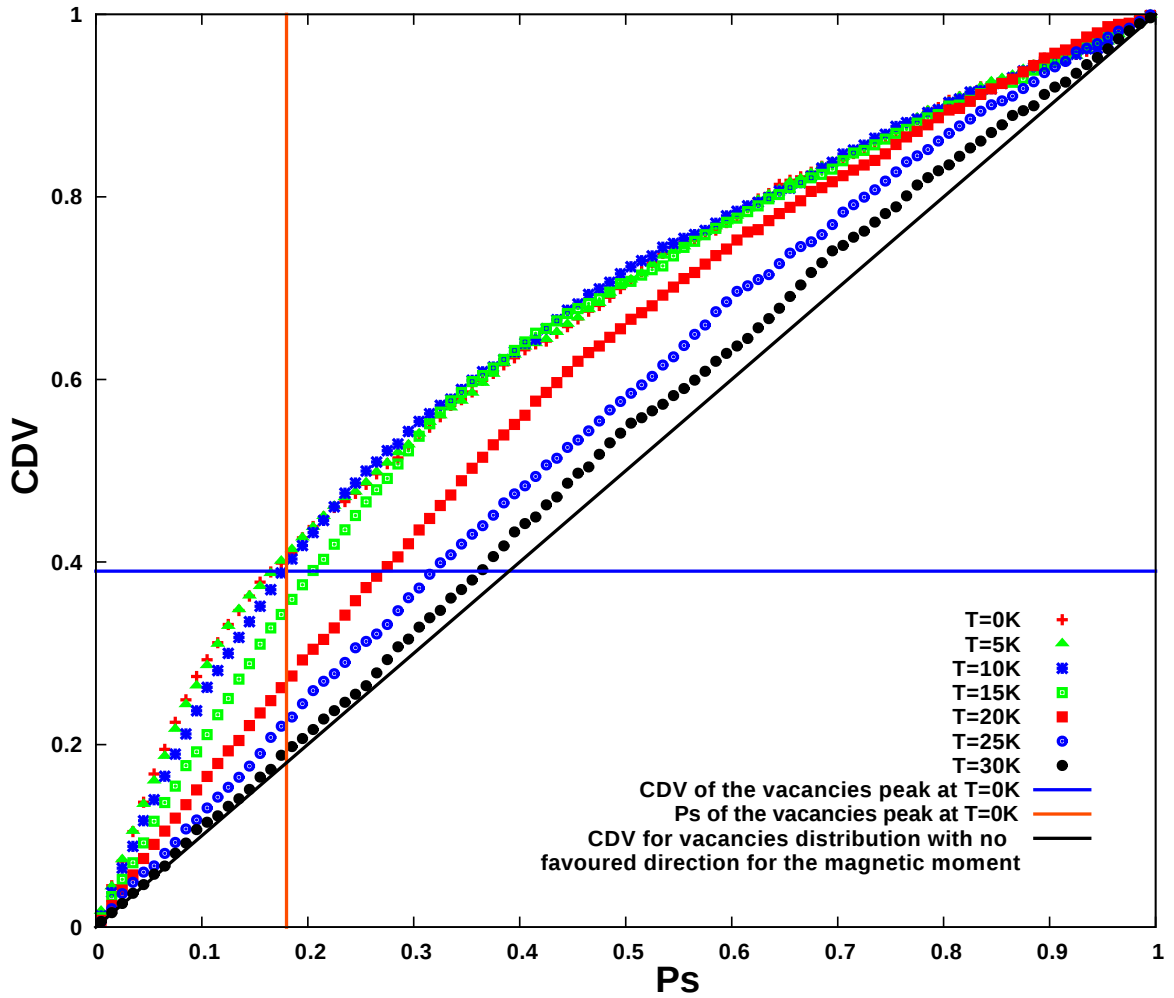


Figure 2.21: The cumulative density of surface vacancies (CDV) of the ensembles Dc63 as a function of P_s (the percentage of the surface spins allocated around the magnetic equator) at different temperatures.

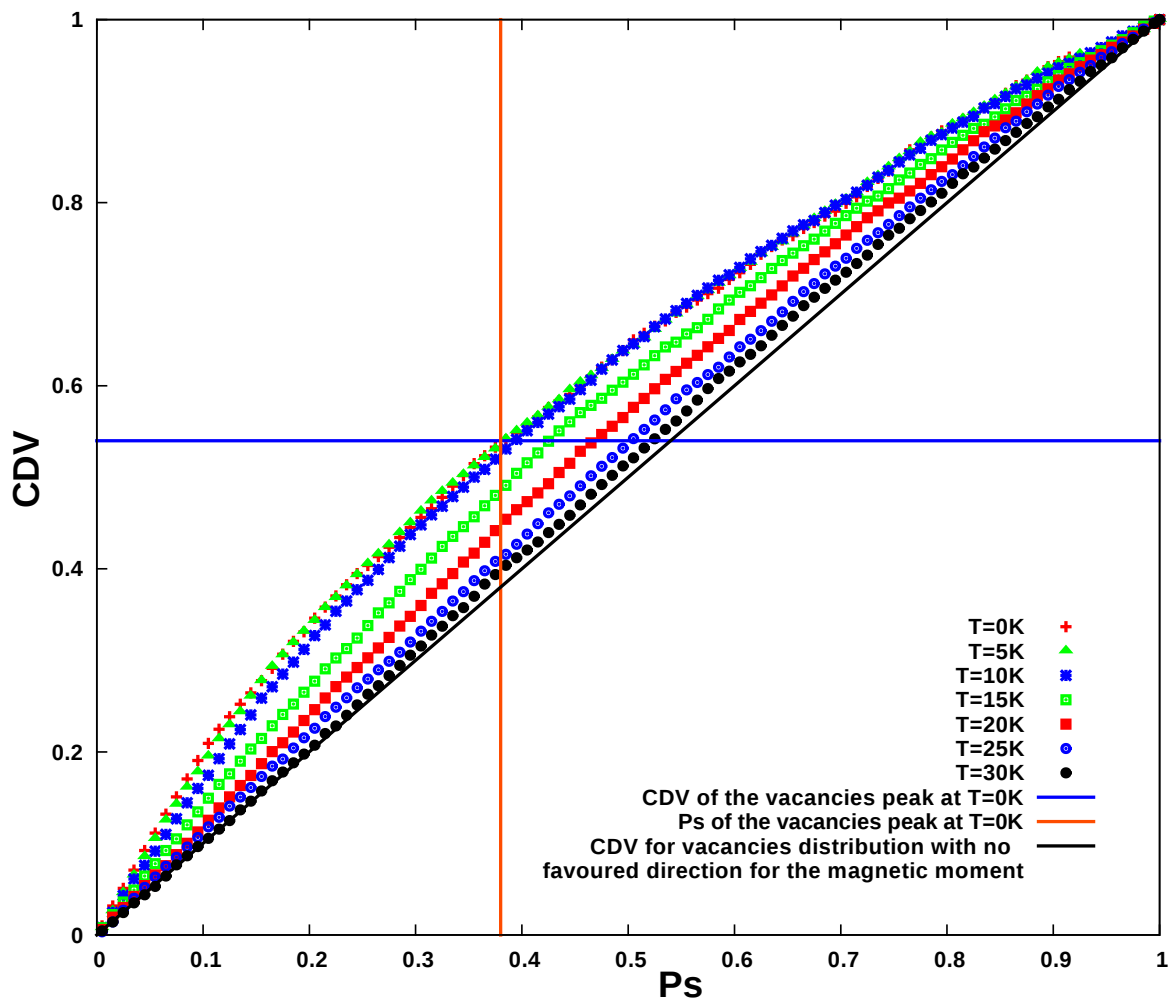


Figure 2.22: The cumulative density of surface vacancies (CDV) of the ensembles Dc675 as a function of P_s (the percentage of the surface spins allocated around the magnetic equator) at different temperatures.

2.6 Summary

We have presented results from a series of stochastic LLG simulations implemented by MagLua [44, 45] for noninteracting maghemite nanospheres. For comparison, ensembles with different nanosphere diameters, surface anisotropies, and the surface thicknesses were studied. The simulation model has a bulk-like core, a radial surface anisotropy, and a weak exchange between the surface spins. The results show two distinct ordering temperatures, T_c and T_s . $T_c \simeq 850$ K is due to the ordering of the core spins and hence is close to the bulk maghemite ordering temperature, whereas $T_s \simeq 30$ K is due to the ordering of the surface spins. These temperatures are in good agreement with previous MC simulations as shown in the Appendix. A. Appendix B presents a comparison between experimental results with our simulations and shows a reasonable agreement between them.

Using the zero-field cooling procedure, we obtain a blocking temperature T_b that is comparable to the experimental value. Since the computation limitations allow only simulations of nanospheres under large external field with large cooling and heating rates, it remains a challenging task to compare the blocking temperature obtained by simulation to the one obtained experimentally. However, the simulations show high correlation between the blocking temperature and the surface anisotropy, whereas a weak dependency between the measured blocking temperature and the cooling and heating rates is observed.

In the range between T_c and T_s , the surface spins are randomly oriented and the core spins are aligned along each other. Below T_s , the core spins are highly aligned whereas the surface spins show a hedgehog-like texture, which results in a

domain wall at the magnetic equator at the surface. The spins at the domain wall are highly frustrated due to the competition between the radial surface anisotropy and the exchange with the highly ordered core spins. The width of the frustrated spins area, which is correlated to the domain wall, increases with increasing temperature and decreases with increasing the surface anisotropy, as shown in Fig. 2.13.

The vacancies in the B-sites are randomly distributed and therefore there is a higher vacancy density at some areas than others. The difference in the surface vacancy density from one area to another combined with the difference in energy between the spins at the domain wall and the rest of the surface spins results in an energy dependency on the direction of the magnetic moment of the nanosphere. This dependency can be interpreted as a magnetic torque that pins the high energy region (the magnetic equator at the surface) to one of the areas with high vacancy density at the surface. The results show that the pinning effect increases by increasing the surface anisotropy or the surface thickness.

Chapter 3

Nanoparticles Superstructures and Inter-Nanoparticle Interactions

For the case of MNP arrays in which the nanoparticles are coated with a non-magnetic material, the exchange interaction between the MNPs is negligible. The collective properties of an MNP array is therefore dominated by the dipole interaction. The magnetic properties therefore depend on the magnetic moment of the MNPs, the spacing between them and the spacial arrangement of the array.

In this section we study the phase behaviour of point dipoles of an FCC lattice using finite temperature LLG. The purpose of this work is to demonstrate that the code we are using reproduces the previously determined ferromagnetic ground state [50] and Curie temperature [51]. The results are also applied to develop a simple point dipole model of magnetic nanospheres that will be compared with a more detailed model that includes the effect of the internal spin configuration of the individual nanospheres (Ch. 4).

3.1 The ground state of dipolar lattices in two and three dimensions

The magnetic field interaction between two point dipoles \vec{m}_i and \vec{m}_j separated by a displacement vector \vec{R} may be written in SI units as

$$\begin{aligned} E_{ij} &= -\vec{m}_i \cdot \vec{B}_{ij} \\ &= -\frac{\mu_0}{4\pi} \left(\frac{\vec{m}_i \cdot \vec{m}_j}{R_{ij}^3} - 3 \frac{(\vec{m}_i \cdot \vec{R}_{ij})(\vec{R}_{ij} \cdot \vec{m}_j)}{R_{ij}^5} \right). \end{aligned} \quad (3.1)$$

From this, we obtain the expression for the energy of an array of dipoles:

$$E = -\frac{\mu_0}{4\pi} \sum'_{\langle ij \rangle} \left(\frac{\vec{m}_i \cdot \vec{m}_j}{R_{ij}^3} - 3 \frac{(\vec{m}_i \cdot \vec{R}_{ij}) \cdot (\vec{m}_j \cdot \vec{R}_{ij})}{R_{ij}^5} \right), \quad (3.2)$$

where $\sum'_{\langle ij \rangle}$ denotes the sum of all pairs $\{i, j\}$ for $i \neq j$ (Note: this may be written as $1/2 \sum_{i \neq j}$ where the factor of 1/2 is included to avoid double counting). Equation 3.2 can be rewritten in terms of the dimensionless variables $\hat{\sigma} = \vec{m}/|\vec{m}|$ and $\vec{r}_{ij} = \vec{R}_{ij}/D$ as

$$E = -g \sum'_{\langle ij \rangle} \left(\frac{\hat{\sigma}_i \cdot \hat{\sigma}_j}{r_{ij}^3} - 3 \frac{(\hat{\sigma}_i \cdot \vec{r}_{ij}) \cdot (\hat{\sigma}_j \cdot \vec{r}_{ij})}{r_{ij}^5} \right), \quad (3.3)$$

where D is the distance between the nearest neighbors and $g = -\mu_0 m^2 / 4\pi D^3$ is the normalizing factor. In this section the energy and temperature are rescaled by setting $g = 1$.

From Eq. 3.2 we see that the dipole interaction is anisotropic and hence the structure in which the dipoles are arranged control the nature of the dipole energy. For example, 1D array of dipoles minimizes the energy by ordering the dipoles parallel

to the array, a square lattice of magnetic dipoles shows antiferromagnetic order [46], a triangular lattice shows ferromagnetic order in the lattice plane [52], while the FCC lattice orders ferromagnetically [51].

The long range nature of the dipole interaction considerably complicates the evaluation of the energy of a spin configuration. While in two dimensions the dipole energy for ferromagnetic states converge in the limit $L \rightarrow \infty$, where L denotes the lateral dimensions of the lattice, the convergence is very slow and highly dependent on the boundary conditions. Typically periodic boundary conditions are applied that require the spin configurations to satisfy,

$$\begin{aligned}\vec{M}_i &= \vec{M}(\vec{r}_i), \\ &= \vec{M}(\vec{r}_i + L\Delta\vec{R}),\end{aligned}\tag{3.4}$$

where $\Delta\vec{R}$ is a translation vector that leaves the vector lattice invariant and L is an integer. The dipole energy can be calculated for periodic systems using Ewald summation techniques [46].

In three dimensions the problem is even more complicated as the energy calculated in the limit $L \rightarrow \infty$ depends on the shape of the surface bounding the volume, giving rise to the so called demagnetizing field. The application of the periodic boundary conditions essentially ignores the effect of the boundary conditions. The situation is similar to the case of an exchange ferromagnet, in which the demagnetizing field is ignored in theoretical or numerical studies of the phase behaviour, but is nevertheless essential to the energetics of ferromagnetic domain formation in ferromagnetism.

3.2 Magnetic dipole interactions in FCC arrays

To investigate the effect of the dipole interaction on the FCC lattice, a series of stochastic LLG simulations have been performed for different lattice sizes. The interaction matrix used to describe the dipole interaction for the FCC array, assuming periodic boundary conditions, was based on the work described in [50] (and the references contained therein) and was implemented in MagLua by J. Mercer [44, 45]. The magnetic moment of the dipoles and the distance between the nearest neighbors dipoles were set to unity and the damping factor chosen as $\alpha = 0.5$.

The simulations were performed using boundary conditions that corresponds to $\Delta\vec{R} = \{(0, L, L), (L, 0, L), (L, L, 0)\}$. This means that the dipole $\vec{\sigma}(\vec{R})$ at the point \vec{R} is identical to the dipole $\vec{\sigma}(\vec{R} + \Delta\vec{R})$ at the point $\vec{R} + \Delta\vec{R}$. The simulations were performed for lattices with $L = 4, 8, 16$ and 32 . For each lattice size, 50 simulations were performed cooling from 1 to 0 in steps of 0.025 (in this chapter, temperature, energy, distance, time and all the other physical quantities are represented by dimensionless reduced units) with 2×10^6 stochastic LLG steps performed each temperature step with a time step of 10^{-3} time units. The first 10^6 LLG steps in each temperature step were ignored and the parameters of interest were calculated by averaging them over the second 10^6 LLG steps. These data were then averaged over the 50 systems. The calculation of the dipole field at each LLG step made the simulation of large lattices very time consuming. From these simulations, estimates of the magnitude of the net magnetic moment M , the heat capacity C_H , the susceptibility χ , and the Binder parameter (Eq. 3.7) were calculated as a function of temperature.

Fig. 3.1 shows the magnetization verses temperature for different lattice sizes.

The smaller lattices show a more pronounced size effect especially in the vicinity of the lattice ordering temperature (T_d) and above. Due to the size effect, it is difficult to accurately determine the critical temperature from the M-T curve. However, it is reasonable to conclude that $0.6 < T_d < 0.7$.

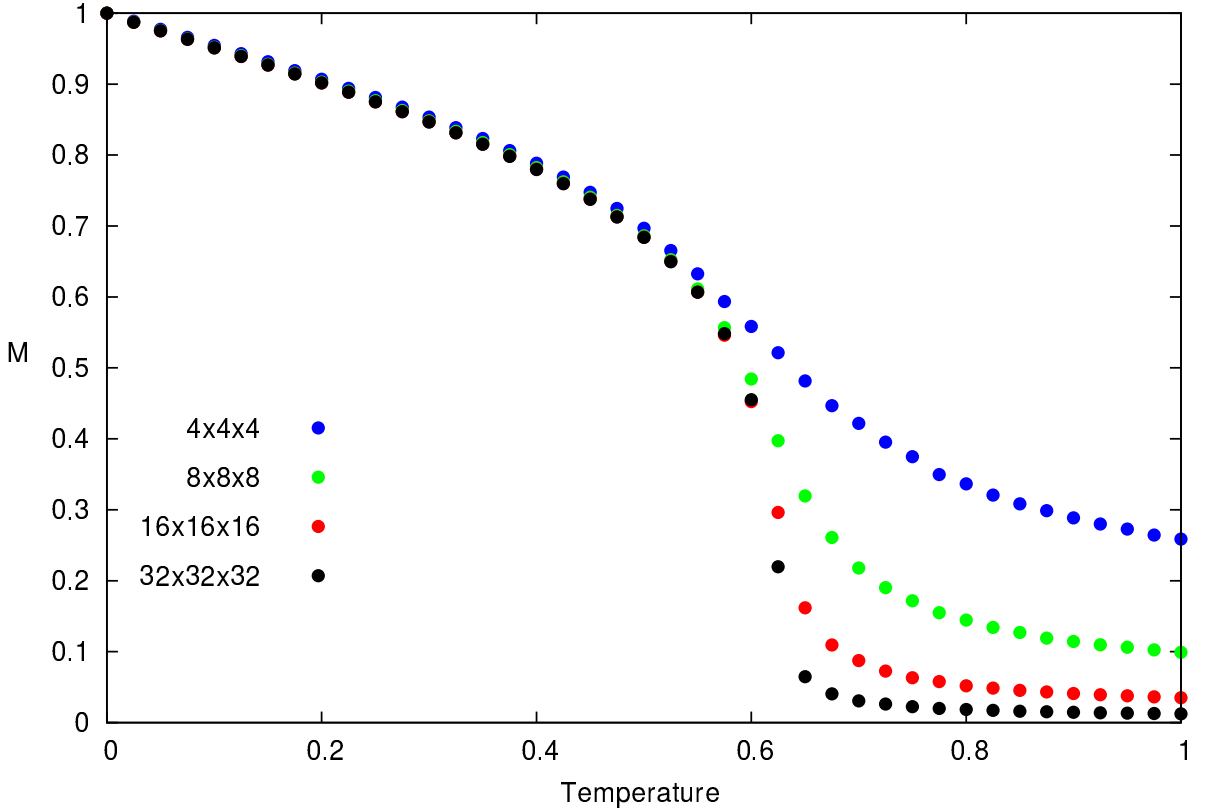


Figure 3.1: The magnetization of different sizes of the FCC lattice of magnetic dipoles as a function of temperature.

Fig. 3.2 shows the susceptibility as a function of temperature for different lattice sizes. The susceptibility was calculated from the expression:

$$\chi = (\langle M^2 \rangle - \langle M \rangle^2)/T \quad (3.5)$$

The data for each value of L show a peak in the susceptibility. We note that the peaks get narrower with the maximum value increasing as L increases, indicative of a continuous transition at $T_d \approx 0.62$

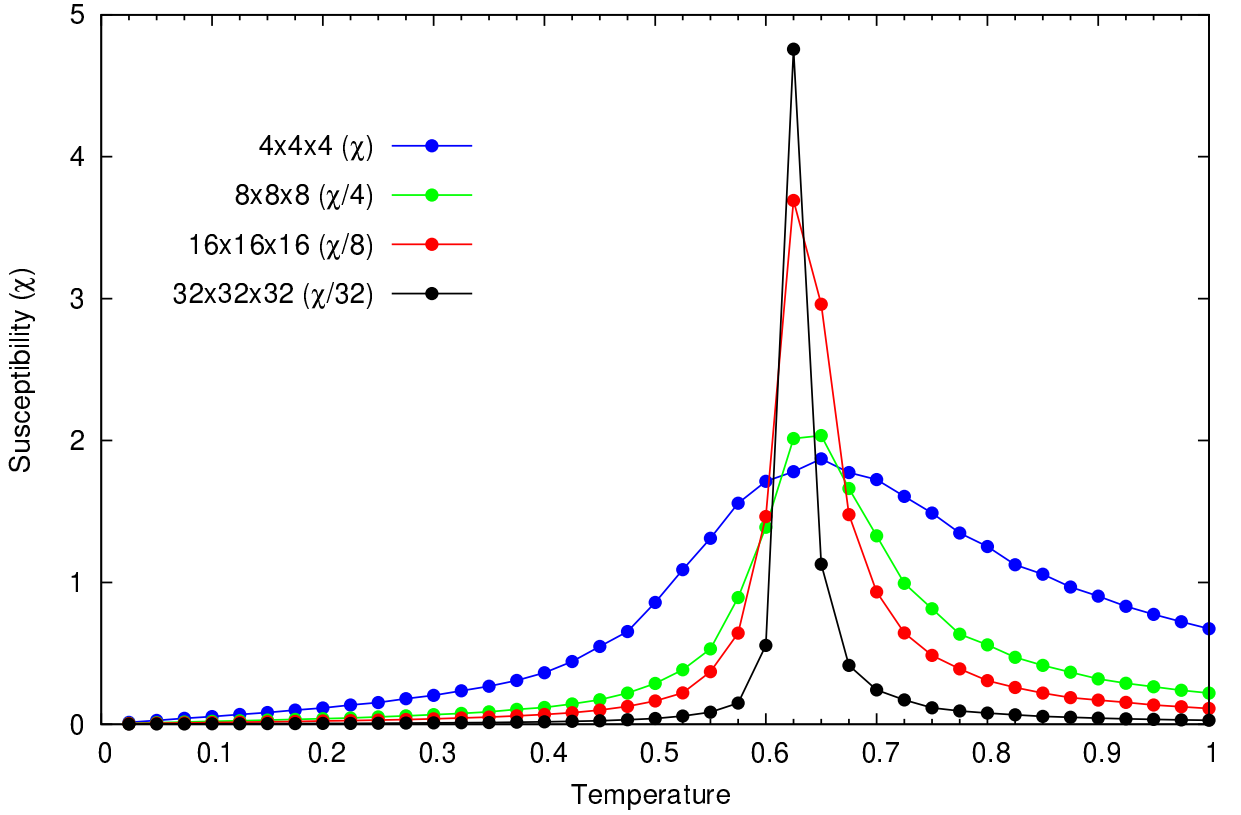


Figure 3.2: The susceptibility of different sizes of the FCC lattice of magnetic dipoles as a function of temperature (the susceptibility is divided by the number shown in the legend and the solid lines are drawn for the convenience of the eye).

Fig. 3.3 shows the heat capacity as a function of temperature for different lattice sizes. The heat capacity was calculated as:

$$C_H = (\langle E^2 \rangle - \langle E \rangle^2)/T^2 \quad (3.6)$$

The heat capacity data for each value of L all give $\lim_{T \rightarrow 0} C_H = 1$ with a peak at some temperature T_0 that increases with increasing L . The data also show the peak becoming narrower, higher and sharper as L increases, indicative of a continuous transition to ferromagnetic state at T_d , consistent with the susceptibility data.

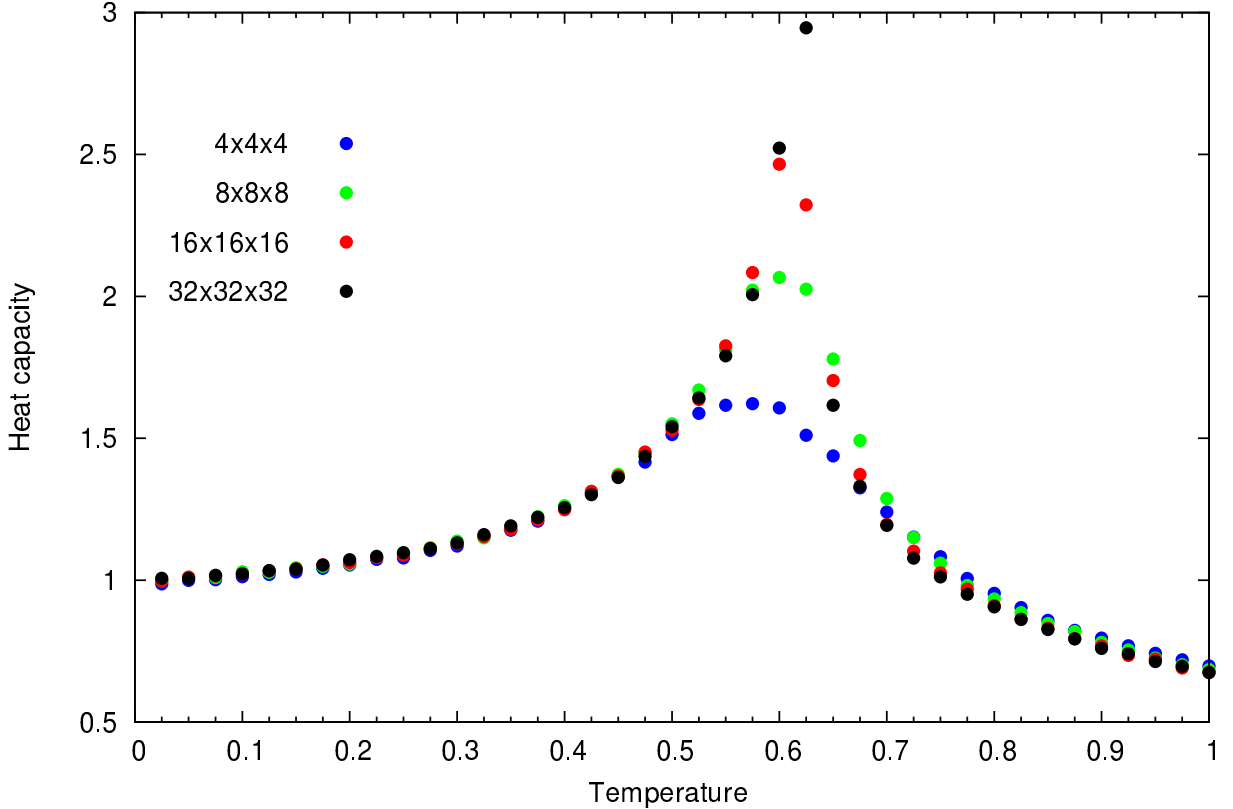


Figure 3.3: The heat capacity of different sizes of the FCC lattice of magnetic dipoles as a function of temperature.

Fig. 3.4 shows the energy per dipole as a function of temperature. Since the energies were practically size independent, even above the ordering temperature, only the data for for the $8 \times 8 \times 8$ lattice is shown. The ground state energy $E_0 = -2.956$ agrees with [53] and [50]. It was also found that while the ground state energy is

degenerate and there is no favoured direction, our simulation data for 200 dipole arrays with different L values and at different temperatures appeared to show that entropic forces favoured a magnetization vector oriented along the $[1\ 1\ 1]$ direction. We observed no evidence of the temperature dependent reorientation transition at around $T_d/2$ referred to in previous studies [51]. This is consistent with more recent simulation results [54]. The data in Fig. 3.4 also show no obvious discontinuity in the slope, again this consistent with a continuous transition at T_d .

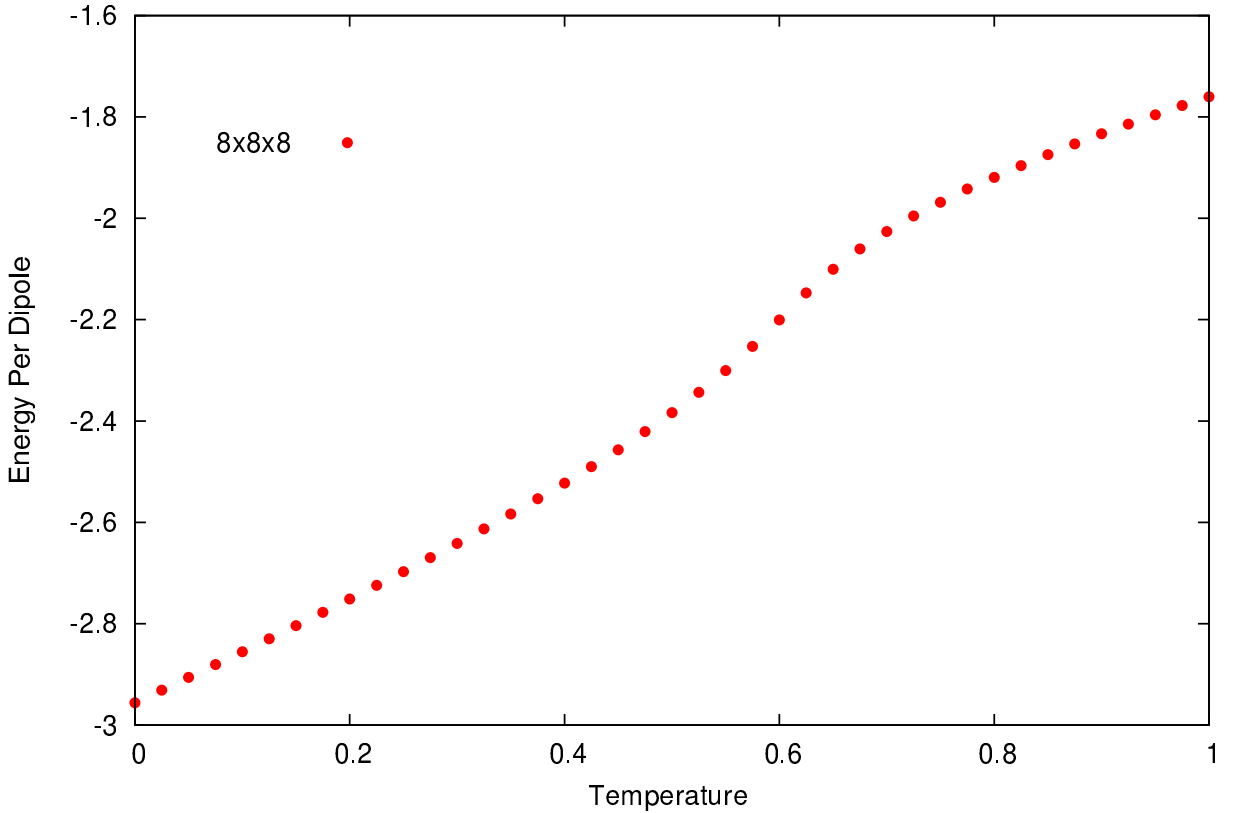


Figure 3.4: The dipole energy of different sizes of the FCC lattice of magnetic dipoles as a function of temperature.

While the magnetization, susceptibility, heat capacity and energy calculated from

the simulation data are consistent with a continuous phase transition at $T_d \approx 0.62$ finite size effects make it difficult to obtain a more accurate estimate of T_c that we can reliably compare with previous work [51]. A more accurate approach is to compute the Binder parameter [52, 55] given by:

$$b = \langle M^2 \rangle^2 / \langle M \rangle^4 . \quad (3.7)$$

The Binder parameter is useful in calculating the value of T_d from finite size data as it has the same value at the critical temperature regardless of the lattice size. Fig. 3.5 shows binder parameter as a function of temperature for different sizes of the FCC lattice. The data show that the plots of b for different L values cross over near the ordering temperature $T_d = 0.625 \pm 0.01$. This is consistent with previous MC simulations by Bouchard [51] who gives the result $\rho m^2 / k_B T_d = 2.316 \pm 0.015$, where ρ is the number of dipoles per unit volume and m is the magnitude of the magnetic moment of the dipoles. To compare with the results obtained from Fig. 3.5 we set $\mu = 1$, $k_B = 1$ and the nearest neighbour spacing to unity to give $\rho = 4 \times 2^{3/2}$ and hence $T_d = 0.611$, which is in good agreement with the result obtained from our simulations. This result is also in agreement with other more recent calculations [54]

3.3 Summary

We have presented results from a series of stochastic LLG simulations for the FCC dipole lattice with periodic boundary conditions. The results show a strong size dependency of the magnetization at temperatures in the vicinity of T_d and above. A more precise estimation of T_d using Binder parameter shows an ordering temperature

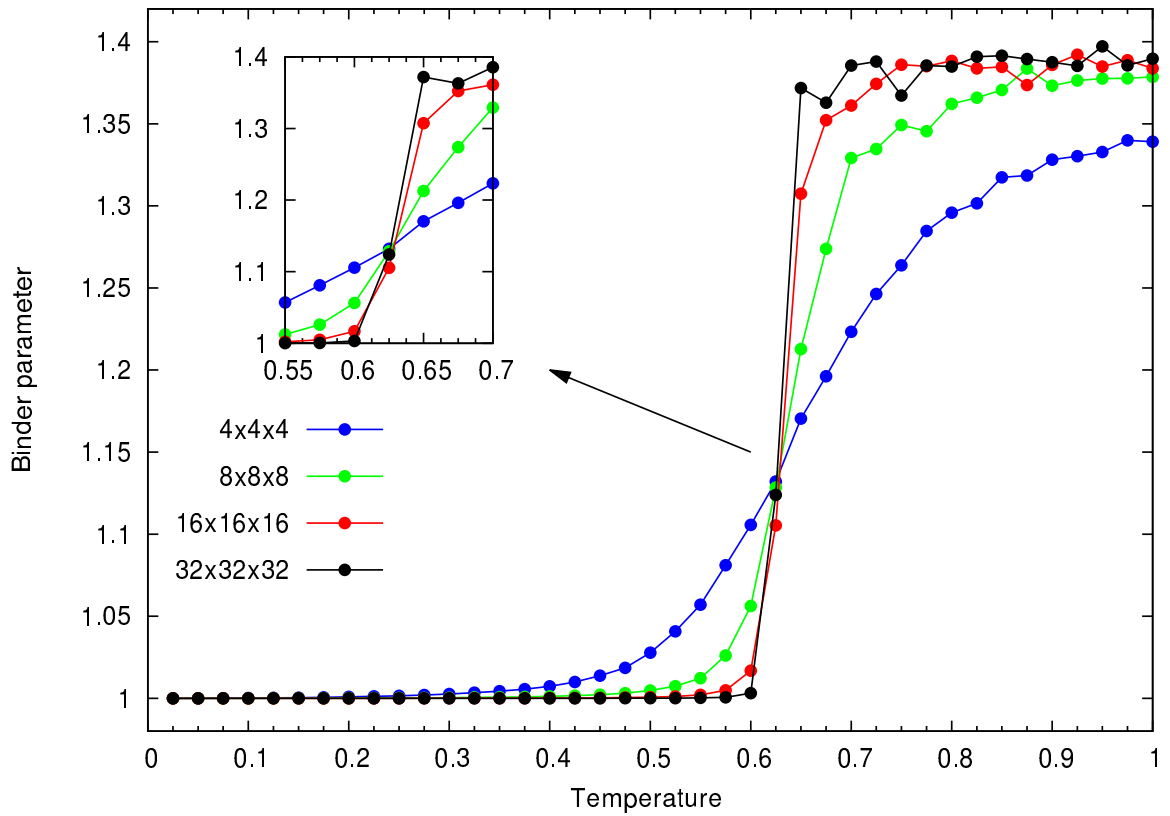


Figure 3.5: Binder cumulant for different sizes of the FCC lattice of magnetic dipoles as a function of temperature (lines are just for guidance).

$T_d = 0.625 \pm 0.01$ that agrees with previous MC calculations [51]. Results for the specific heat and the susceptibility for several L values were also presented as functions of temperature. These curves showed a series of peaks consistent with the ordering temperature estimated from Binder parameter that seemed to be consistent with a second phase transition. Energy calculations show a degenerate ground state with a normalised energy of $E/g = -2.956$ for any direction of the magnetization with ferromagnetic configuration. This ground state energy value agrees with the work in [50]. At any finite temperature the net magnetization prefers the $[1\ 1\ 1]$ direction or any of its equivalent and there is no observed second transition that changes the preferred direction on the contrary of what has been suggested in the literature[51]. Finally, the consistency of the results shows that stochastic LLG can reliably simulate the equilibrium properties of the FCC dipole lattice.

Chapter 4

Nanosphere FCC Array

In this chapter, we study FCC arrays of maghemite nanospheres including both the dipole interactions between the nanospheres and the complex internal spin structure of these nanospheres, using stochastic LLG simulations. It is well established experimentally that interparticle dipole interactions in assemblies of magnetic nanoparticles can give rise to an enhanced collective behavior [56, 57, 58, 15]. This behavior can be exploited in various applications. Previous computational studies of these assemblies have been done assuming that each nanoparticle is a single magnetic dipole with a uniaxial anisotropy [41, 59, 42, 60], cubic anisotropy [43, 60], or using the Meiklejohn-Bean model where each nanosphere is represented as two anisotropic dipoles with an exchange between them, one dipole corresponding to the core while the other corresponding to the surface[61, 59]. However, here we present studies of FCC arrays that treat the internal spin structure of the nanospheres.

4.1 Model and parameters of the nanosphere FCC lattices

In addition to the quantities defined by Eqs. 2.7-2.10 for the non-interacting nanospheres, we define the following quantities: The average magnitude of the magnetic moment of the nanospheres (M_a) is given by

$$M_a = 1/N \sum_{n=1}^N \left| \sum_{i=1}^{q_n} \vec{S}_i(n) \right| \quad (4.1)$$

(Note: M_a is equivalent to M_n as in Eq. 2.7 but without normalization. Hence, M_a defines the magnetic moment of the individual nanospheres regardless of their collective order in the lattice.). The normalized average magnetic moment of the nanosphere lattice (M_{nl}) is given by

$$M_{nl} = 4/N \left| \sum_{n=1}^N \sum_{i=1}^{q_n} \vec{S}_{i(n)}/q_n \right| \quad (4.2)$$

(Note: M_{nl} is the equivalent to the magnitude of the magnetic moment, \vec{M}_e , of the ensemble as in Eq. 2.8.). The order parameter of the nanosphere lattice is given by

$$O_{nl} = M_{nl}/M_n. \quad (4.3)$$

The normalized average magnetic moment of the dipole lattice (M_{dl}) is given by

$$M_{dl} = 1/(NM_a(0)) \left| \sum_{n=1}^N \vec{M}_{d(n)} \right| \quad (4.4)$$

(Hence: $M_{dl} = M_{nl}$ if the magnetic moment of every nanosphere has the same direction of its equivalent dipole.). Finally, the order parameter of the dipole lattice (O_{dl}) is given by

$$O_{dl} = M_{dl}/M_n, \quad (4.5)$$

where N is the number of the nanospheres or the dipoles in the ensemble (array), q_n is the number of spins in the nanosphere number (n), N_{sl} is the number of the spins in the whole array, $M_{d(n)}$ is the magnetic moment of the dipole n (without normalization), and $M_a(0)$ is the average magnitude of the magnetic moment of the nanospheres at $T = 0$ K (not normalized to one).

The energy of an FCC array of magnetic nanospheres may be written as

$$\begin{aligned}
E = & - \sum_{k=1}^N \sum_{\{i,j\} \in k} J_{ki,kj} \hat{\sigma}_{ki} \cdot \hat{\sigma}_{kj} - \sum_{k=1}^N \sum_{i \in k} K_{ki} (\hat{\sigma}_{ki} \cdot \hat{n}_{ki})^2 \\
& - \frac{g}{2} \sum_{k=1}^N \sum_{l=1}^N \left(\sum_{i \in k} \sum_{j \in l} \hat{\sigma}_{ki} \cdot \mathbf{D}^{ik,jl} \cdot \hat{\sigma}_{lj} \right) - m \sum_{k=1}^N \sum_{i \in k} \vec{B} \cdot \hat{\sigma}_{ki}, \quad (4.6)
\end{aligned}$$

where the subscripts $\{ki\}$ denote the i^{th} spin in the k^{th} nanosphere. While this expression is exact, the long-range character of the dipolar interaction means that the computational effort required to compute the effective field for a given spin configuration other than a few cells is not feasible. However, if we assume that the intra-nanosphere interaction is dominated by the exchange interaction while the inter-nanosphere interaction consists only of the dipolar interaction then we may simplify the dipolar interaction somewhat to give the effective Hamiltonian as

$$\begin{aligned}
E_{\text{eff}} = & - \sum_{k=1}^N \sum_{\{i,j\} \in k} J_{ki,kj} \hat{\sigma}_{ki} \cdot \hat{\sigma}_{kj} - \sum_{k=1}^N \sum_{i \in k} K_{ki} (\hat{\sigma}_{ki} \cdot \hat{n}_{ki})^2 \\
& - \frac{g}{2} \sum_{k=1}^N \sum_{l=1}^N \left(\sum_{i \in k} \hat{\sigma}_{ki} \right) \cdot \mathbf{D}^{kl} \cdot \left(\sum_{j \in l} \hat{\sigma}_{lj} \right) - m \sum_{k=1}^N \sum_{i \in k} \vec{B} \cdot \hat{\sigma}_{ki}, \quad (4.7)
\end{aligned}$$

where \mathbf{D}^{kl} is given by the interaction between two point dipoles. This simplification considerably reduces the computational effort required to calculate the effective fields while retaining the complexity of the spin structure of the individual nanospheres and the interaction between the dipolar fields generated by the magnetic moment of the

nanospheres where these fields are applied on the individual spins.

This model is used to study two FCC arrays of magnetite nanospheres using stochastic LLG. The lattice size used $8 \times 8 \times 8$ with periodic boundary conditions, with the long range part of the dipolar interaction treated using the Ewald summation [46].

Results are presented for two systems of nanospheres. Both systems consist of nanospheres of diameter $D = 7.5$ nm, $K_s = 10$ K and have the same exchange parameters as these studied in Ch. 2. The first set which we refer to as FDC675 has a core diameter of 6.75 nm and the second set, which we refer to as FDC63, has a core diameter $D_c = 6.3$ nm. Table 4.1 shows the ratio of the surface spins to the total number of spins (n_s/n_v), the lattice ordering temperature (T_l), the magnitude of the magnetic moment of the individual nanospheres at $T = 0$ K ($M_a(0)$), and $M_a(T_l)$ which is M_a at the lattice ordering temperature for FDC63 and FDC75. Also, the parameters of their equivalent dipole lattices, d63 and d675, respectively are presented in this table. The dipoles in the equivalent dipole arrays have the same magnetic moment of the corresponding nanospheres and have no anisotropy. To study the effect of the magnetostatic dipolar interactions on the intrinsic spin configuration of the nanospheres, FDC63 and FDC675 are compared with their equivalent systems of noninteracting nanospheres Dc63 and Dc675 (Table 2.2) respectively. The damping factor used in all the cases is 0.5.

Even using the simplified expression E_{eff} , the number of individual spins in the $8 \times 8 \times 8$ nanosphere arrays is sufficiently large ($\sim 5 \times 10^5$ spins per array), so that the computational times involved mean that it is not feasible to perform the calculation in serial mode. All of the simulations were performed in parallel using MPI with each

The FCC system	FDc63	d63	FDc675	d675
building unit	nanosphere	dipole	nanosphere	dipole
lattice size	$8 \times 8 \times 8$			
center to center distance	7.5 nm	7.5 nm	7.5 nm	7.5 nm
K_s (K)	10	0	10	0
D_c	6.3 nm	-	6.75 nm	-
n_s/n_v	0.406	-	0.276	-
T_l (K)	36.5	36.5	52	52
$M_a(0)(\mu_B)$	9275	9275	9830	9830
$M_a(T_l)(\mu_B)$	1400	1400	1850	1850

Table 4.1: Characteristic parameters of FDc63, FDc675 and the corresponding dipole lattices, d63 and d675.

nanosphere assigned to a single processor core. In addition, in order to reduce the effects of the latency between the processor cores and using the fact that the dipole field changes are very small in a single LLG time step, the dipole field is updated every 100 time steps ($2 \times 10^{-2} t_u$). Comparisons between results obtained by updating the dipole field each LLG time step shows little difference from those obtained in which the dipole field is updated every 100 LLG steps.

4.2 The equivalent dipole lattice

For comparison purposes, the results of the simulations of equivalent dipole lattices (Table 4.1) are also presented. The equivalent dipole lattice consists of a FCC lattice

of point dipoles with the same lattice spacing as the nanosphere lattice and a temperature dependent moment equal to that average moment of the nanospheres that make up the nanosphere lattice.

The dipole system is left to relax for $400 t_u$ at each temperature step using a time step of $1 \times 10^{-4} t_u$ and data collected over the final $200 t_u$ for each temperature. The net magnetization of the dipole lattices (M_{dl}) is obtained by averaging over 20 dipole arrays. The dipole arrays simulations were done using both Euler and RK4 integration schemes in which the precession of the magnetic dipoles is treated using quaternion formalism [44, 45]. The results of the simulations using the two integration methods show little difference. The results are may also be obtained from the results of the previous section using a non-linear scaling of the reduced temperature in the case of the equivalent dipole lattice due to the temperature dependence of the moment of the nanosphere

$$T/T_r = \frac{g(T)}{k_B} = \mu_0(M_a(T))^2/4\pi D^3 k_B \quad (4.8)$$

where $M_a(T)$ is the magnetic moment of the nanosphere/dipole at temperature T , D is the diameter of the nanospheres (the same as the distance between the centers of the nearest neighbors) and T_r is the reduced temperature used in Ch. 3. Fig. 4.1 shows the relation between the temperature of the dipole lattices corresponding to the two nanosphere lattices and the reduced temperature. We note from Fig. 4.1 that the reduced ordering temperature $T_r = 0.625$ is equivalent to lattice ordering temperature ($T = 52$ K) for the dipole lattice d675 and to lattice ordering temperature ($T = 36.5$ K) for the dipole lattice d63.

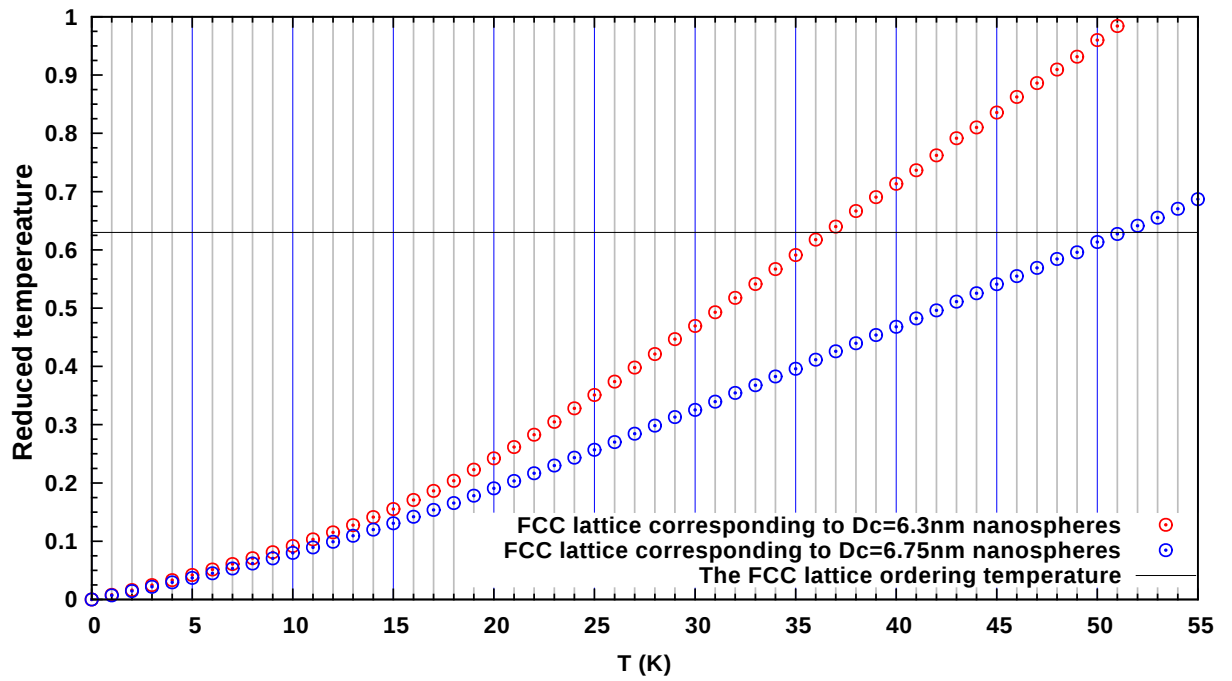


Figure 4.1: The relation between the reduced temperature and the temperature of two FCC dipole lattices d63 and d675 which correspond to the nanospheres with core diameter $D_c = 6.3 \text{ nm}$ and 6.75 nm , respectively (Table 4.1).

4.3 Results and Analysis

Simulations of an array of nanospheres with cores of 6.75 nm (FDc675) has been performed using RK4 integration (Appendix. C) with a time step of $2 \times 10^{-4} t_u$ with the dipole field being updated every 100 LLG steps. At each temperature, the stochastic LLG process was performed for $400 t_u$. Then the temperature was reduced and the lattice was left to equilibrate for another $400 t_u$. A similar procedure was applied to the FDc63, but with the somewhat longer equilibration time of $600 t_u$ at each temperature.

Fig. 4.2 shows the simulation process of the lattice FDc675. For example, the first (yellow) column represents the net lattice magnetization, M_{nl} , as a function of time at $T = 40$ K. The temperature is then reduced to 30 K and the net magnetisation plotted in the second (green) column and the system left to relax for another $400 t_u$ and so on. Similarly, Fig. 4.3 shows the simulation process for the FDc63 array.

Fig. 4.2 show a rapid increases in the lattice magnetisation M_{nl} of the FDc675 array when the temperature is reduced. We note similar jumps for the FDc63 array as shown in Fig. 4.3. These jumps happens because of the increase in the nanospheres magnetization M_n . Thus, reducing the temperature leads to the sudden increase in M_{nl} . For the data in the temperature range $T \leq 15$ K letting the lattice to equilibrate at the new temperature shows a reduction in M_{nl} following the initial increase. This reduction implies a loss of the orientational order between the nanospheres as the system relaxes. This reduction in the orientational order at low temperature is due to the pinning effect of the vacancies, as will be discussed later.

Fig. 4.4 shows the lattice magnetization, M_{nl} , of the FDc675 array plotted as a

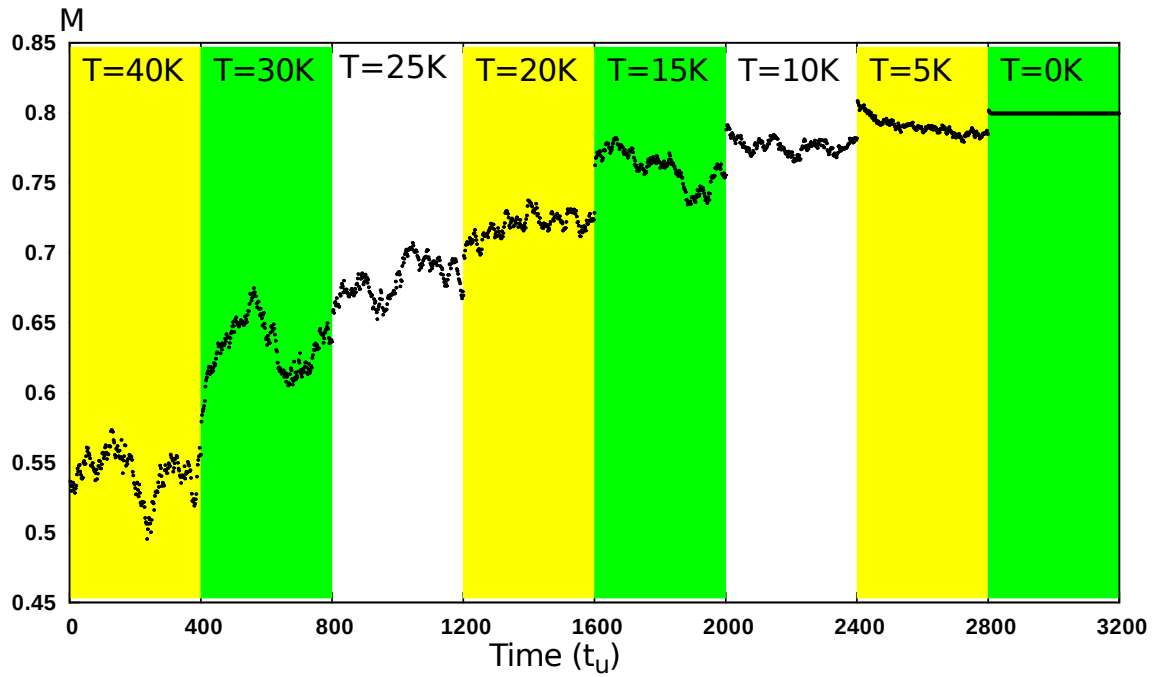


Figure 4.2: M_{nl} of an $8 \times 8 \times 8$ FCC nanosphere array as a function of temperature, where the nanospheres have a 7.5 nm diameter, 6.75 nm core diameter, 7.5 nm center to center spacing and $K_s = 10$ K (FDc675 Table 4.1).

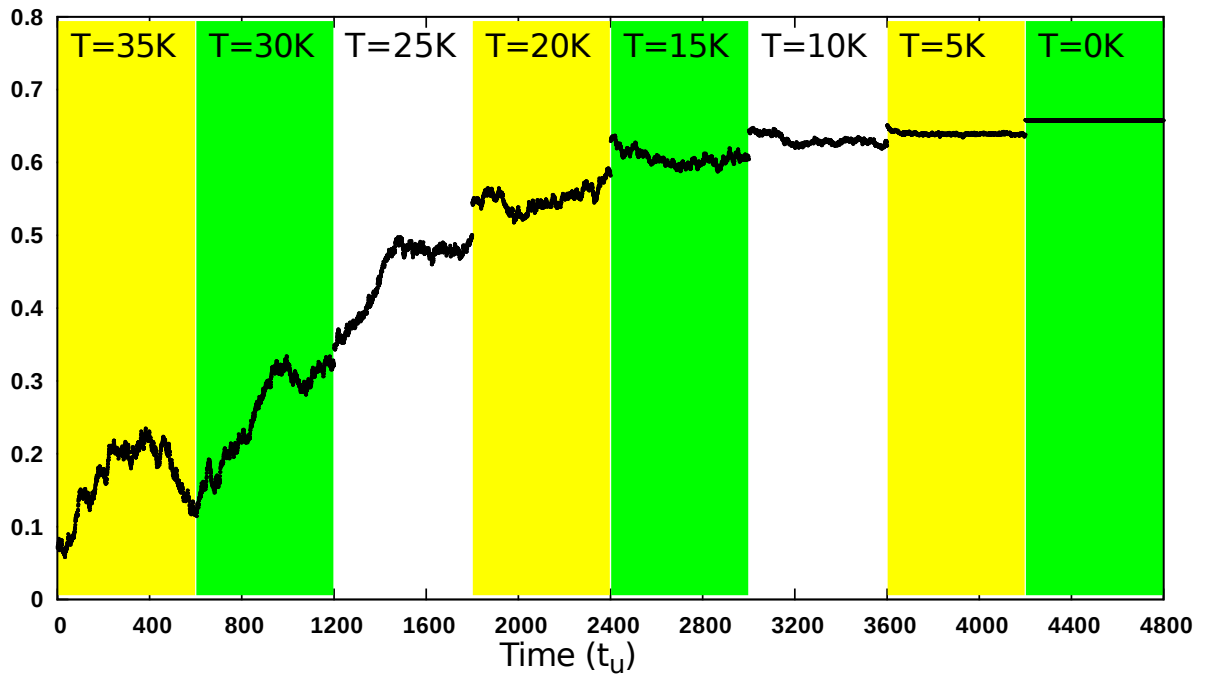


Figure 4.3: $M_{nl} a$ of an $8 \times 8 \times 8$ FCC nanosphere array as a function of temperature, where the nanospheres have a 7.5 nm diameter, 6.3 nm core diameter, 7.5 nm center to center spacing and $K_s = 10$ K (FDc63 Table 4.1).

function of temperature. The lattice magnetization, M_{dl} , of the equivalent dipole lattice, d675 is also plotted as a function of temperature together with M_n , the magnitude of the magnet moment of the maghemite nanospheres. M_n is scaled by unit of μ_B on the right y -axis while it is normalized on the left y -axis. A comparison with M_n of the system of noninteracting nanospheres Dc675 shows negligible difference when the dipole effect is introduced by placing the nanospheres on an FCC array. Fig. 4.5 shows the same data for the nanosphere lattice, FDc63 (Table 4.1), and the equivalent dipole lattice d63.

In Fig. 4.4, we distinguish two cases. At high temperatures ($T \gtrsim 30$ K), the nanosphere lattice have essentially the same magnetization as the equivalent dipole lattice. This is expected since the nanospheres behave as super-paramagnets. At low temperatures, M_{nl} drops below the magnetization of the equivalent dipole lattice (M_{dl}). This indicates that there is some phenomenon that decreases the orientational order between the nanospheres. The disordering at low temperatures is more obvious if we eliminate the effect of the temperature dependency of the magnitude of the magnetic moment of the nanospheres by defining the order parameter $O_{nl} = \langle \cos(\theta) \rangle$, where θ is the angle between the magnetic moment of the nanosphere and the net magnetization of the lattice. Hence, $O_{nl} = M_{nl}/M_n$.

The reduction in O_{nl} can be understood in light of the pinning effect which is a result of the inhomogeneity of the surface vacancies as discussed in Ch. 2. Fig. 4.6 shows the density of the vacancies of the lattice, FDc675, and the corresponding ensemble of non-interacting nanospheres, Dc675, as a function of $\cos(\varphi)$ at different temperatures. Both systems show a strong peak in the vacancies density at the equator where the peak gets lower with increasing the temperature. The peaks in the

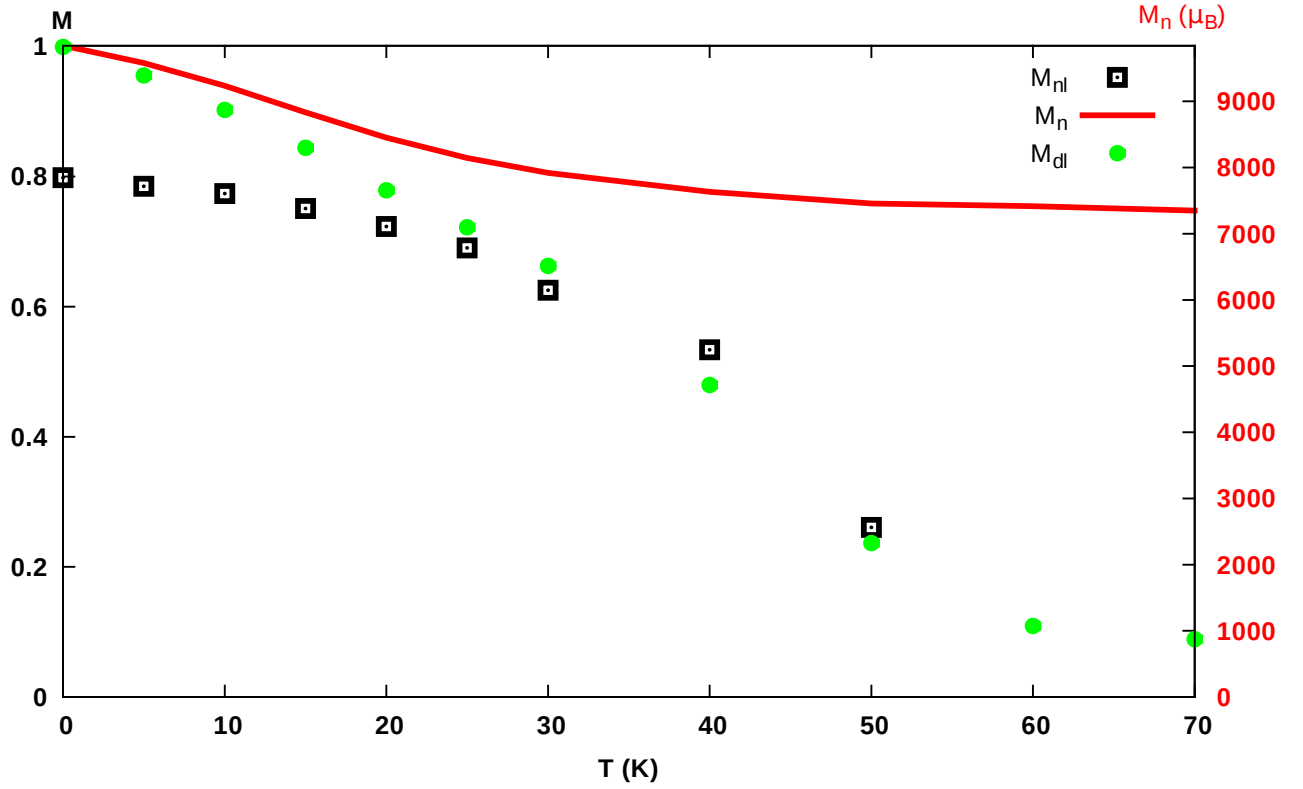


Figure 4.4: The lattice magnetization, M_{nl} , and the magnitude of the nanosphere magnetic moment, M_n , as a function of temperature. M_{nl} and M_n belong to the array FDc675 (Table 4.1). The array is an $8 \times 8 \times 8$ FCC lattice with 7.5 nm diameter nanospheres, 6.75 nm core diameter, $K_s = 10$ K and 7.5 nm center to center distance between the nearest neighbors. Also, M_{dl} , the magnetization of the corresponding dipole lattice (d675 Table 4.1) is presented as a function of temperature.

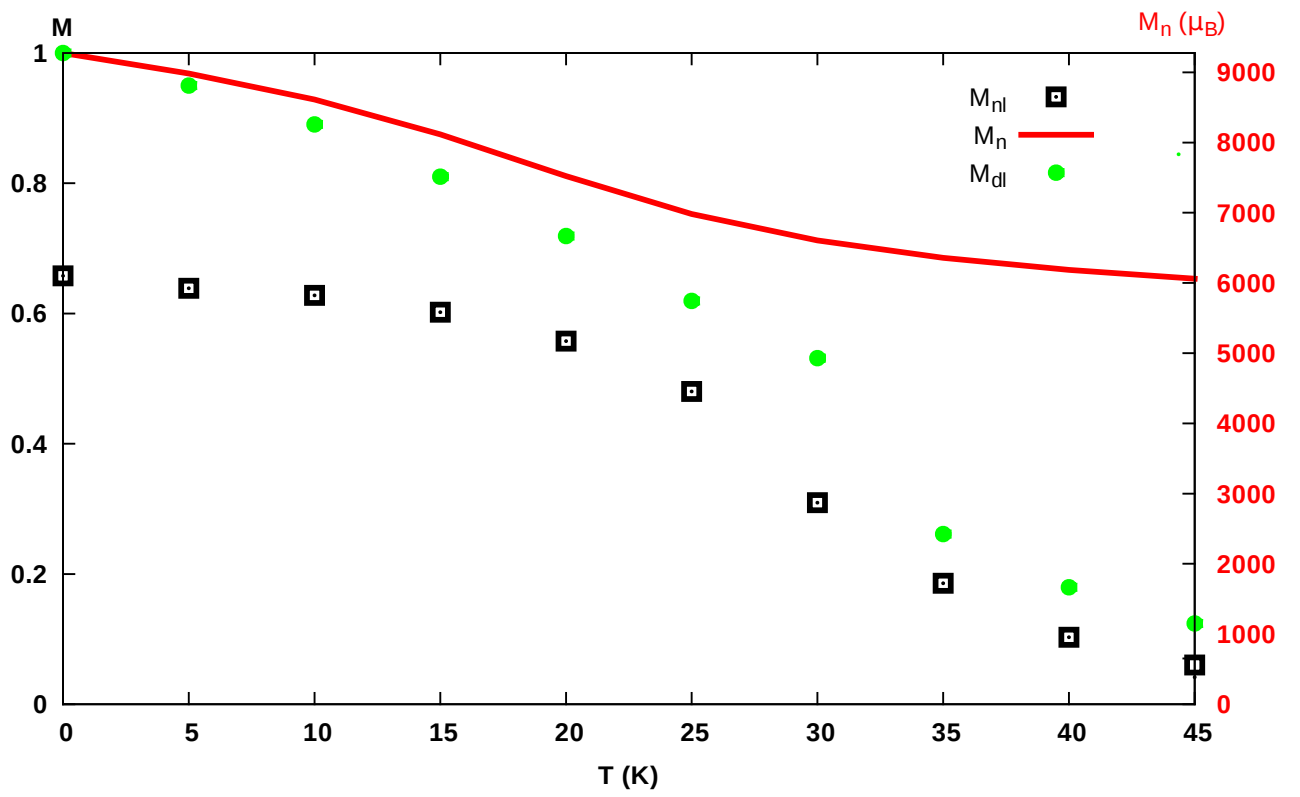


Figure 4.5: As in Fig. 4.4 for the FDc63 lattice.

two systems can be observed even at temperatures as high as 30 K. Since the vacancies are randomly distributed, each nanosphere has a unique vacancies distribution. This results in a unique pinning direction/directions for the magnetic moment of each nanosphere. By placing the nanospheres in a lattice, the pinning directions show a random pattern where the magnetic moment of each nanosphere prefers a different direction. On the other hand, the dipole field prefers orienting the magnetic moment of the nanospheres in the same direction and a competition between the dipole field and the torque due to the pinning effect increases. As shown in Ch. 2, the pinning effect increases with reducing temperature, which explains the reduction in O_{nl} with reducing temperature.

This competition is demonstrated in Fig. 4.6 where the peak in the density of the surface vacancies at the equator in the FDc675 nanosphere array is less pronounced than the corresponding peak for the non-interacting nanospheres (Dc675). Thus, while the pinning effect of the vacancies hinders the ordering of the magnetic moment nanospheres in the FDc675 array as the temperature is reduced, the dipolar field limits the pinning effect of the vacancies and a decrease in the peak in the vacancy distribution around the equator occurs. While this array disorientation effect is masked by the increase in the magnetic moment of the nanospheres when the temperature is reduced as shown in Fig. 4.4, this disorientation is clearly seen in the order parameter O_{nl} shown in Fig. 4.7.

In the case of the FDc63 array the thicker shell means that the magnetic moment of the core and hence M_n is lower than it is in the FDc675 array. This means that the FDc63 array orders at a much lower temperature than the FDc675 array ($T \approx 36.5$ K for the equivalent dipole array as seen in Fig. 4.1). Hence the FDc63 lattice ordering

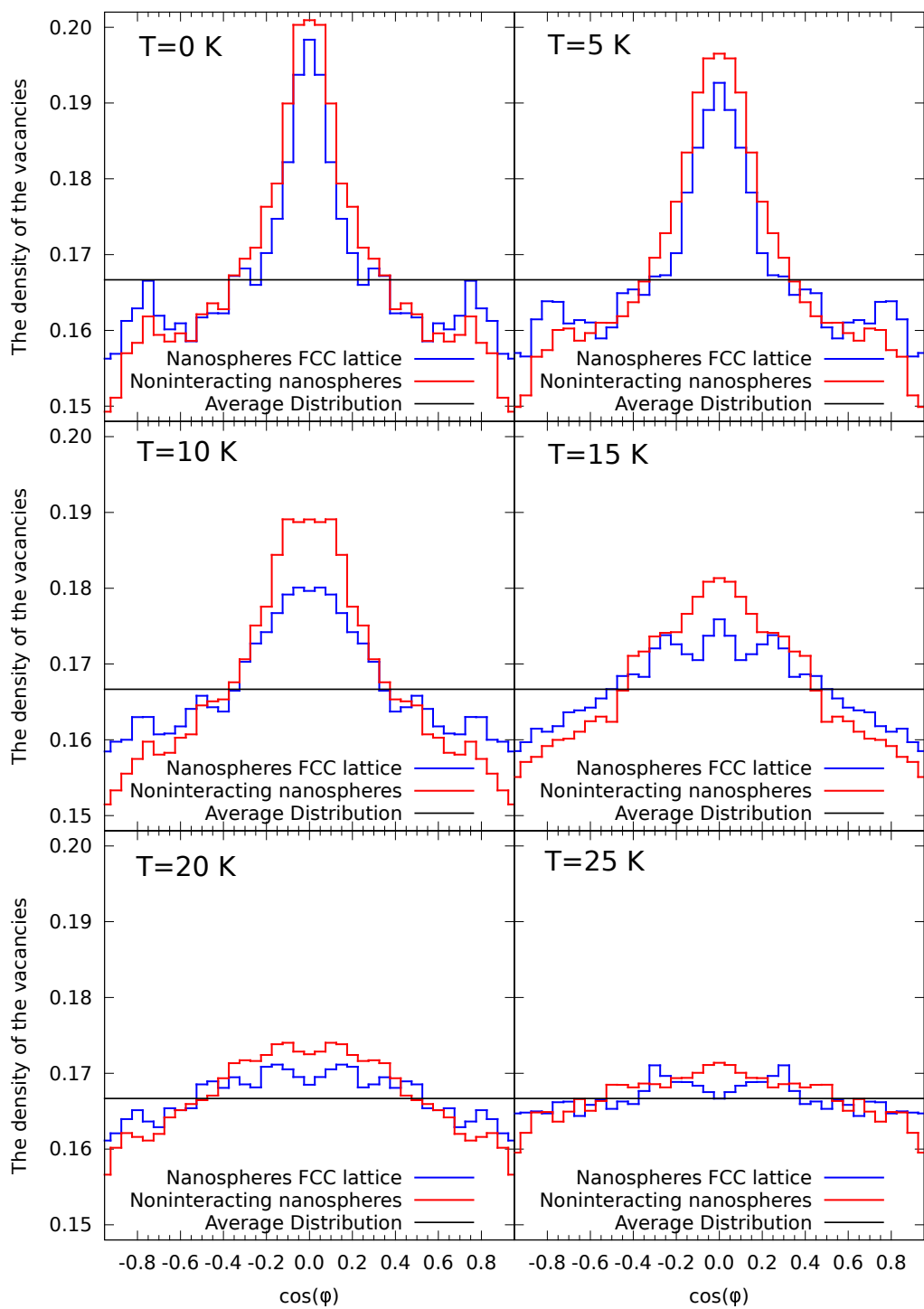


Figure 4.6: The density of the vacancies of the lattice, FDc675, and the corresponding ensemble of non-interacting nanospheres, Dc675, as a function of $\cos(\varphi)$ at different temperatures.

temperature coincides with the estimated pinning temperature ($T \approx 30$ K as shown in Ch. 2 for Dc63). As a result, the pinning effect of the surface vacancies is much more effective in suppressing the formation of ferromagnetic ordering of the FDc63 array than suppressing the ordering of the FD675 array. This is clearly seen in Fig. 4.8 where O_{nl} of the FDc63 lattice and O_{dl} of the equivalent dipole lattice are shown as functions of temperature. By comparing Fig. 4.7 with Fig. 4.8, we note that the difference in the ordering parameter between FDc63 and its equivalent dipole array is much more pronounced than the difference in the ordering parameter between FDc675 and its equivalent dipole array. Fig. 4.9 shows that the order parameter of FDc63 is much lower than the ordering parameter of FDc675 at any temperature. In particular the order parameter at $T = 0$ K, where the only factor that reduces the ordering parameter is the pinning effect. We note that at $T = 0$ K, ($O_{nl} = 0.65$) for the FDc63 array is significantly lower than corresponding value for the FDc675 array ($O_{nl} = 0.80$). Likewise Fig. 4.10, which compares the vacancy profile for the FDc63 nanospheres and the equivalent profile for the non-interacting nanospheres, shows that the effect of the dipole interaction on the polar vacancy distribution is much smaller than the dipole effect on the vacancies distribution for FDc675 array (as shown in Fig. 4.6).

4.4 Summary

Results of MPI simulations of FCC maghemite nanosphere lattices using stochastic LLG implemented by MagLua [44, 45] are presented. The simulation model treats the nanospheres as dipoles to calculate the dipole field at the center of each nanosphere.

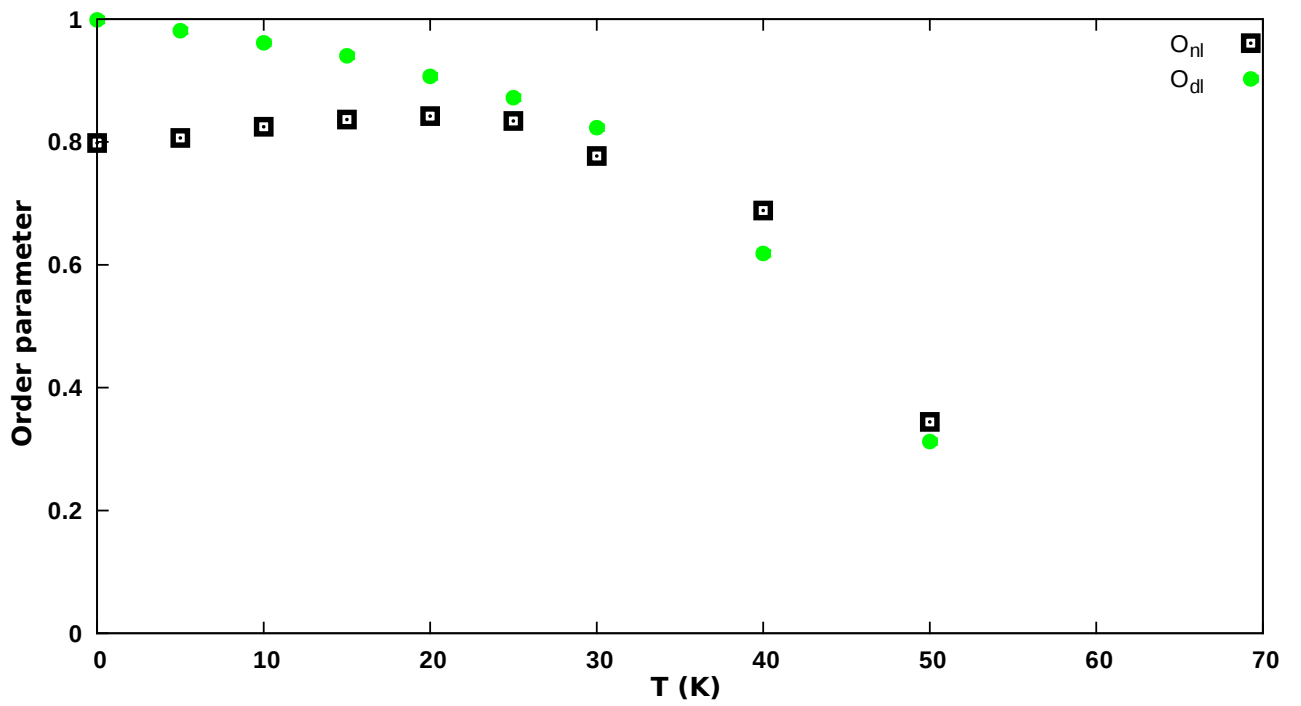


Figure 4.7: O_{nl} and O_{dl} of an $8 \times 8 \times 8$ FCC array as a function of temperature, where the nanospheres have a 7.5 nm diameter, 6.75 nm core diameter and $K_s = 10$ K.

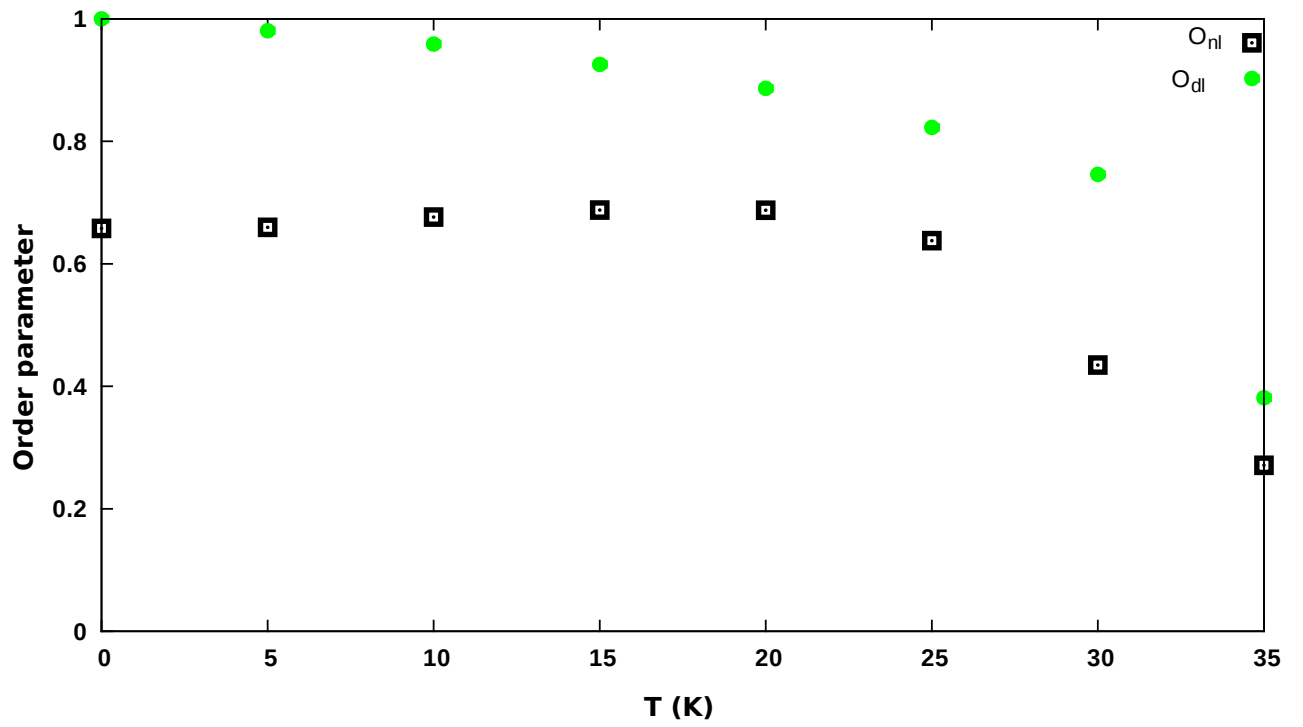


Figure 4.8: O_{nl} and O_{dl} of an $8 \times 8 \times 8$ FCC array as a function of temperature, where the nanospheres have a 7.5 nm diameter and 6.3 nm core diameter.

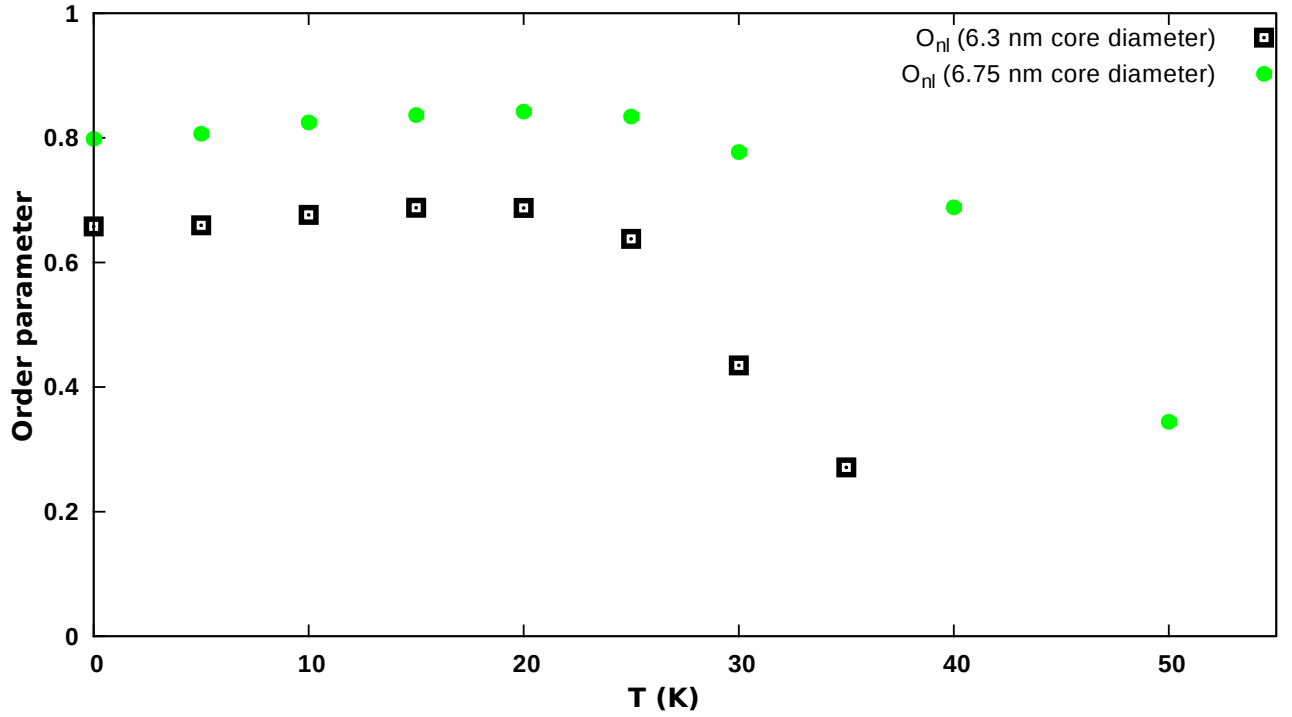


Figure 4.9: O_{nl} of $8 \times 8 \times 8$ FCC arrays as a function of temperature, where the nanospheres have a 7.5 nm diameter with $K_s = 10$ K in both cases. One of the lattices has nanospheres of core diameter 6.3 nm, while the other has nanospheres of core diameter 6.75 nm.

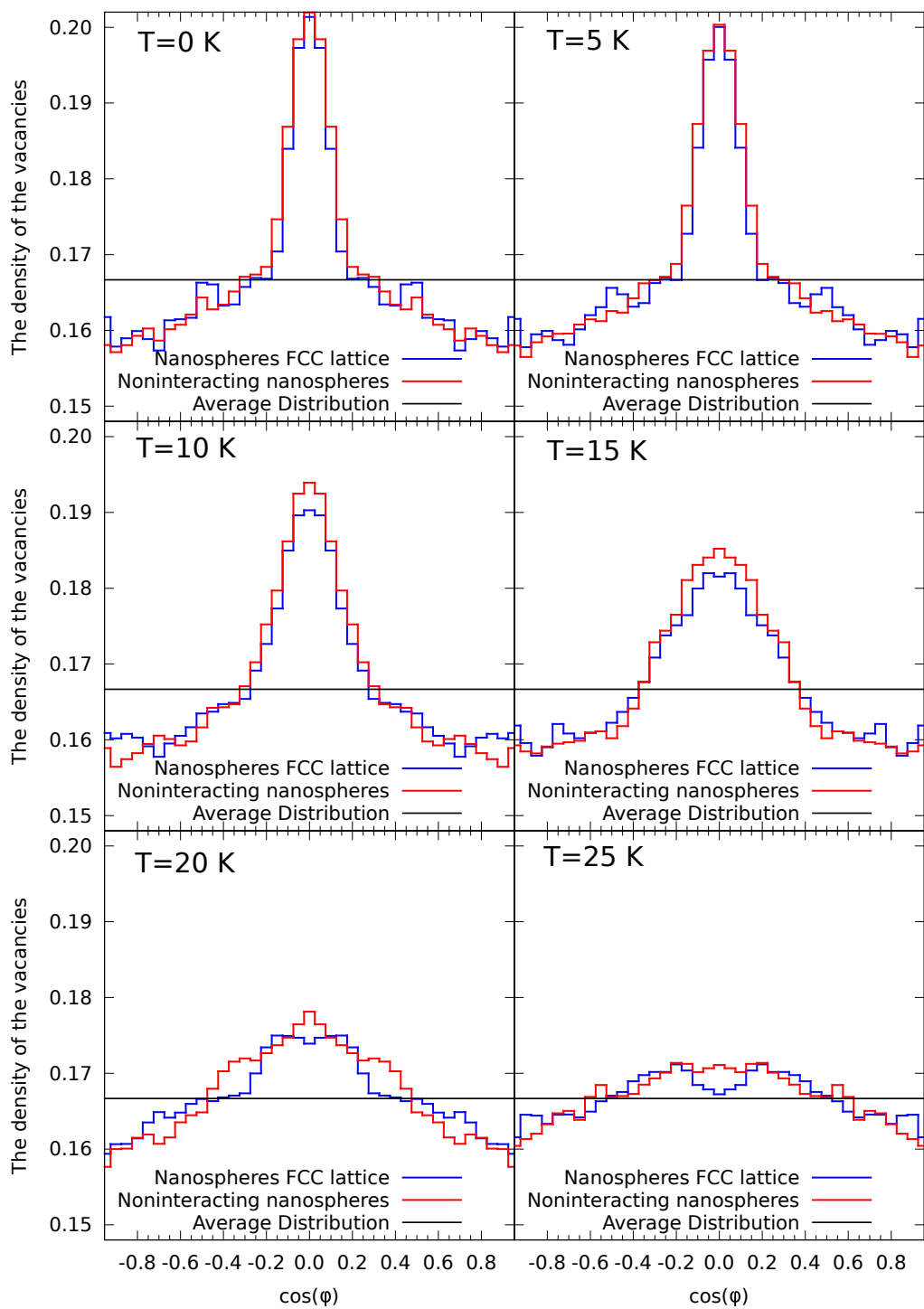


Figure 4.10: The density of the vacancies of the lattice, FDc63, and the corresponding ensemble of non-interacting nanospheres, Dc63, as a function of $\cos(\varphi)$ at different temperatures.

Then the atomistic structure of each nanosphere is taken into account during the stochastic LLG integration. The study of two nanosphere lattices are presented at different surface thicknesses. Each nanosphere lattice is compared with the equivalent dipole lattice which has dipoles with the same magnitude of the magnetic moments of their equivalent nanospheres, while no anisotropy were assigned to the dipoles.

The results show that the ordering temperature of each nanosphere lattice is very close to its equivalent dipole lattice. At temperatures high enough to ignore the pinning effect (above 25 K), the nanospheres behave as superparamagnetic dipoles. Hence, the nanosphere lattice and the equivalent dipole lattice have the same net magnetization at high temperatures. While the magnitude of the magnetic moment of the individual nanospheres increases rapidly below 25 K, the nanosphere lattice net magnetization shows only a very shallow increase. This difference between the net magnetization of the nanosphere lattice and its equivalent dipole lattice might seem at first as a result of the direction of the magnetic moment of the nanospheres being blocked. By defining the orientational order parameter as an average of $\cos(\theta)$, where θ is the angle between the magnetic moment of the nanosphere and the net magnetization of the lattice, we can study the orientational behavior of the nanosphere lattice. The results show that the orientational order parameter of the nanosphere lattices decreases with decreasing the temperature below 25 K. This disorder of the direction of the nanospheres magnetization can be understood in light of the pinning of the domain wall in region with high vacancy density. The results show that the vacancy density is maximum at the magnetic equator for both interacting and noninteracting nanospheres. These peaks get higher and narrower by decreasing temperature, which means the pinning increases with decreasing the temperature. Since the vacancies pin

the magnetic moment of each nanosphere to a unique direction, the strong pinning randomizes the orientational order of the magnetic moment of the nanospheres. This ordering reduction suggests that the pinning of domain walls to the areas with high vacancy density is stronger than the dipole field. Therefore it might be the main factor in determining the maghemite nanospheres blocking temperature.

Increasing the nanospheres surface thickness increases the pinning of the domain wall to the vacancies and decreases the magnitude of the magnetic moment of the nanosphere. As a consequence, lattices of nanospheres of thick surfaces are less ordered than lattices of nanospheres of thin surfaces. This is consistent with what we notice from Figs. 4.6 and 4.10 where the competition between the dipole interactions and the pinning effect reduces the vacancy density at the equator for the lattice FDc675 compared to the noninteracting nanosphere ensemble Dc675 whereas the lattice FDc63 show a vacancy density at the equator almost identical to the corresponding noninteracting nanospheres in the ensemble Dc63.

Chapter 5

Conclusion

Stochastic LLG simulations implemented by MagLua [44, 45] are presented in this thesis. We focus on three systems: maghemite noninteracting nanospheres, FCC dipole lattice, and FCC maghemite nanosphere lattice.

5.1 Maghemite noninteracting nanospheres

Results of stochastic LLG simulations of noninteracting maghemite nanospheres with different surface anisotropies and different surface thicknesses have been presented. The simulation model has a bulk-like core, a radial surface anisotropy, and a weak exchange between the surface spins. The results show two distinct ordering temperatures, T_c and T_s . T_c is close to the bulk maghemite ordering temperature, which is due to the ordering of the core spins, whereas $T_s \simeq 30$ K is due to the ordering of the surface spins. These temperatures are in good agreement with previous MC simulations as shown in the Appendix. A. Comparing Fig. 2.1 with Fig. 1.3 in Ref. [1] shows a qualitative agreement with the experimental results.

The heating and cooling magnetization curves of ZFC ensembles show a blocking temperature that is relatively close to experimental value [1]. Increasing the surface anisotropy results in increasing the blocking temperature, whereas increasing the heating and cooling rates results in a slight increase in the blocking temperature.

Below T_s , the surface spins start to order and the competition between the surface anisotropy and the exchange interactions leads to form a hedgehog-like structure at the surface with a domain wall at the magnetic equator. The surface spins at the magnetic equator have higher energy than the others due to the competition between the exchange and the surface anisotropy. The random vacancy distribution combined with inhomogeneous energy distribution at the surface result in an anisotropic energy by pinning the high energy region which is the magnetic equator at the surface to the low spin density region which is the region of the surface with high vacancy density. This pinning can be understood as a magnetic torque that change the location of the magnetic equator by changing the direction of the magnetic moment to maximize the number of vacancies at the magnetic equator.

The results show that increasing the surface anisotropy increases the peak in the surface vacancy density at the equator and reduces the width of this peak, which indicates an increase in the pinning effect. Similar changes were observed when the surface thickness was increased from 0.36 nm to 0.6 nm.

5.2 FCC dipole lattice

In Ch. 3, we present simulations of different sizes of FCC dipole lattices with periodic boundary conditions where the dipole fields are the only interaction between

the dipoles. The Binder parameter shows a reduced ordering temperature $Td = 0.625 \pm 0.01$ that agrees with previous MC simulations [51]. The specific heat and the susceptibility as functions of temperature show peaks that are consistent with a typical second order phase transition. Energy calculations show a degenerate ferromagnetic ground state with a reduced energy of -2.956 in any direction of the magnetization. The calculated ground state energy shows agreement with a previous computations [50]. The simulations show that at any finite temperature, the net magnetization prefers the $[1\ 1\ 1]$ direction or any of its equivalents with no second transition that changes the preferred direction, contrary to what Bouchaud had suggested [51].

5.3 Maghemite nanospheres on FCC lattice with dipole interactions

In Ch. 4, we present multi-scale simulations of FCC maghemite nanosphere arrays with periodic boundary conditions where the inter-particle dipole interaction and the intra-particle exchange interactions and anisotropy are included. The dipole field is calculated at the center of each nanosphere by assuming that each nanosphere is a point dipole and the dipole field is applied to each nanosphere and then, the stochastic LLG integrations are performed on atomistic level. To the best of our knowledge, this is the only simulation example of this type of multi-scale modelling. This procedure was implemented by MagLua [44, 45] using MPI where each nanosphere was assigned to a single processing core. The array net magnetization and the inter-particle orien-

tational order parameter were compared with the equivalent dipole lattice which has dipoles with the same magnitude of the magnetic moments of the nanospheres, while no anisotropy were assigned to the dipoles.

At high temperature ($T > 25$ K), we can ignore the pinning effect and the nanospheres behave as superparamagnetic dipoles. Hence, the magnetization and the ordering temperature of the nanosphere arrays are very close to the results obtained for equivalent dipole arrays as shown in Fig. 4.4.

While the magnitude of the magnetic moment of the individual nanospheres increases rapidly below 25 K, the nanosphere lattice net magnetization shows only a very shallow increase. This odd behavior indicates an inter-particles orientational disordering with decreasing temperature. Results of the orientational order parameter as a function of temperature confirms this inter-particles disordering below $T = 25$ K as shown in Figs. 4.7 and 4.8.

As shown in Figs. 4.6 and 4.10, the pinning of the magnetic equator to the areas with high surface vacancy is strong at $T < 25$ K and increases with decreasing the temperature even in the presence of the dipole interactions. The fact that the pinning preferred direction is unique for each nanosphere explains the reduction in the ordering parameter.

Since increasing the nanospheres surface thickness increases the pinning of the domain wall to the vacancies and decreases the magnitude of the magnetic moment of the nanosphere as shown in Ch. 2, lattices of nanospheres with thick surfaces are less ordered than lattices of nanospheres of thin surfaces as shown in Fig. 4.9.

The simulations of the nanosphere FCC lattice show an ordering temperature, $T \simeq 50$ K, that is much lower than the temperature obtained experimentally ($T =$

400 K) from MH-loops [20] for nanospheres with the same size. In fact, the simulation assumes that the nanospheres are just touching each other while the experimental results in Ref. [20] are for nanospheres that are separated from each other due to the ferritin coat and therefore should show lower ordering temperature than the simulations. A possible explanation of this discrepancy may be the presence of a very strong core anisotropy where the Ising model is a valid approximation [62]. In addition, there are many factors that may cause the difference between the experimental results and the simulations such as the finite lattice size in the experiment and the unclear effect of the ferritin cage on the surface.

The inter-particles orientational disorder due to the surface vacancies can be generalized to other one [14], two [15, 58], and three [8, 20] dimensional maghemite structures. Also, we can expect this pinning due to the surface vacancies to be present in other nanospheres of cation-deficient magnetic materials such as Fe_2TiO_4 and FeCr_2O_4 [63]. This disordering mechanism provides a reasonable explanation for the reduction in the FCC lattice magnetization at low temperatures as the experiments in Ref. [62] show.

5.4 Future work

The work presented in this thesis can be extended to determine and quantify the energy landscape of nanospheres as a function of the orientation of the nanosphere magnetic axis. This combined with the study of the dynamical response of nanospheres to applied field and temperature can be exploited in determining the relation between domain wall pinning due to vacancy distribution and the blocking temperature. Also,

we intend to study further the origin of discrepancy between the ordering temperature of the nanosphere lattice from simulations and from MH loops.

Bibliography

- [1] T. N. Shendruk, R. D. Desautels, B. W. Southern, and J. van Lierop, “The effect of surface spin disorder on the magnetism of $\gamma - \text{Fe}_2\text{O}_3$ nanoparticle dispersions,” *Nanotechnology*, vol. 18, p. 455704, 2007.
- [2] S. P. Gubin, Y. A. Koksharov, G. B. Khomutov, and G. Y. Yurkov, “Magnetic nanoparticles: preparation, structure and properties,” *Russian Chemical Reviews*, vol. 74, p. 489, 2005.
- [3] E. Mazarío, P. Herrasti, M. P. Morales, and N. Menéndez, “Synthesis and characterization of CoFe_2O_4 ferrite nanoparticles obtained by an electrochemical method,” *Nanotechnology*, vol. 23, p. 355708, 2012.
- [4] B. Issa, I. M. Obaidat, B. A. Albiss, and Y. Haik, “Magnetic nanoparticles: Surface effects and properties related to biomedicine applications,” *International Journal of Molecular Sciences*, vol. 14, pp. 21266–21305, 2013.
- [5] K. Okuyama and I. W. Lenggoro, “Preparation of nanoparticles via spray route,” *Chemical Engineering Science*, vol. 58, pp. 537 – 547, 2003.

- [6] P. Tartaj, M. d. P. Morales, S. Veintemillas-Verdaguer, T. González-Carreño, and C. J. Serna, “The preparation of magnetic nanoparticles for applications in biomedicine,” *Journal of Physics D: Applied Physics*, vol. 36, p. R182, 2003.
- [7] F. Brem, G. Stamm, and A. M. Hirt, “Modeling the magnetic behavior of horse spleen ferritin with a two-phase core structure,” *Journal of Applied Physics*, vol. 99, p. 123906, 2006.
- [8] O. Kasyutich, A. Sarua, and W. Schwarzacher, “Bioengineered magnetic crystals,” *Journal of Physics D: Applied Physics*, vol. 41, p. 134022, 2008.
- [9] C. Ross, “Patterned magnetic recording media,” *Annual Review of Materials Research*, vol. 31, pp. 203–235, 2001.
- [10] V. Rovenzano, R. D. Shull, A. J. Shapiro, and V. Provenzano, “Reduction of hysteresis losses in the magnetic refrigerant $\text{Gd}_5\text{Ge}_2\text{Si}_2$ by the addition of iron,” *Nature*, vol. 429, p. 853, 2004.
- [11] H. Zeng, C. T. Black, R. L. Sandstrom, P. M. Rice, C. B. Murray, and S. Sun, “Magnetotransport of magnetite nanoparticle arrays,” *Phys. Rev. B*, vol. 73, p. 020402, 2006.
- [12] M. De, P. S. Ghosh, and V. M. Rotello, “Applications of nanoparticles in biology,” *Advanced Materials*, vol. 20, pp. 4225–4241, 2008.
- [13] W. Shen, B. D. Schrag, M. J. Carter, and G. Xiao, “Quantitative detection of DNA labeled with magnetic nanoparticles using arrays of MgO-based magnetic tunnel junction sensors,” *Applied Physics Letters*, vol. 93, 2008.

- [14] B. Mehdaoui, R. P. Tan, A. Meffre, J. Carrey, S. Lachaize, B. Chaudret, and M. Respaud, "Increase of magnetic hyperthermia efficiency due to dipolar interactions in low-anisotropy magnetic nanoparticles: Theoretical and experimental results," *Phys. Rev. B*, vol. 87, p. 174419, 2013.
- [15] S. Fleutot, G. L. Nealon, M. Pauly, B. P. Pichon, C. Leuvrey, M. Drillon, J.-L. Gallani, D. Guillon, B. Donnio, and S. Begin-Colin, "Spacing-dependent dipolar interactions in dendronized magnetic iron oxide nanoparticle 2D arrays and powders," *Nanoscale*, vol. 5, pp. 1507–1516, 2013.
- [16] Z. P. A. K. E. Nie, "Properties and emerging applications of self-assembled structures made from inorganic nanoparticles," *Nat Nano*, vol. 5, p. 1038, 2010.
- [17] S. Sun, "Recent Advances in Chemical Synthesis, Self-Assembly, and Applications of FePt Nanoparticles," *Advanced Materials*, vol. 18, pp. 393–403, 2006.
- [18] M. Chen, D. E. Nikles, H. Yin, S. Wang, J. Harrell, and S. A. Majetich, "Patterning self-assembled FePt nanoparticles," *Journal of Magnetism and Magnetic Materials*, vol. 266, pp. 8 – 11, 2003.
- [19] H. F. Hamann, S. I. Woods, and S. Sun, "Direct Thermal Patterning of Self-Assembled Nanoparticles," *Nano Letters*, vol. 3, pp. 1643–1645, 2003.
- [20] M. A. Kostianen, P. Ceci, M. Fornara, P. Hiekkataipale, O. Kasyutich, R. J. M. Nolte, J. J. L. M. Cornelissen, R. D. Desautels, and J. van Lierop, "Hierarchical Self-Assembly and Optical Disassembly for Controlled Switching of Magnetoferritin Nanoparticle Magnetism," *ACS Nano*, vol. 5, pp. 6394–6402, 2011.

- [21] X. Xu, A. K. Azad, and J. T. Irvine, “Photocatalytic H₂ generation from spinels ZnFe₂O₄, ZnFeGaO₄, and ZnGa₂O₄,” *Catalysis Today*, vol. 199, pp. 22 – 26, 2013.
- [22] R. Feng, H. Al-Megren, M. Al-Kinany, M. Rood, and Z. Yan, “SO₂ abatement over nanocrystalline MgAl₂O₄ spinel-supported catalysts,” *Journal of Porous Materials*, vol. 20, pp. 571–577, 2013.
- [23] D. Gilks, L. Lari, Z. Cai, O. Cespedes, A. Gerber, S. Thompson, K. Ziemer, and V. K. Lazarov, “Magnetism and magnetotransport in symmetry matched spinels: Fe₃O₄/MgAl₂O₄,” *Journal of Applied Physics*, vol. 113, 2013.
- [24] J.-R. Huang and C. Cheng, “Cation and magnetic orders in MnFe₂O₄ from density functional calculations,” *Journal of Applied Physics*, vol. 113, 2013.
- [25] K. E. Sickafus, J. M. Wills, and N. W. Grimes, “Structure of spinel,” *Journal of the American Ceramic Society*, pp. 3279–3292, 1999.
- [26] X.-M. Liu, S.-Y. Fu, and H.-M. Xiao, “Fabrication of octahedral magnetite microcrystals,” *Materials Letters*, vol. 60, pp. 2979 – 2983, 2006.
- [27] A. U. Gehring, H. Fischer, M. Louvel, K. Kunze, and P. G. Weidler, “High temperature stability of natural maghemite: a magnetic and spectroscopic study,” *Geophysical Journal International*, vol. 179, no. 3, pp. 1361–1371, 2009.
- [28] I. S. Ricardo Grau-Crespo, Asmaa Y Al-Baitai and N. H. D. Leeuw, “Vacancy ordering and electronic structure of -fe₂o₃ (maghemite): a theoretical investigation,” *J. Phys.: Condens. Matter*, vol. 22, 2010.

- [29] K. Rudzka, J. L. Viota, J. Muoz-Gamez, A. Carazo, A. Ruiz-Extremera, and V. Delgado, “Nanoengineering of doxorubicin delivery systems with functionalized maghemite nanoparticles,” *Colloids and Surfaces B: Biointerfaces*, vol. 111, pp. 88 – 96, 2013.
- [30] D. Serrano-Ruiz, M. Laurenti, J. Ruiz-Cabello, E. Lopez-Cabarcos, and J. Rubio-Retama, “Hybrid microparticles for drug delivery and magnetic resonance imaging,” *Journal of Biomedical Materials Research Part B: Applied Biomaterials*, vol. 101B, pp. 498–505, 2013.
- [31] B. Sun, W. Zhao, Y. Xiong, Y. Lin, and P. Chen, “Effect of thickness and annealing temperature on magnetic properties of ultrathin γ - Fe_2O_3 films grown on silicon substrate,” *Metallurgical and Materials Transactions A*, vol. 45, no. 11, pp. 5245–5248, 2014.
- [32] Z. S. Wu, W. Xiao, X. X., “Synthesis and magnetic properties of maghemite (γ – Fe_2O_3) short-nanotubes,” *Nanoscale Research Letters.*, vol. 5, pp. 1474–1479, 2010.
- [33] D. Lin, A. Nunes, C. Majkrzak, and A. Berkowitz, “Polarized neutron study of the magnetization density distribution within a CoFe_2O_4 colloidal particle II,” *Journal of Magnetism and Magnetic Materials*, vol. 145, pp. 343–348, 1995.
- [34] R. H. Kodama, A. E. Berkowitz, J. E. J. McNiff, and S. Foner, “Surface Spin Disorder in NiFe_2O_4 Nanoparticles,” *Phys. Rev. Lett.*, vol. 77, pp. 394–397, 1996.
- [35] R. H. Kodama and A. E. Berkowitz, “Atomic-scale magnetic modeling of oxide nanoparticles,” *Phys. Rev. B*, vol. 59, pp. 6321–6336, 1999.

- [36] J. Restrepo, Y. Labaye, and J. Greneche, “Surface anisotropy in maghemite nanoparticles,” *Physica B: Condensed Matter*, vol. 384, pp. 221 – 223, 2006.
- [37] K. Adebayo, “Magnetic nanoparticles,” *MSc. thesis, Manitoba University: Canada*, 2009.
- [38] J. Mazo-Zuluaga, J. Restrepo, and J. Meja-Lpez, “Effect of surface anisotropy on the magnetic properties of magnetite nanoparticles: A heisenberg-monte carlo study,” *Journal of Applied Physics*, vol. 103, 2008.
- [39] J. Mazo-Zuluaga, J. Restrepo, F. Muoz, and J. Meja-Lpez, “Surface anisotropy, hysteretic, and magnetic properties of magnetite nanoparticles: A simulation study,” *Journal of Applied Physics*, vol. 105, 2009.
- [40] H. Kachkachi and E. Bonet, “Surface-induced cubic anisotropy in nanomagnets,” *Phys. Rev. B*, vol. 73, p. 224402, 2006.
- [41] D. Brinis, A. Laggoun, D. Ledue, and R. Patte, “Effects of dimensionality and spatial distribution on the magnetic relaxation of interacting ferromagnetic nanoclusters: A monte carlo study,” *Journal of Applied Physics*, vol. 115, 2014.
- [42] C. L. Dennis and R. Ivkov, “Physics of heat generation using magnetic nanoparticles for hyperthermia,” *International Journal of Hyperthermia*, vol. 29, pp. 715–729, 2013.
- [43] M. Woińska, J. Szczytko, A. Majhofer, J. Gosk, K. Dziatkowski, and A. Twardowski, “Magnetic interactions in an ensemble of cubic nanoparticles: A monte carlo study,” *Phys. Rev. B*, vol. 88, p. 144421, 2013.

- [44] J. I. Mercer and J. P. Whitehead, “Maglua: A general purpose, parallel, scriptable micromagnetics simulator with graphics processing unit acceleration,” *J. Comp. Phys.* (in preparation).
- [45] J. I. Mercer and J. P. Whitehead, “Scripted micromagnetics environment,” *presentation at Magnetic North II*, St.Johns,NL, 2011.
- [46] K. De’Bell, A. B. MacIsaac, and J. P. Whitehead, “Dipolar effects in magnetic thin films and quasi-two-dimensional systems,” *Rev. Mod. Phys.*, vol. 72, pp. 225–257, 2000.
- [47] M. d’Aquino, *Nonlinear Magnetization Dynamics in Thin-films and Nanoparticles*. PhD thesis, 2004.
- [48] J. P. Vejpravov, J. Plocek, A. Hutlov, and J. L. Rehspringer, “Superparamagnetism Of Co-ferrite Nanoparticles,” *Week of Doctoral Students, Proceedings of Contributed Papers, Part III*, pp. 518–523, 2005.
- [49] Private communications with J. V.Lierop.
- [50] J. W. M. Fitzpatrick, “Finite temperature spin waves in magnetic thin films,” *B.Sc. (Hons) Thesis, Memorial University of Newfoundland: Canada*, 2012.
- [51] J. P. Bouchaud and P. G. Zérah, “Dipolar ferromagnetism: A monte carlo study,” *Phys. Rev. B*, vol. 47, pp. 9095–9097, 1993.
- [52] Y. Tomita, “Monte carlo study of two-dimensional heisenberg dipolar lattices,” *Journal of the Physical Society of Japan*, vol. 78, p. 114004, 2009.

- [53] L. W. McKeehan, “Magnetic dipole fields in unstrained cubic crystals,” *Phys. Rev.*, vol. 43, pp. 913–923, 1933.
- [54] Private communications with B. W. Southern and M. Gingras., 2014.
- [55] K. Binder and A. P. Young, “Spin glasses: Experimental facts, theoretical concepts, and open questions,” *Rev. Mod. Phys.*, vol. 58, pp. 801–976, 1986.
- [56] D. Eberbeck and L. Trahms, “Experimental investigation of dipolar interaction in suspensions of magnetic nanoparticles,” *Journal of Magnetism and Magnetic Materials*, vol. 323, pp. 1228 – 1232, 2011.
- [57] D. Farrell, Y. Cheng, R. W. McCallum, M. Sachan, and S. A. Majetich, “Magnetic Interactions of Iron Nanoparticles in Arrays and Dilute Dispersions,” *The Journal of Physical Chemistry B*, vol. 109, pp. 13409–13419, 2005.
- [58] L. G. Paterno, E. H. C. P. Sinnecker, M. A. G. Soler, J. P. Sinnecker, M. A. Novak, and P. C. Morais, “Tuning of Magnetic Dipolar Interactions of Maghemite Nanoparticles Embedded in Polyelectrolyte Layer-by-Layer Films,” *Journal of Nanoscience and Nanotechnology*, vol. 12, pp. 6672–6678, 2012.
- [59] D. Kechrakos and K. N. Trohidou, “Dipolar interaction effects in the magnetic and magnetotransport properties of ordered nanoparticle arrays,” *Journal of Nanoscience and Nanotechnology*, vol. 8, pp. 2929–2943, 2008.
- [60] M. L. Plumer, J. van Lierop, B. W. Southern, and J. P. Whitehead, “Micromagnetic simulations of interacting dipoles on an fcc lattice: application to nanopar-

- ticle assemblies,” *Journal of Physics: Condensed Matter*, vol. 22, p. 296007, 2010.
- [61] D. Kechrakos, K. Trohidou, and M. Vasilakaki, “Magnetic properties of dense nanoparticle arrays with core/shell morphology,” *Journal of Magnetism and Magnetic Materials*, vol. 316, pp. e291 – e294, 2007.
- [62] O. Kasyutich, R. D. Desautels, B. W. Southern, and J. van Lierop, “Novel aspects of magnetic interactions in a macroscopic 3D nanoparticle-based crystal,” *Phys. Rev. Lett.*, vol. 104, p. 127205, 2010.
- [63] E. Schmidbauer, “Mssbauer spectroscopy and magnetization of cation-deficient Fe_2TiO_4 and FeCr_2O_4 ,” *Physics and Chemistry of Minerals*, vol. 14, pp. 533–541, 1987.

Appendix A

Comparing Stochastic LLG with Monte Carlo

Adebayo *et al.* [37] MC simulations (AMC) use double the core exchange parameters that are used in Kodama simulations (KLLG) [34]. However, the energy expression in AMC counts the exchange between two ions only once (Eq. 1.5), while the energy expression in KLLG counts it twice [34](similar to Eq 2.5). Therefore, the core ordering temperature must be the same in the two studies. However, each iron ion in KLLG was assigned $5 \mu_b$, while each iron ion in AMC was assigned $1 \mu_b$. As a result, the magnetization unit in Figs. 1.5, 1.6, and 1.7 is $(5\mu_b/\text{ion})$. Also, this difference results in a scaling factor of $5 * 5 = 25$ in energy, anisotropy, and temperature as we conclude from the energy expression in Eq. 1.5. Hence the core ordering temperature in KLLG ($T \simeq 900$ K) should translate into $T \simeq 900/25 = 36$ in AMC units. However, the core ordering temperature in AMC is about twice the expected value as shown in Fig. 1.6. This might mean that the exchange is counted twice in AMC. To

confirm this, the total magnetization as a function of temperature is shown in Fig. A.1 where the data compares AMC results with our stochastic LLG results using the same parameters while the exchange is counted twice. The two curves are matching and hence a scaling factor of $25/2 = 12.5$ is required for the temperature in AMC results and the factor of 25 that is applied to the exchange parameters to get the results in Ch. 2 and Ch. 4 is valid. Also, as shown in Fig. 2.1, the stochastic LLG simulations give a core ordering temperature $T_c \simeq 900$ K, in agreement with the results in KLLG Ref [34].

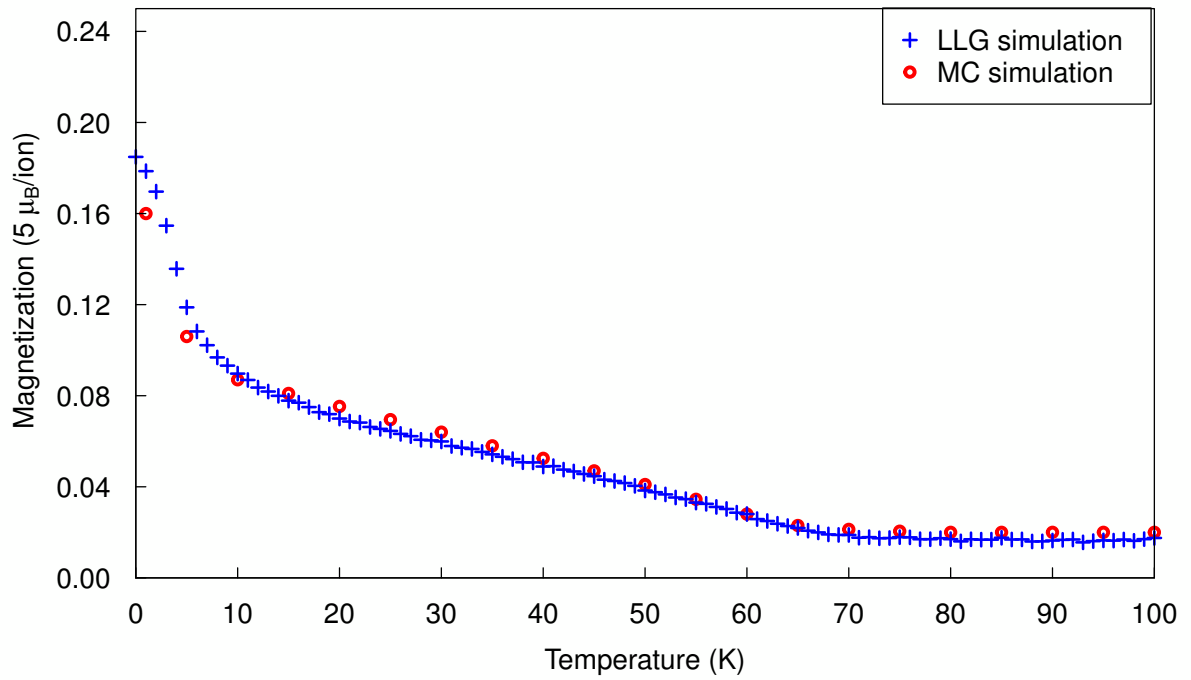


Figure A.1: The total magnetization of maghemite single nanosphere with 5 nm diameter as a function of temperature. The data compares MC simulations from Ref. [37] with stochastic LLG simulation results. The units of temperature, field, and anisotropy are (12.5 K) and the magnetization unit is $5 \mu_B/\text{ion}$.

Appendix B

Comparing noninteracting maghemite nanosphere simulation with experimental results

The saturation magnetization of dispersed 7 nm diameter maghemite nanospheres as a function of temperature is shown in Fig. B.1. The data represents the experimental results (from Ref. [1]) and stochastic LLG simulations. The nanospheres in the simulations have 0.735 nm surface thickness and $K_s = 20$ K. The core exchange parameters have the same values as in Table 2.1, while and surface-surface and surface-core exchange interactions are divided by 50. The applied field is 5 K (1.49 T).

As shown in Fig. B.1, the surface ordering temperature and the shape of the surface saturation magnetization obtained from the simulations is in agreement with the experiment. Also the core ordering temperature is close to the bulk maghemite ordering

temperature and in agreement with previous MC simulations [34].

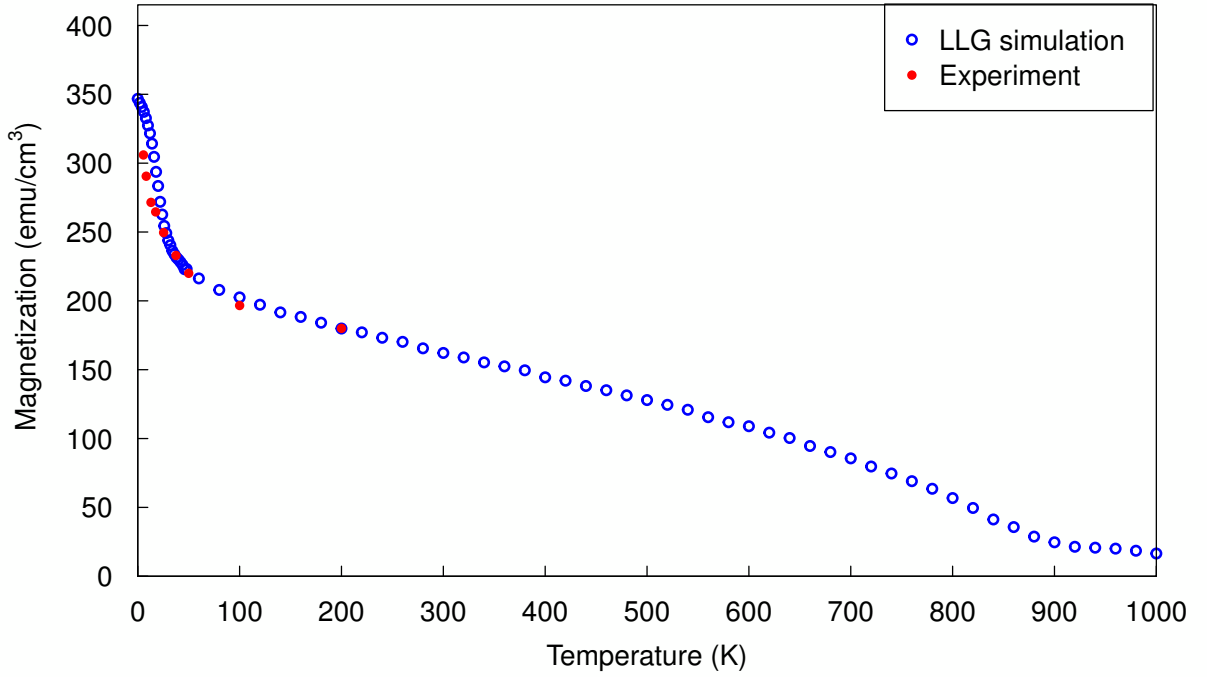


Figure B.1: The saturation magnetization of 7 nm diameter dispersed maghemite nanospheres as a function of temperature. The data represents the experimental results in Ref. [1] (red) and the stochastic LLG simulations with $K_s = 20$ K and 0.735 nm surface thickness.

Appendix C

Euler integration error in nanospheres lattice

Above the blocking temperature $T = 20$ K, the nanospheres are expected to behave as superparamagnetic dipoles and the nanosphere lattice magnetization (M_{nl}) must be identical to the magnetization of the corresponding dipole lattice (M_{dl}). However, M_{nl} at high temperature is a little higher than M_{dl} as shown in Ch. 4.

The lattice magnetization (M_{nl}) of the FDc675 array and the corresponding dipole lattice (Dc63) as functions of temperature are shown in Fig. C.1. The data compares M_{nl} results obtained by Euler integration with results obtained by RK4 using a time step of $2 \times 10^{-4}t_u$. Since RK4 and Euler results are the same for M_{dl} only one curve is shown to represent M_{dl} . M_{nl} clearly converges to the dipoles array value (M_{dl}) at high temperature by reducing the error using a higher order integration method (RK4). Updating the dipole field every time step and running the simulation for longer time did not change the difference between M_{nl} and M_{dl} at high temperature

for both methods. In fact, Euler integration gives reliable results for noninteracting nanospheres or a lattice of dipoles and no difference from RK4 integration was observed. This means that when Euler integration produces a systematic error when the dipole field is introduced to the nanospheres.

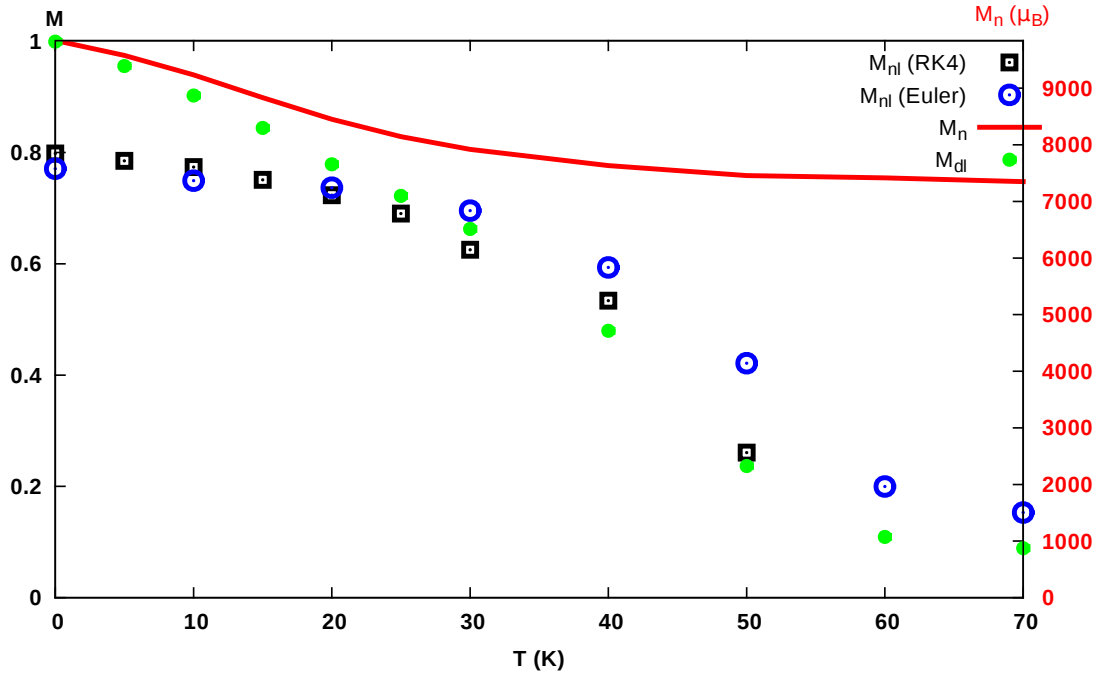


Figure C.1: The magnetization of the FDC675 FCC nanosphere lattice and the corresponding dipole lattice. The data represents results using Euler and RK4 integration of the LLG equation with time step $2 \times 10^{-4} t_u$.